Humanoid Robot Dynamic Synchronization via Whole-Body Teleoperation with Bilateral Feedback

by

João Luiz Almeida de Souza Ramos

Submitted to the Department of Mechanical Engineering
in partial fulfillment of the requirements for the degree of

Doctor of Philosophy

at the

MASSACHUSETTS INSTITUTE OF TECHNOLOGY

September 2018

Signature redacted

Author ....
Department of Mechanical Engineering
August 16, 2018

Signature redacted

Certified by ....
Sangbae Kim
Associate Professor of Mechanical Engineering
Thesis Supervisor

Signature redacted

Accepted by...
Rohan Abeyaratne
Chairman, Department Committee on Graduate Theses

Humanoid Robot Dynamic Synchronization via Whole-Body Teleoperation with Bilateral Feedback

by

João Luiz Almeida de Souza Ramos

Submitted to the Department of Mechanical Engineering
on August 16, 2018, in partial fulfillment of the
requirements for the degree of
Doctor of Philosophy

Abstract

Despite remarkable recent advances in robotic research, legged machines are still far from robustly executing physical actions with comparable performance to humans. Yet, the potential applications for robots with such unique capabilities range from disaster response all the way to elderly care and further. Hence, an intuitive short-term answer for this issue lies on harnessing human motor control abilities and transferring them to the remote robot via whole-body teleoperation while providing the operator with real-time physical feedback from his/her actions. Motivated by such a promising solution, this Thesis presents an introductory study to achieve human and bipedal robot dynamic synchronization via whole-body teleoperation and bilateral feedback. This work describes how we can utilize powerful simple models to explore the interplay between human Center of Mass motion and the contact forces with the environment in order to transmit to the robot the underlying balancing and stepping strategy. All the necessary fundamental equations for the coupled dynamics in the Frontal Plane are presented along with the human feedback law and motion data mapping derived from the imposition of dynamic similarity. We take a closer look on how the natural frequency of each system influences the resulting motion and analyze how the coupled system responds to various robot scales. We present experiments in which a human operator controls a bipedal robot to show how the feedback from the Human-Machine Interface varies according to the robot's characteristic time response and the perturbations from its surrounding environment. Finally, we describe the implementation of the presented strategy on a small-scale dynamic robot, Little HERMES, to allow it to balance, jump and take steps in place simultaneously with the human operator. We expect that the results presented in this Thesis will eventually allow robots to achieve motor dexterity and coordination that can rival their biological counterparts.

Thesis Supervisor: Sangbae Kim
Title: Associate Professor of Mechanical Engineering

Acknowledgments

Primarily, I would like to express my deepest gratitude to my advisor, Prof. Sangbae Kim, for investing in me from the beginning and giving me the opportunity to work at the Biomimetic Robotics Lab. I consider myself very fortunate to have him as a mentor and as a friend during my time at MIT. Thank you for pushing my ambitions beyond my comfort zone and opening my eyes for a whole different way of thinking about robots, research and life. I'll definitely miss the time I spent in the lab.

I also would like to thank all my committee members, Prof. Neville Hogan, Prof. David Trumper and Prof. Leia Stirling for the extremely insightful meetings and always showing genuine interest in my work. I invited you to be part of my committee because you represent role models to me; you have my deepest respect and admiration. Thank you all for the priceless time you invested in my academic career.

I'm incredibly happy to have had the chance to work in the lab with some of the brightest and most fun people I ever met. Regardless of the problems I encountered, I always knew that someone in the lab would have the answer. Specifically, John Mayo, Wyatt Ubellacker, Will Bosworth, Hae-Won Park, Gerardo Bledt, Matthew Powell, Chiheb Boussema, Yichao Pan, Erich Meinig, Tony Stuart, Justin Cheung, Sam Ingersoll , and many others that I didn't mention for lack of memory or space. Thank you all for making my work easier and my life happier. I would like to specially thank Michael Chuah and Ben Katz for the direct collaboration with my experiments and for always be willing to help me. My research could not have been completed without you.

I extend a particular gratitude to two people that now I consider friends for life. Albert Wang, for literally staying by my side during my entire graduate life at MIT, and for the countless discussions about motors, robots, research, work, problems, life, death and everything else in between. Thank you for being such a good friend and always so supportive. And Patrick Wensing, for all the advices and for being like a second advisor to me. Your good spirit and character have always inspired me in many occasions in my graduate life. Thank you both for helping me shape most of my personal concepts about work and academia.

During all the time I spent at MIT, I couldn't have asked for better friends from many groups in MechE from my very first day. Thank you to Robert Katzschmann, Claudio Hail, Mustafa Mohamad, Tommaso Tadei, Andrew Huock, Connor Mulcahy, Shawn Zhang, Affi Maragh, Sara Nagelberg, Uyanga Tsedev, Chris Merian, Phillip Daniel, and so many others. Thank you also to all the MechE staff and Professors, specially Leslie Regan, Una Sheehan, Alexandra Cabral, Prof. Rohan Abeyaratne, Prof. Maria Yang, Prof. Gang Chen, and everyone else. You all make me proud of being part of the MIT family.

If I ever accomplished anything during my career, it was mostly thanks to the support of my amazing friends from Brazil and other countries. Particular people I would like to address are Fabio Paredes, Cesar Lampe, Thiago Marinho, Junior, Mateus Braunes, Guilherme Rodrigues, Igor Girsas, Alexandre Ormiga, Gabriel Barsi, Germano Cereja, Marcell Hosana, Ricardo Marques, Luiz Santarelli, and many others. Thank you Prof. Marco Meggiolaro and Felipe Depine for all the support and advices.

Most importantly, I want to thank my family for everything they have done for me, for believing on my silly dreams and always representing a safe home I can go back to. I'm incredibly lucky to have people like my parents supporting me regardless of my decisions and mistakes. Quero agradecer profundamente à minha esposa, Laís, pela infinita paciência para suportar todos os nossos desencontros e dificuldades. Obrigado, mo, minha vida seria completamente infeliz sem você. Te amo demais!

To everyone back home and from the bottom of my heart: thank you very much for everything, I hope I can always make you proud, this one is for you. Amo vocês.

All models are wrong, some are useful.

George Box, 1967

Contents

List of Figures

List of Tables

Chapter 1

Introduction

1.1 Motivation

Robotics has the potential to address problems that otherwise would be unsolvable, and history presents us with occasions where robot first responders would be essential, if not the only feasible solution. The outcome of the Fukushima Daiichi Nuclear Power Plant disaster could have been completely different if human-like machines were capable to enter the facility after the incident. On March 2011, an unexpected 15-meter Tsunami, followed by a major earthquake, hit the Japanese Power Plant. The natural disaster disabled the power supply and the cooling system of three of the main reactors inside the facility, causing the effective melt down of all three cores within the first three days [4]. It is estimated that if the cooling system could have been restarted from inside within 24 hours of shutdown, the radiation leakage could have been greatly reduced or completely avoided. However, because the deadly levels of radiation precluded human entry to the area following the incident, the Japanese government requested robots, such as the *Packbot* from *iRobot* [66], to enter the building to investigate the situation. These machines performed amazingly by recording video footage of the interior, taking pictures and gathering data, but they were still not able to perform the full range of physical tasks usually carried out by human workers. At the time, no legged robot of any sort was able to navigate the highly unstructured terrain, open doors, move debris, or even operate valves, whether fully or semi-autonomously, in a real environment.

Despite the remarkable recent progress in legged robotics research, machines are still far from performing physical operations as robustly as humans do every day. In light of such contrasting capabilities, one might ask how can we take advantage of this unparalleled human motor skill in order to augment robot performance? This pertinent question arises especially considering that humans exhibit amazing control proficiency despite the biological system characteristics. For instance, humans have over 200 muscles with very compliant structures and about only $10Hz$ force bandwidth, the sensory feedback can be as slow as $100ms$ or more, while the communication speed of neurons runs around $10^2 m/s$. Humanoid robots, on the other hand, have only 25 to 40 Degrees of Freedom (DoF) with actuators that can have over $50Hz$ bandwidth, control loops that can easily achieve $1kHz$ rates and electrical communication with speeds up to $10^8 m/s$ [24]. It is clear that, if we can harness this human control competence, we will allow legged robots to attain a new level of motor dexterity. A bipedal platform that can execute similar powerful physical tasks as the average human would be extremely valuable for field applications such as search and rescue or firefighting. However, executing high power dynamic motions such as opening a heavy door, throwing and swinging a sledge hammer in real situations requires a level of coordination that nearly all autonomous humanoid robots today cannot yet achieve. On the other hand, in direct teleoperation, the robot immediately gains access to the human's innate motor skills and knowledge of the world, in addition to allowing the operator to rapidly prototype new motions on the fly. The challenge here lies, however, on effectively transferring the motion data from human to robot and providing the operator with the apropriate feedback.

Instead of tracking individual joint trajectories and remapping them to robot coordinates such that the motion is visually similar to humans, in this Thesis, we focus on transmitting the *strategy* the operator uses for creating motion. We assume that this strategy can be described by a reduced model and a few fundamental elements such as the contact points location (feet position) and an augmented Center of Mass (CoM) state, the Divergent Component of Motion (DCM)[70]. The DCM is a composite variable given by the CoM position plus its time rate of change normalized by the system's natural frequency. Compelling experimental evidence suggests that the DCM, also know as Extrapolated Center of Mass (XCoM), [23] is a fundamental component humans regulate in order to balance and create motion [22]. Other authors evidenced similar state augmentation as a linear feedback law for disturbance rejection [77]. This concept was also developed in parallel by the robotics community under the name of Instantaneous Capture Point (ICP) [58]. This state represents the unstable portion of the CoM dynamics: if the DCM can be stabilized, then the CoM is guaranteed to remain within safe boundaries. Regulating the DCM as a balancing and stepping strategy has also been successfully implemented in several robot controllers [15][26] and stands as a promising mapping state for dynamic teleoperation of legged robots.

In this Thesis, we assume that if the operator can learn about the teleoperation coupled dynamics through feedback, then s/he can generate motions that are inherently stable or create recovery actions that consider both systems, the human body and the robot. This has been demonstrated by well-defined continuous systems such as in [8], where a the human is able to learn how to compensate the forces generated by an artificial potential field and stabilize the upper limb motion through optimizing joint impedance. But such adaptation to external dynamics has yet to be shown for hybrid systems with non-trivial contact force constraints such as legged robots. Additionally, a natural concern of motion mapping in teleoperation is if the reference trajectory generated is stable for the target machine. A legged walking system is discontinuous, from the intermittent impacts with the environment, highly nonlinear, from the coupled dynamics of multi rigid-bodies, and underactuated, due to the unilateral force constraints and friction characteristics imposed by contact with the ground. Linear control theory is not sufficient to provide a general sense of stability to theses systems. Similarly, stability in the sense of Lyapunov cannot capture the hybrid behavior and Poincaré return maps are extremely difficult to be defined. Authors usually resource to some sort of numerical definition of stability, which ultimately still suffers from the curse of dimensionality [56]. Thus, the general definition of bipedal stability is still an open and active problem in robotics and biomechanics research [20]. Hence, binding the teleoperation mapping law to an over-conservative metric of stability could greatly narrow the richness of robot motion and, in consequence, defeat the purpose of using a human operator. This work depicts our approach to achieve dynamic synchronization, including stance change and stepping. In this pioneering study, we show how the natural frequencies of the human and robot models play a key role on the feedback law and how external disturbances applied to the robot are transmitted to the operator through the Human-Machine Interface. We envision this work as the first step towards enabling machines to achieve the desired extreme motions required for power manipulation in unstructured environments.

1.2 Related Work

The work developed here fundamentally differs from the classic telerobotics problem with manipulators attached to a fixed base. Robotic manipulators are capable of transmitting the payload to the ground through the fixture, allowing them to exert arbitrary forces to the environment (only limited by the actuators). Legged robots, on the other hand, are required to deal with balancing when manipulating one's entire body to perform dynamic tasks. Thus, to take advantage of human motors skills, the required body-feedback that should be provided to the operator is fundamentally different from the force feedback from conventional bilateral teleoperation [64] as shown in figure 1-1.

Many researchers have attempted to access human motor skills by focusing solely on the kinematic mapping between operator and the target machine. In fact, trajectory generation for bipedal robots through retargeting of human motion has been extensively studied in robotics and computer graphics [76][18]. The majority of these studies utilize a full-body Motion Capture (MoCap) System that monitors the human kinematic data. This information is then transformed into trajectories in robot coordinates online [36] [29] [30] [45] [57] [12] [16] [9] [3] [40] or offline [35] [84] [85] [47] [48] [68] (see figure 1-2). On the other hand, instead of capturing the whole-body kinematic information, in this work, we focus on tracking only specific points that we assume to be fundamental for legged locomotion, such as the Center of Mass and feet spatial trajectories. Moreover, due to the vast differences between operator and robot, the motion stability is of prime concern during this unilateral teleoperation. Here the captured kinematic data has to be modified according to a simplified model and a safety metric (e.g. Zero-Moment Point and Linear Inverted Pendulum [83][82][67] or Machine Learning techniques [42][13]) such that the motion can be stably reproduced. In contrast, we argue that constraining the robot to a static controller and a safety metric considerably reduces the achievable motion limits. This occurs because, during exploration, the system will inevitably reach a user-defined stability boundary that is likely to be over-conservative due to the relative simplicity of the model when compared to the real system [56]. Thus, we intend to study how far a human operator can improve robot performance through appropriate feedback without imposing safety metrics. However, to the authors' knowledge, in very few studies the Human Machine Interface (HMI) provides meaningful physical feedback to the operator regarding the robot's performance in real-time. In [53][54] the authors provide force feedback to the operator and utilize Machine Learning techniques to develop an interesting method to teach a bipedal robot how to physically interact with another human while balancing. However, the study was limited to slow motions and it is unclear how to expand the technique to more complex dynamic behaviors that involve rough terrain and stepping. Alternatively, in [7][6] the operator is provided with vibro-tactile information about the state of balance of the legged robot. But this approach is also only valid for semi-static motions on flat terrain. In addition, vibration input is not only difficult to model, but it also increases human physical response time for requiring voluntary motor control from the operator (sensory input is not directly related to the motor action) [33]. Other unconventional approaches such as in [10][25] utilize Artificial Muscles to apply pressure over the operator's skin, providing information about the robot performance. This approach has similar disadvantages to the vibro-tactile feedback and has only been demonstrated for upper body control during time-insensitive tasks. Some commercial HMIs for Virtual Reality (VR) systems can provide vibration feedback to the user [71], while others, like the AxonVR [5], provides full-body support and force feedback. Differently from teleoperating a physical robot in the real world, the virtual environment is not required to obey real constraints. Additionally, the feedback law for these products is not publicly available, thus its usefulness for real life applications is still unclear. Yet, legged locomotion is governed by the intricate dynamics between the robot state, the contact forces with the environment and the feedback from its actions. Thus, the logical approach to effectively access human motor capacity is to appropriately map the kinematic *and* dynamic information from operator to robot and to close the teleoperation

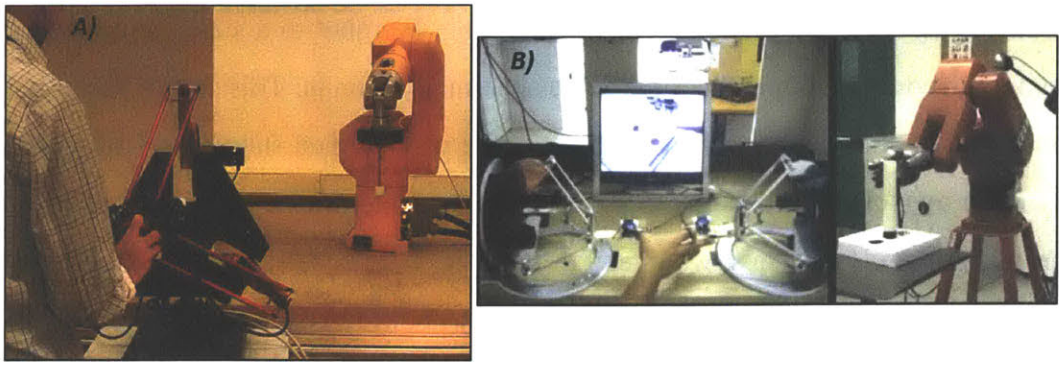

Figure 1-1: Bilateral teleoperation of fixed-base manipulators with force feedback [74][50]. The slave robot is not required to balance itself, thus it can apply arbitrarily large forces to the environment. This bilateral teleoperation scenario is fundamentally different from the whole-body bilateral teleoperation proposed in this thesis.

loop by providing the correct feedback to the operator online.

1.3 Research Contributions

As one of the very few studies in the literature regarding the whole-body coupling between human and humanoid robot, the main contribution of this work is to show the potential of such approach and, hopefully, motivate research directions that derived from it. Secondarily, we argue and experimentally demonstrate that a model-based approach to establish this force coupling between both system is required, and, particularly, that simple models are competent to bridge this connection, as is described in Chapter 4. A powerful outcome from this Chapter shows that is possible to dynamically teleoperate robots with substantially different scales from the human operator. Moreover, all the results obtained in simulation are reproduced in two physical systems, demonstrating the generality of the method.

Additionally to the academic contributions described in the previous paragraph, several technical contributions are also presented. First, we describe the design of a custom Human-Machine Interface that focus on capturing particular components of human motion at high-speed, and is also capable of physically applying forces to the operator. Effectively interfacing with the human body has often been shown to be very challenging. Moreover, we describe the design of two bipedal robots that are developed to perform highly dynamic motions: HERMES and Little HERMES. Both platforms represent a paradigm shift from

Figure 1-2: Unilateral teleperation of humanoid robots. In all these cases, the operator does not receive any feedback from the robot interaction with its environment, thus they have decoupled dynamics. In addition to the generally low motion capture rates, the robot is unable to perform fast motions from human input. Human operator and slave robot do not have synchronized change of support and stepping. (A) Offline motion retargeting from human dancer to the robot *HRP-2* robot [46]. (B) Online teleoperation of the robot *Mahru* using an IMU-based Motion Capture suit [65]. (C) Online teleoperation of the robot *NAO* from *Aldebaram Robotics* using an IMU-based Motion Capture suit [36]. (D) Online teleoperation of the robot *Jaxon* using an camera-based Motion Capture suit [31].

traditional high-gear-ratio robots that are enable to mitigate impacts that unavoidably occur during locomotion and manipulation. The ability to control the forces applied to the environment at high bandwidth is a fundamental requirement that is becoming more evident as the control of state-of-the-art robots becomes more sophisticated.

1.4 Thesis Organization

This Thesis is organized to break down the solution to the bilateral teleoperation problem into steps with increasing degree of complexity. First, in Chapter 2, we describe our procedure for capturing human data at high sampling-rates and motivate the idea of physically connecting the operator to the fixed world frame. The following step, in Chapter 3, depicts our first attempt to address whole-body teleoperation and the deployment of a human-like robot to scenarios that require physical work in addition to surveillance. In that Chapter, we show the design of the HERMES robot, a machine that utilize torque-dense actuators and is capable of Power Manipulation, such as striking a wooden door with a firefighter axe. We also discuss the limitations of the adopted model-free teleoperation approach, and motivate the requirement for the theoretical formulation developed in Chapter 4, the core contributions of this Thesis. We show how the scale and natural frequency of the reduced order model affect the teleoperation behavior and help the human synchronize with the slave machine. We evaluate the approach by controlling simulated robots of different scales using real-time motion data. This results are further extended to Chapter 5 to control a physical underactuated system, the Cart-Pole. Motivated by its similarity to the human walking model, the Linear Inverted Pendulum, we show that our proposed strategy allows the synchronization of systems with substantially different characteristic time responses. Next, in Chapter 6, we pinpoint design requirements for real bipedal robots that allows reliable torque control, fast force bandwidth and the ability to deal with unexpected impacts. Such characteristics are fundamental for robots that are required to perform dynamic tasks and robustly deal with the surrounding environment. Finally, in Chapter 7, we apply the theoretical formulation to Little HERMES, a small-scale bipedal robot capable of fast motions. We describe promising experimental results in which the robot is able to take steps in place, jump and deal with uneven terrain. The closing Chapter, Chapter 8, discusses the progress throughout the Thesis and highlights particular insights from the experiments, as well as other lessons learned, suggesting topics for future research directions.

Chapter 2

Capturing Human Motion Data

2.1 Introduction

Human motion can be physically described by a collection of states that define the body pose plus the contact points with the surrounding environment along with the respective interaction forces. To capture this information, the HMI is required to track the spatial position and orientation of selected Cartesian points (or joints) while monitoring the contact forces in real-time. To avoid corrupting the measured information, the Motion Capture (MoCap) system needs to be transparent to the user and as least intrusive as possible.

There are many commercial systems available for human tracking [78], including mechanical suits [69], inertial measurement unit (IMU) suits [73], and a variety of optical tracking systems [72][28]. Most mechanical suits measure the joint angles directly, offer fast acquisition times (often above $1kHz$ sample rates), low-noise and drift-free measurements using encoders, but restrict human range of motion and require correct sizing for each individual. IMU suits offer flexibility in operator dimensions and good range of motion, but suffer from low sample rates ($\approx 200Hz$), lower resolution, noise due to gyroscopic drift, magnetic interference, and mechanical noise from the compliant suit and human body. Optical systems provide the best range of motion, and if enough cameras and markers are used, the problems of occlusion and measurement noise can be filtered out. However, the acquisition time is limited by both the frame rate of the cameras ($360Hz$ for high end systems) and the image post-processing time (an additional 8 to $10ms$ in our experiments with

OptiTrack).

In this Thesis, because we require the ability to apply relatively large forces to the user (up to $120N$), we opt for the utilization of a custom mechanical suit that attaches to certain points of the human body, reducing the total number of sensors. This design allows high sampling rates (up to $3kHz$), necessary to capture fast motions, while maintain excellent accuracy ($< 1cm$) and drift-free readings.

2.2 The Balance Feedback Interface (BFI)

The Balance Feedback Interface (BFI) is a custom Human-Machine Interface (HMI) that physically connects the human operator to a fixed base via a series of passive and active joints that can apply large forces to the operator's torso. These forces provide the feedback information regarding the performance of the robot when it moves and interacts with its environment. In this Section, we describe two different versions for this device that were used for the experiments in this Thesis (see figure 2-1).

2.2.1 Balance Feedback Interface Version 1

This HMI, depicted in figure 2-2, is composed of three actuation modules, each with 3-DoF, two passive and one actuated (see Figure 2-3). The BFI allows unconstrained 6-DoF motion of the torso within the workspace and can apply forces that act on the operator's Transverse Plane. Thus, it can apply forces on the X^H and Y^H axis, as well as yaw moments around the vertical Z^H axis. Refer to figure 2-2 for a cartoon of the device with the operator and the device Computer Aided Design (CAD) picture.

The system is required to be transparent such that it will not largely disrupt human natural motion. In addition to the lightweight links, the actuation and transmission are designed to be highly efficient and, thus, backdrivable. A similar methodology was utilized for the design of Little HERMES and is explained in Chapter 6. Each module utilizes a brushless motor (*Maxon EC90 Flat* 48V). The timing belt transmission provides a torque amplification of 23:1. The required force to be applied to the human was determined by experimentally pushing the operator and determining the force required to induce a stepping motion. The commercial actuator was selected to achieve this required force level while reducing the transmission ratio (and reflected rotor inertia).

From figure 2-4 we see that the total force and moment applied to the operator is

$$\begin{aligned} \vec{F}_{total} &= \sum_{i=1}^{3} F_i \vec{u}_i \\ \vec{M}_{total} &= \sum_{i=1}^{3} F_i (\vec{r}_i \times \vec{u}_i). \end{aligned} \tag{2.1}$$

Where $\vec{u}_i$ is the direction of the force F_i applied by module i, and $\vec{r}_i$ is the vector between the estimated human Center of Mass (CoM) and the module i attachment point P_i. The third link of each module is designed to be long such that we can assume that the forces generated by the BFI exist only in the Transverse Plane for all experiments in this Thesis. The spacial position of the human torso can be derived from the forward dynamics of this parallel manipulator. This particular iteration of the BFI was utilized for the control of HERMES (Chapter 3) and the Cart-Pole (Chapter 5).

2.2.2 Balance Feedback Interface Version 2

The final iteration of the BFI design followed the same criteria as the previous one: transparent to the user and capable of applying large feedback forces to the operator. However, in order to increase the human workspace and to generate roll moment (Y^H axis) around the human Center of Mass, the structure of the HMI was modified as shown in Figure 2-6 and detailed view of each module in 2-7.

The Frontal Plane spacial position and orientation of the operator can be derived from the forward kinematics of the modules. For instance, from Figures 2-8 and 2-9, the CoM position is given by

$$\overrightarrow{CoM}_H = \begin{bmatrix} x_H \\ y_H \\ z_H \end{bmatrix} = \vec{P}_1 + \delta_1 \frac{\vec{P}_2 - \vec{P}_1}{|\vec{P}_2 - \vec{P}_1|},$$

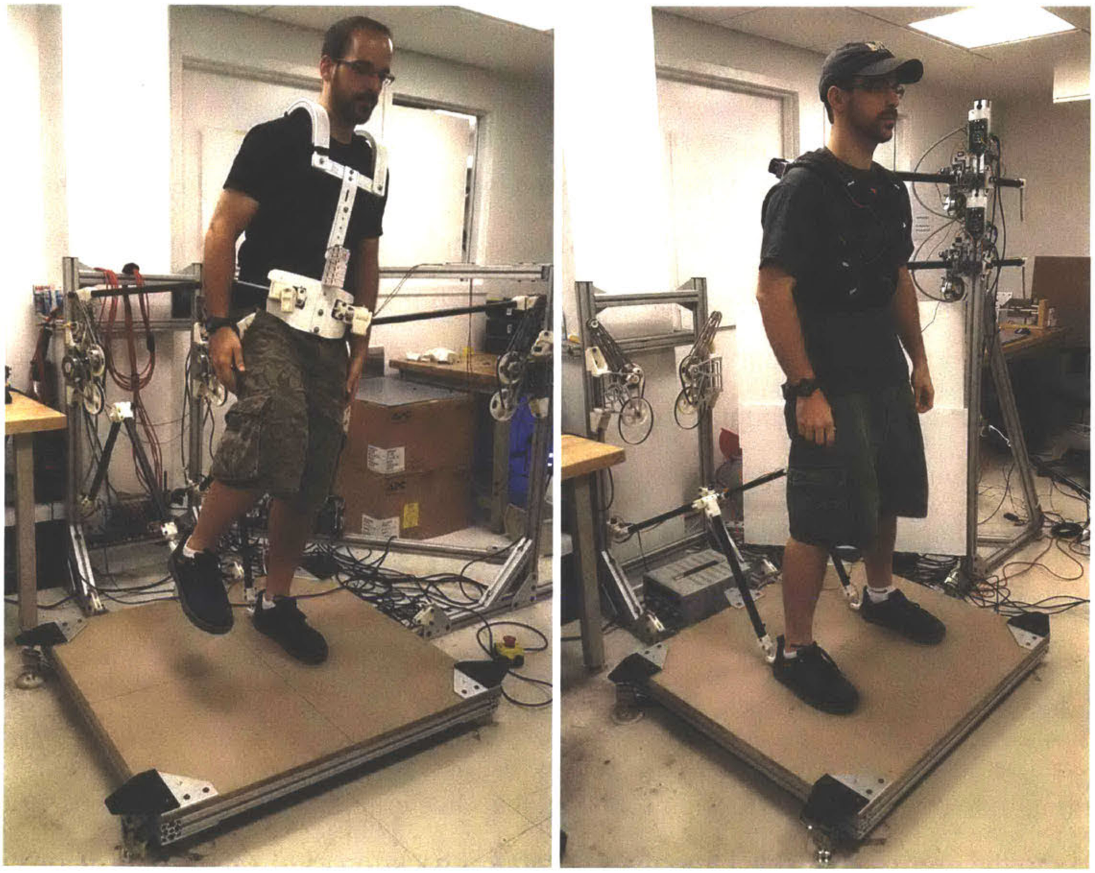

Figure 2-1: Human operator stands in the Balance Feedback Interface version 1 (left) and 2 (right). Left: This BFI is able to measure all 6-DoF of the human torso in addition to 3-DoF feet spatial position. It can also generate left-to-right and front-and-back forces, as well as yaw moments. Right: the final version of the BFI focus primarily on the frontal plane dynamics. It tracks torso 5-DoF (no yaw) and feet 3-DoF position. It can generate horizontal left-to-right forces and also roll moments. Both inputs are important for dynamic motions in the Frontal Plane.

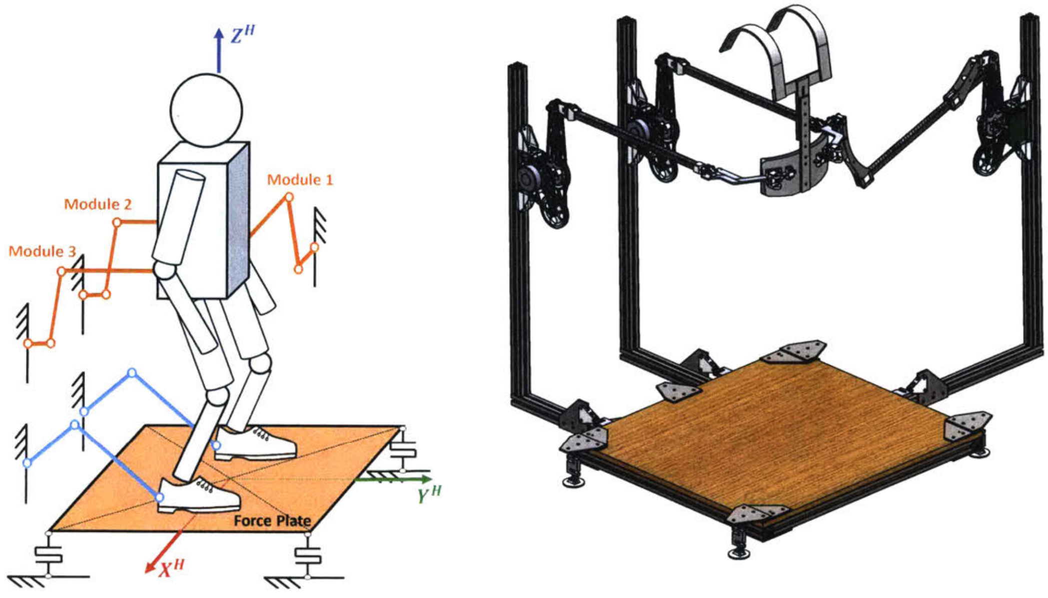

Figure 2-2: Left: Schematic of the Balance Feedback Interface. The linkages in orange track 6-DoF of the human torso in space and can also apply large forces to the operator's CoM. Simultaneously, the passive linkages in blue monitor the feet position. The human stands on a 6-axis force plate that measures the net forces applied by the legs to the ground. Right: The CAD of the Balance Feedback Interface with the custom force plate.

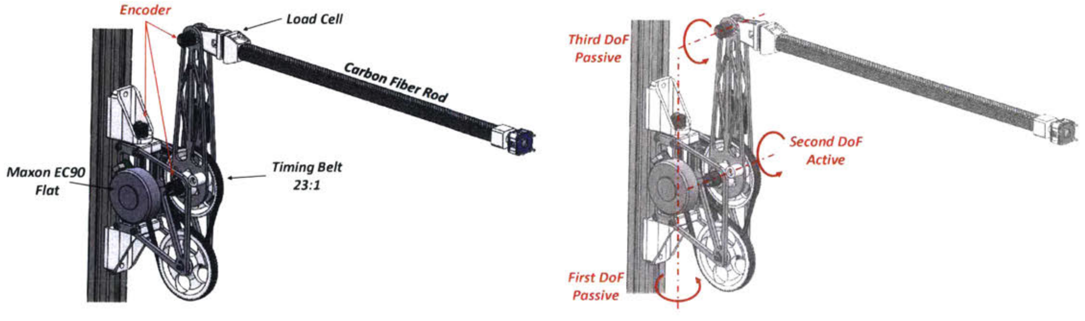

Figure 2-3: BFI modular 3DOF underactuated linkages. The first and third joints are passive while the second joint is driven by a brushless electric motor.

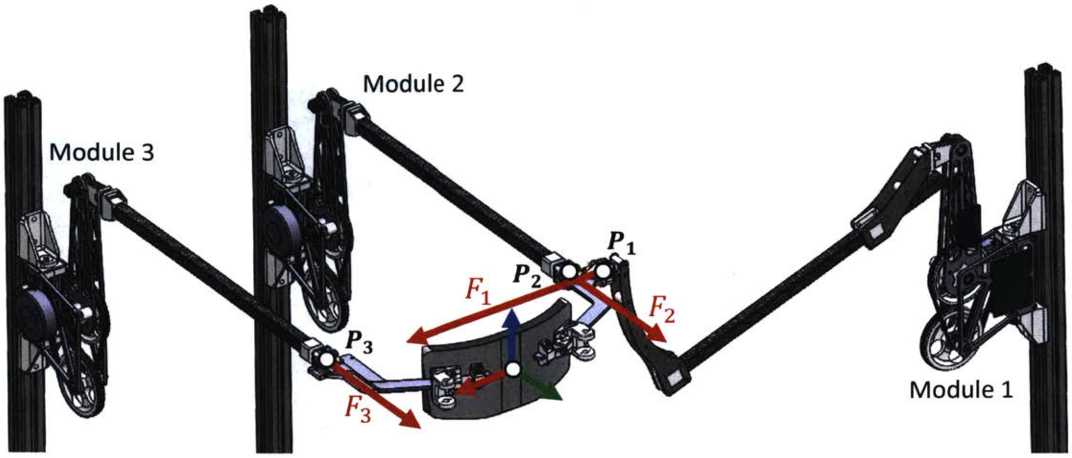

Figure 2-4: The parallel actuation scheme of the BFI modules. Notice that due to the passivity of the third joint, the torque applied by the motor mounted to the second joint of each module produces a force that is collinear with the last linkage.

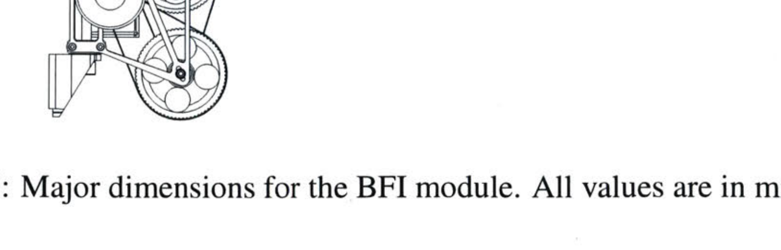

Figure 2-5: Major dimensions for the BFI module. All values are in millimeters.

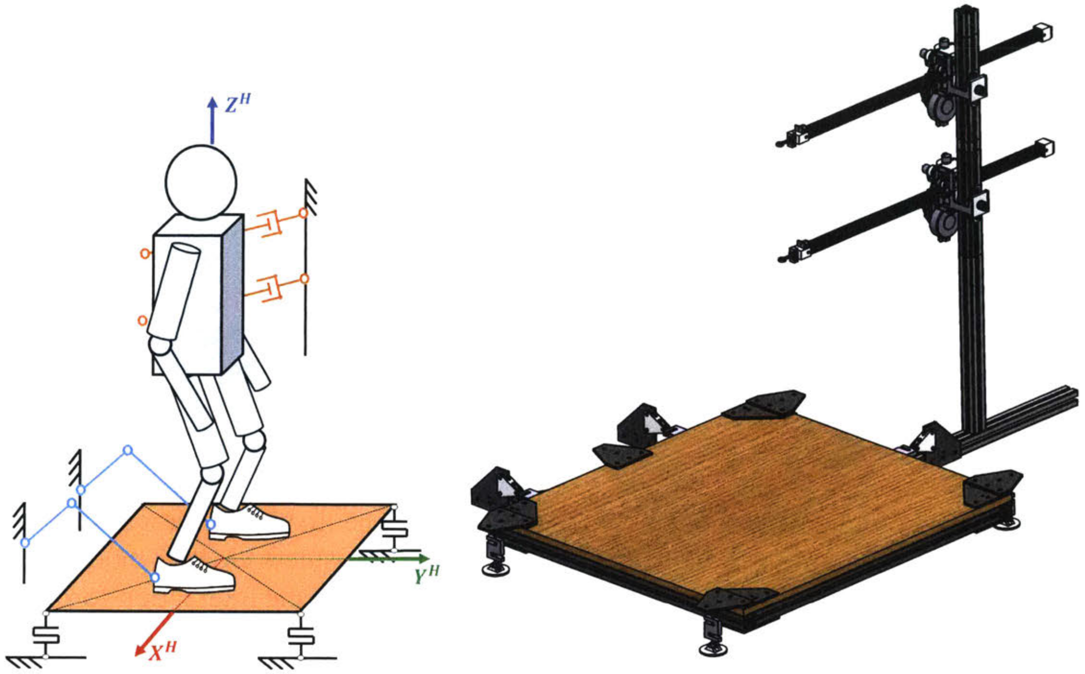

Figure 2-6: Schematic of the Balance Feedback Interface version 2. Left: The human operator stands inside the BFI and over a 6-axis force plate that measures the ground reaction forces. This device tracks 5-DoF human torso state and 3-Dof feet spatial position. Together, both underactuated arms can generate horizontal forces (in X_H) and roll moments (in Y^H). Right: the CAD of the constructed BFI utilized for experiments.

where δ_1 is the distance between the attachment point $\overrightarrow{P}_1$ and the body CoM, assumed constant in this Thesis. The Root Mean Squared Error (RMSE) for this estimation is $0.06mm$. Similarly, the torso roll is given by

$$\varphi_{yH} = tan^{-1}\left(\frac{P_{2x} - P_{1x}}{P_{2z} - P_{1z}}\right),$$

where P_{ix} and P_{iz} are the horizontal and vertical component of point i. The RMSE is $6 * 10^{-4} rad$. The total force applied to the operator is given by the same expression as in equation (2.1). This HMI was utilized to control Little HERMES as described in Chapter 7.

2.2.3 Force Plate

In order to measure the reaction forces between the operator and the ground, a large ($3ft$ by $3ft$) custom 6-DoF force plate is utilized. Figure 2-10 shows the concept for a planar

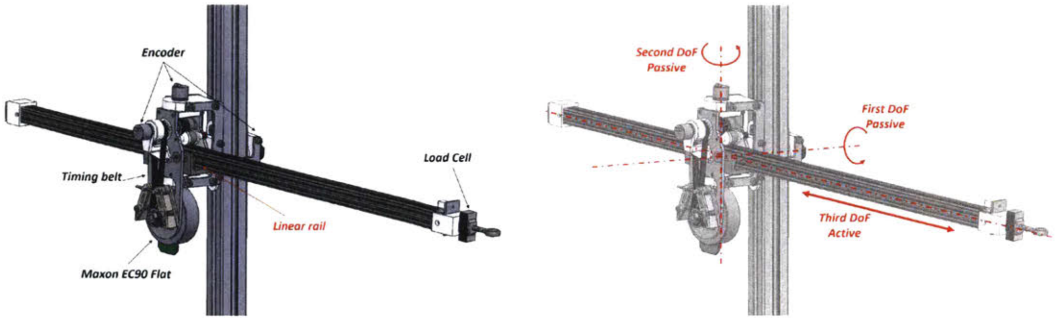

Figure 2-7: BFI modular 3-DoF underactuated linkages. The first two rotational joints are passive while the third joint is prismatic and actuated by a brushless electric motor. A load cell is mounted at the end of the last linkage in order to measure the interaction forces with the operator.

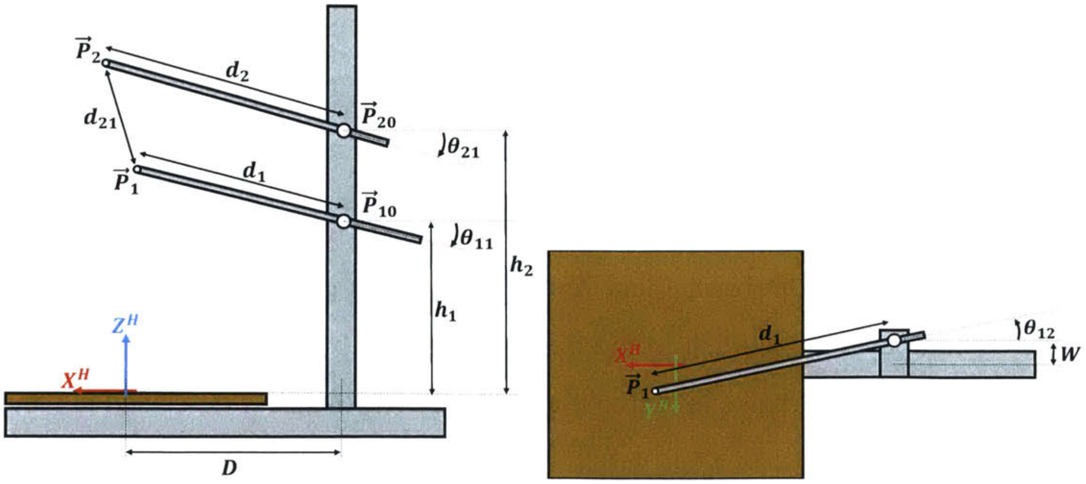

Figure 2-8: Parameters and definitions utilized for the BFI kinematics. The distances d_1 and d_2 are controlled by active prismatic joints in modules 1 and 2.

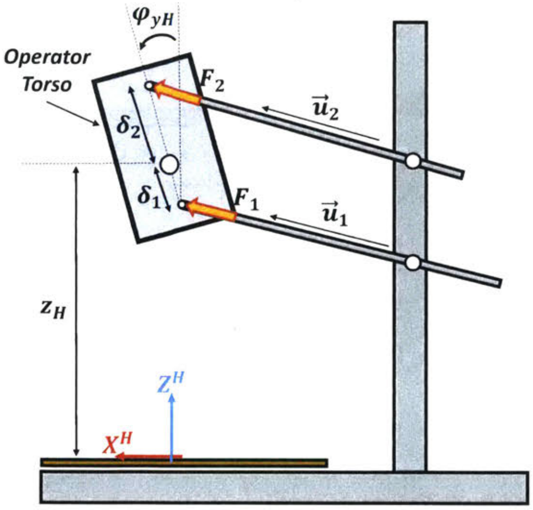

Figure 2-9: Representations of the forces F_1 and F_2 applied by the BFI. These forces are collinear with the directions $\vec{u}_1$ and $\vec{u}_2$ of modules 1 and 2, respectively. The spacial position of the operator's CoM can be estimated by a linear combination of points $\vec{P}_1$ and $\vec{P}_2$. A similar strategy can be utilized to estimate the roll angle φ_{yH}.

example of the force plate design. For the full 3D version, seven S-Type load cells (100kg CZL301C) were utilized as depicted in figure 2-11. Each load cell is mounted with a pair of ball-joint rod ends such that they only support one axis of the force. To calibrate the entire force plate, a Linear Least Squares regression approach was utilized based on the measurements of known weights (0 to $60kg$) placed at different locations, specially the extreme limits of the plate. Assuming that the net shear and normal components measured by the force plate are given by $\begin{bmatrix} F_{xH} & F_{yH} & F_{zH} \end{bmatrix}^T$ and that S_i corresponds to the force measured by load cell i, we can write the Least Square formulation

$$\begin{bmatrix} F_{xH} & F_{yH} & F_{zH} \end{bmatrix} = \phi^T \theta = \begin{bmatrix} S_1 & \ldots & S_7 \end{bmatrix} \begin{bmatrix} \vec{a}_x & \vec{a}_y & \vec{a}_z \end{bmatrix}.$$

Where $\vec{a}_{\hat{e}}$ is the column vector of parameters to be estimated for direction $\hat{e}$.

The operator Center of Pressure (CoP) is calculated by the weighted average of load cells 1 to 4. Thus, the X^H component p_{xH} is given by

$$p_{xH} = \frac{\sum_{i=1}^{4} S_i p_{xi}}{\sum_{i=1}^{4} S_i},$$

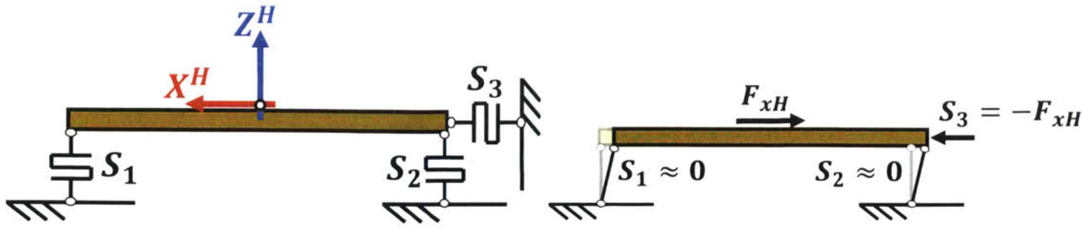

Figure 2-10: Planar concept for the custom force plate. Example with pure shear loading of the force plate. If the deformation of the sensor S_3 is small, load cells S_1 and S_2 will not measure any portion of the load F_{xH}. Normal loads are analogous, sensor S_3 is insensitive to the forces shared by S_1 and S_2.

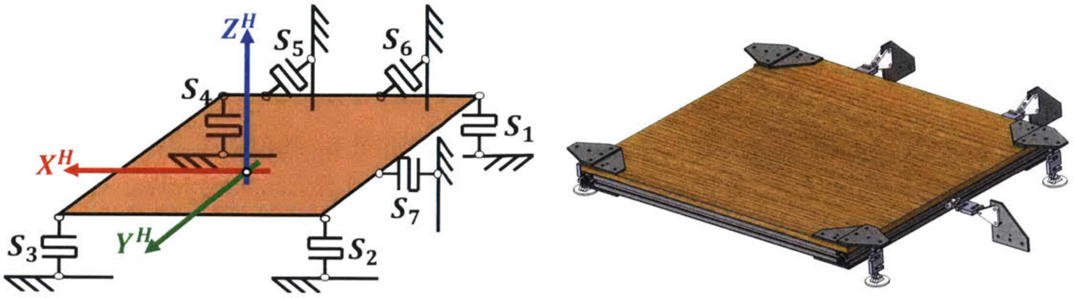

Figure 2-11: Design of the 6-axis custom force plate. This architecture follows the same principle of small deformation as the 2D case. Each load cell is mounted to rod ends such that these sensors just experience one direction of the applied load. An array of seven sensor measure the shear (F_{xH} and F_{yH}) and normal (F_{zH}) components of the human ground reaction forces.

where p_{xi} is the X^H coordinate of load cell i. The RMSE for the CoP estimation is $0.4mm$. The Y_H component is analogous.

2.2.4 Tracking feet position

The position of the operator's feet is measured in space utilizing a passive 3-DoF series of linkages with $12bit$ encoders (*Avago Technologies AEAT-6012-A06*) on each joint. The end-effector attaches to the operator's shoe utilizing a pair of self-aligning magnets (see the cartoon at Figure 2-12). The feet position are simply estimated by the forward kinematics of this serial-linkages device. Near nominal stance the system precision is on the order of $\pm 5mm$ with RMSE of $0.45mm$

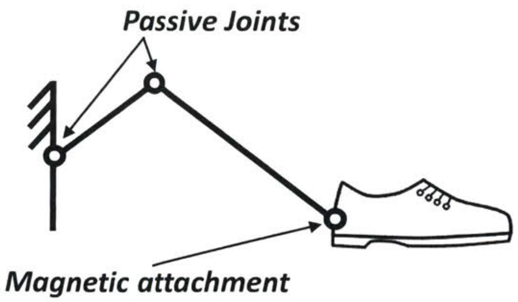

Figure 2-12: Cartoon representation of foot tracking linkages. Feet position can be estimated via forward kinematic of the passive linkages. Envisioning the safety of the operator, the shoes are magnetically attached to the structure. Thus, if the operator is required to step beyond the workspace of the BFI, the shoes will simply disengage.

2.2.5 BFI Controller and Schematic

The Balance Feedback Interface is controlled at $1kHz$ utilizing a *National Instruments cRIO9082* real-time target with programmable FPGA (Field Programmable Gate Array). Analog to digital (A/D) converter cards collect the readings from the load cells voltage amplifiers. A digital input/output card reads the joints angle values from the encoders in each module and on the feet tracking linkages. Figure 2-13 provides a detailed information regarding the BFI power and communication flow.

The feedback force applied to the operator is produced by current-based torque control of the brushless motors. For example, assuming negligible losses from the belt transmission, the force produced by module i for the second version of the BFI is given by

$$F_i = \frac{\tau_i}{r_p} = \frac{i_{mi} k_T}{r_p}, \tag{2.2}$$

where, τ_i is the torque produced by motor i utilizing an armature current i_{mi} and a torque constant k_T. Parameter r_p specifies the radius of the pulley utilized for the actuator transmission. Figure 2-14 shows the response for a step force applied to the operator with $\approx 42Hz$ bandwidth (notice this includes the human compliance). Figure 2-15 shows the comparison between the commanded force achieved via equation (2.2) and the force measured using the module load cell during one of the experiments when the operator teleoperates a bipedal robot as described in Chapter 7. The RMSE for this force control is about $11.2N$, which we assume is due to friction in the transmission.

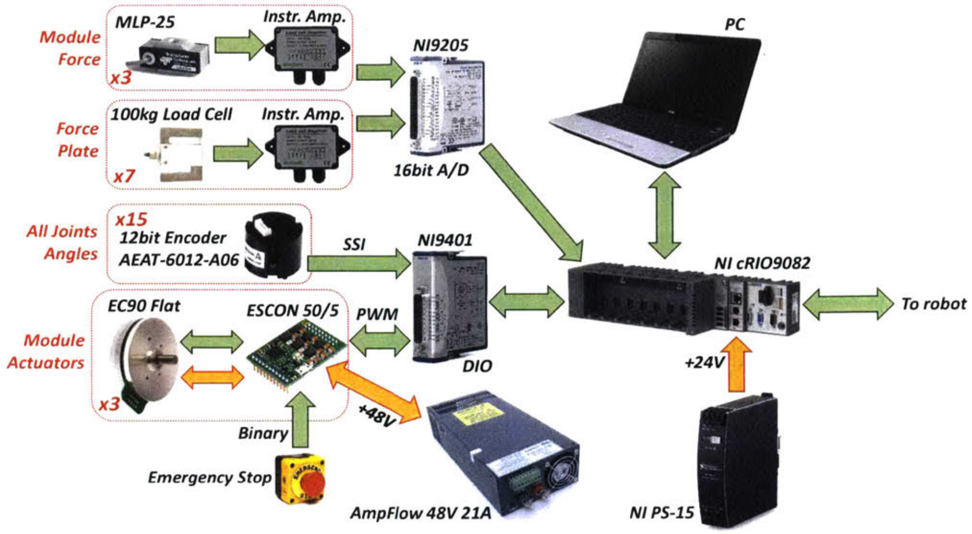

Figure 2-13: Electronic connections for the BFI. Red arrows indicate high power connections while green arrows shows low power communication flows. Bidirectional arrows indicate flow of power/information on both ways.

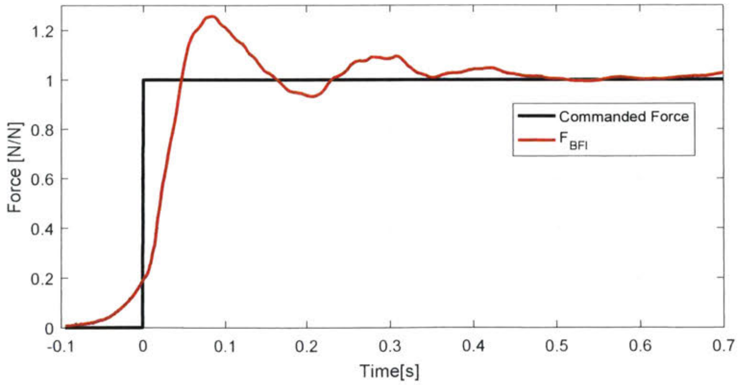

Figure 2-14: Response for a step commanded force applied to the operator. Notice that this response also includes the compliance of the BFI and operator attachment.

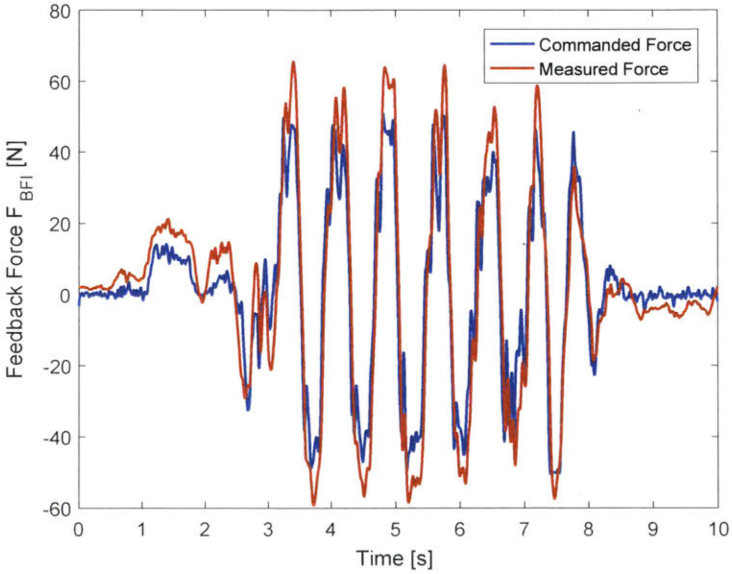

Figure 2-15: Comparison between the commanded F_{BFI} force versus the measured value from the load cell during one of the experiments. The efficient transmission and low reflected inertia allows reliable current-based torque control of the brushless motors at high bandwidth. We assume that small differences are due to unmodeled friction and model parameter errors.

Chapter 3

Proof of Concept: The HERMES System

3.1 Introduction

The nuclear disaster that took place at the Fukushima Daiichi Power Plant exposed the inability of state-of-the-art legged robots to perform human-like tasks in unstructured environments. Legged robots did not possess the autonomy or the motor skills required to navigate such challenging terrain and perform physical power manipulation tasks such as moving heavy debris or swinging a sledge hammer.

In light of these challenges, this Chapter depicts the development of the HERMES humanoid robot, a powerful bipedal system teleoperated through a whole-body Motion Capture Suit and a bilateral feedback Human-Machine Interface, the Balance Feedback Interface (BFI). This system represents the first approach for addressing the deployment of robots to dangerous scenarios that require physical work in addition to surveillance. By capturing innate dynamic upper body coordination abilities of the human operator, during experiments the robot was able to successfully perform a variety of power manipulation tasks such as breaking through a plaster wall, using an axe and operating an extinguisher to put out a fire. These promising results show that the HERMES system is a step towards a generalized architecture that can be potentially adapted to future disaster response robots. However, the system does not represent the complete solution to the whole-body teleoperation problem. In the end of the Chapter, we justify the necessity to expand the work done with the HERMES system to include knowledge about the robot dynamics, allowing the

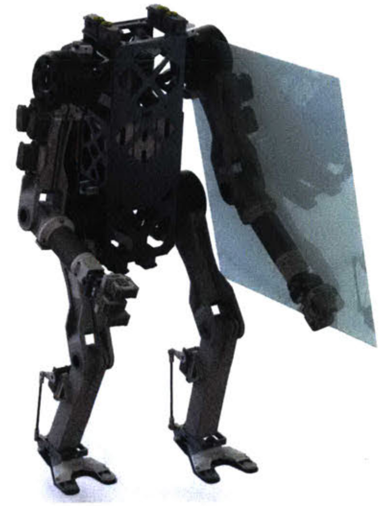

Figure 3-1: Power Plane representation of the HERMES humanoid robot left arm: the limb has six degrees of freedom but high power actuators drive only two, composing a plane. The remaining four auxiliary Degrees of Freedom are actuated by low power actuators.

teleoperation strategy to be used to make the robot take steps and walk.

3.2 System design

3.2.1 HERMES Humanoid Robot

HERMES physical layout is based on the Power Plane assumption for power manipulation: each limb has six degrees of freedom but high power actuators drive only two, which compose a plane, as depicted in figure 3-1. High-torque slower motors (*Dyanmixel MX-106*) that reorient the Power Planes, control the remaining four joints. Uniform power in all directions can be achieved by assuming that the machine is able to move around the environment. This design criterion reduces the number of large actuators because the robot will rarely need to generate high power motions in many directions while maintaining a single posture. Additionally, a collection of design features allows the machine to be robust against impact that unavoidably occur during normal operation. A combination of motor high torque capability, low gear ratio and low limb inertia (including rotor reflected inertia) grants the machine the ability to properly control task-space force from motor current and limb kinematics alone. By not using rigid force sensors, the robot can handle unexpected

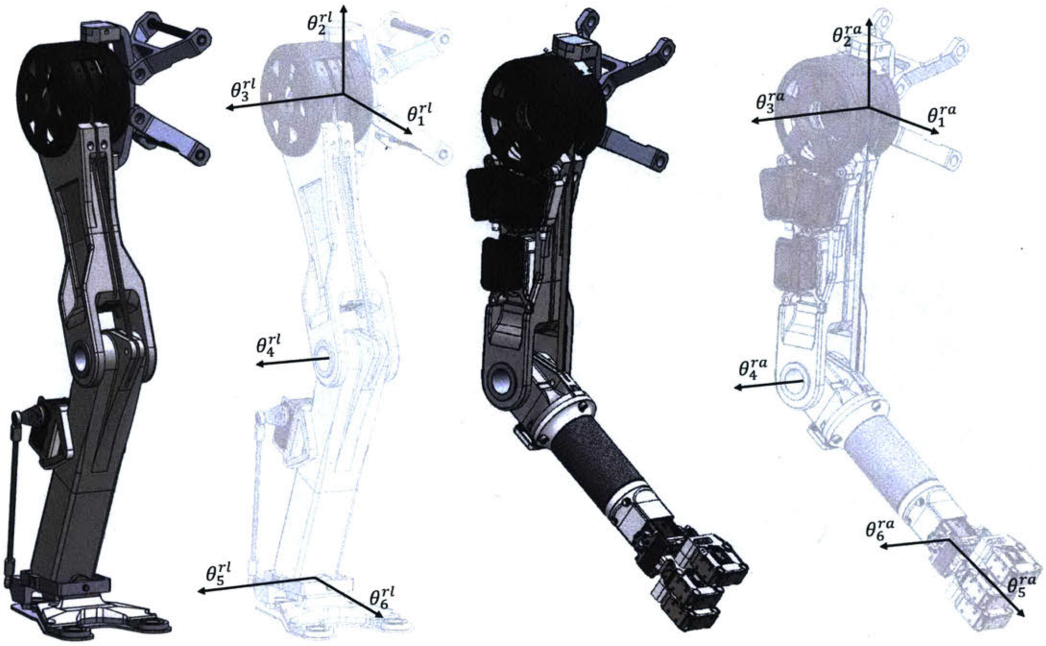

Figure 3-2: Axis of rotation of the Degrees of Freedom of HERMES' limbs. The hip/shoulder are composed of a three DoF semi-spherical joint with remote rotation axis θ_1^{rl}, the knee/elbow have each one DoF and the ankle/knee have two DoF. The ankle pitch θ_5^{rl} and roll θ_6^{rl} are driven by a differential actuation scheme.

impulsive load by programmed impedance [63][81]. This design achieves high bandwidth (~80 Hz) compared to conventional Series Elastic Actuators (25-35 Hz) [60]. Figures 3-2, 3-3 and 3-4 depict the Degrees of Freedom and the actuation scheme for the robot's limbs. The hip/shoulder are composed of a three DoF semi-spherical joint with remote rotation axis θ_1^{rl}, the knee/elbow have each one DoF and the ankle/knee have two DoF. The ankle pitch θ_5^{rl} and roll θ_6^{rl} are driven by a differential actuation scheme. Detailed design process for a similar machine, Little HERMES robot, is presented in Chapter 6.

Finally, HERMES is required to perform power manipulation either with or without tools, but not to the extent of human-level dexterity. The three-fingered underactuated gripper is driven through Bowden cables by motors mounted on the upper arm (see Figure 3-5 and 3-8 , item (7)).

The robot Center of Pressure is estimated by six load cells (*Futek LLB400 FSH03891*, three per foot) mounted to the bottom of the feet as shows in figure 3-9.

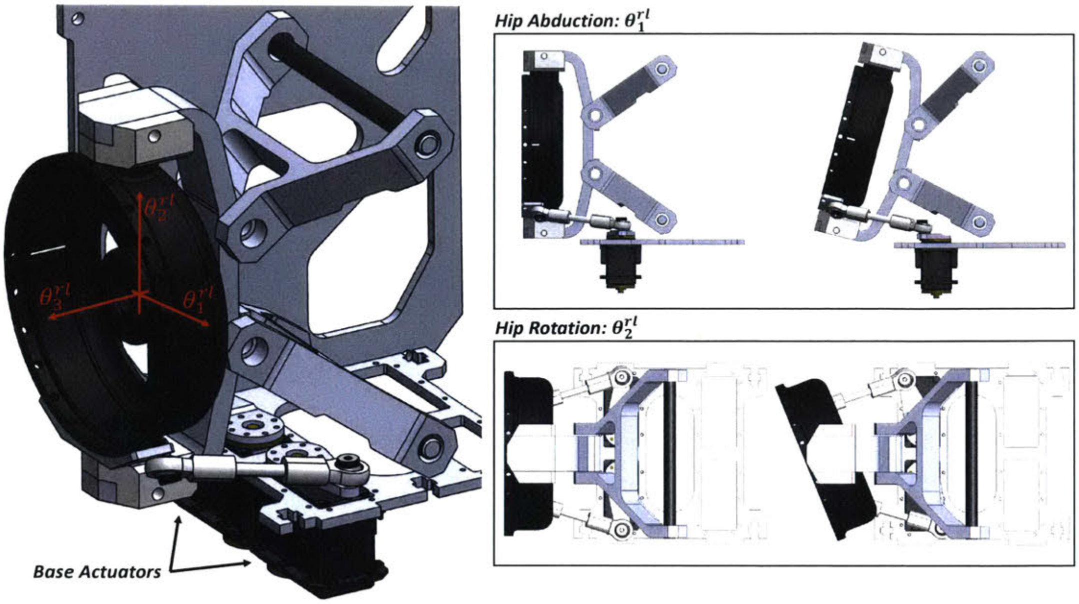

Figure 3-3: Detailed view of the hip semi-spherical joint. A four bar linkage performs hip abduction around a remote axis, as depicted in the top-right figure. Hip ab/adduction and in/out rotation are accomplished by a differential actuation scheme of the base motors.

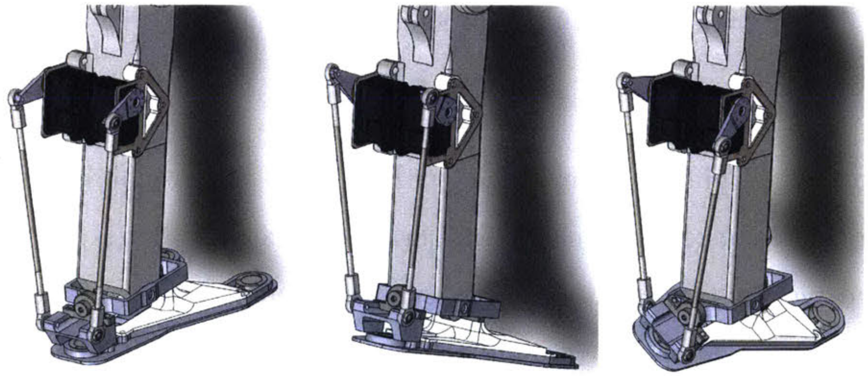

Figure 3-4: Detailed view of the ankle differential actuation for pitch θ_5^{rl} and roll θ_6^{rl}.

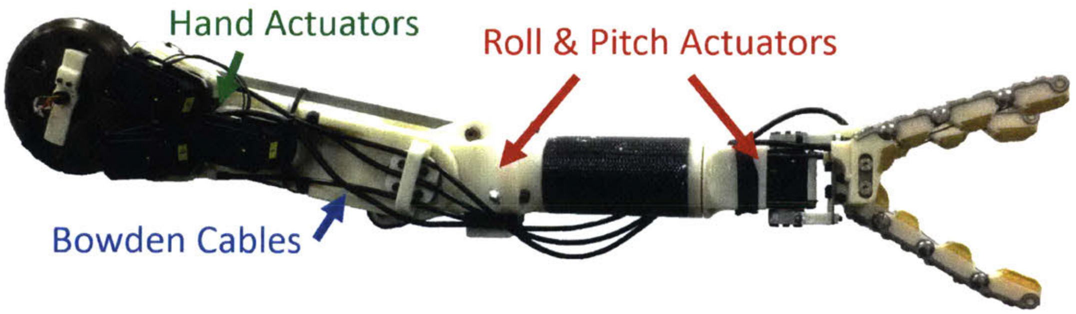

Figure 3-5: Detailed view of the arm design. The fingers are driven via Bowden cables by actuators mounted on the upper arm.

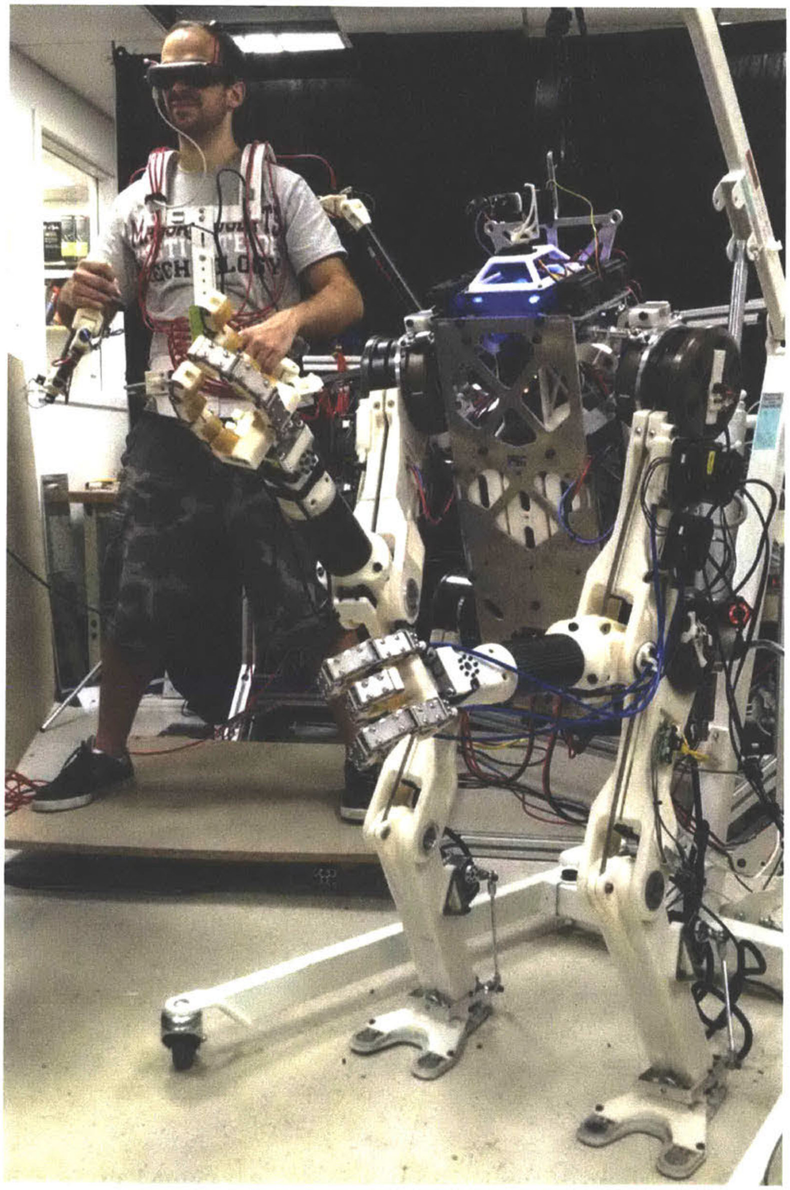

Figure 3-6: Picture of the proposed whole-body teleoperation system composed of the Human-Machine Interface as the Master system and the HERMES humanoid robot as the Slave System.

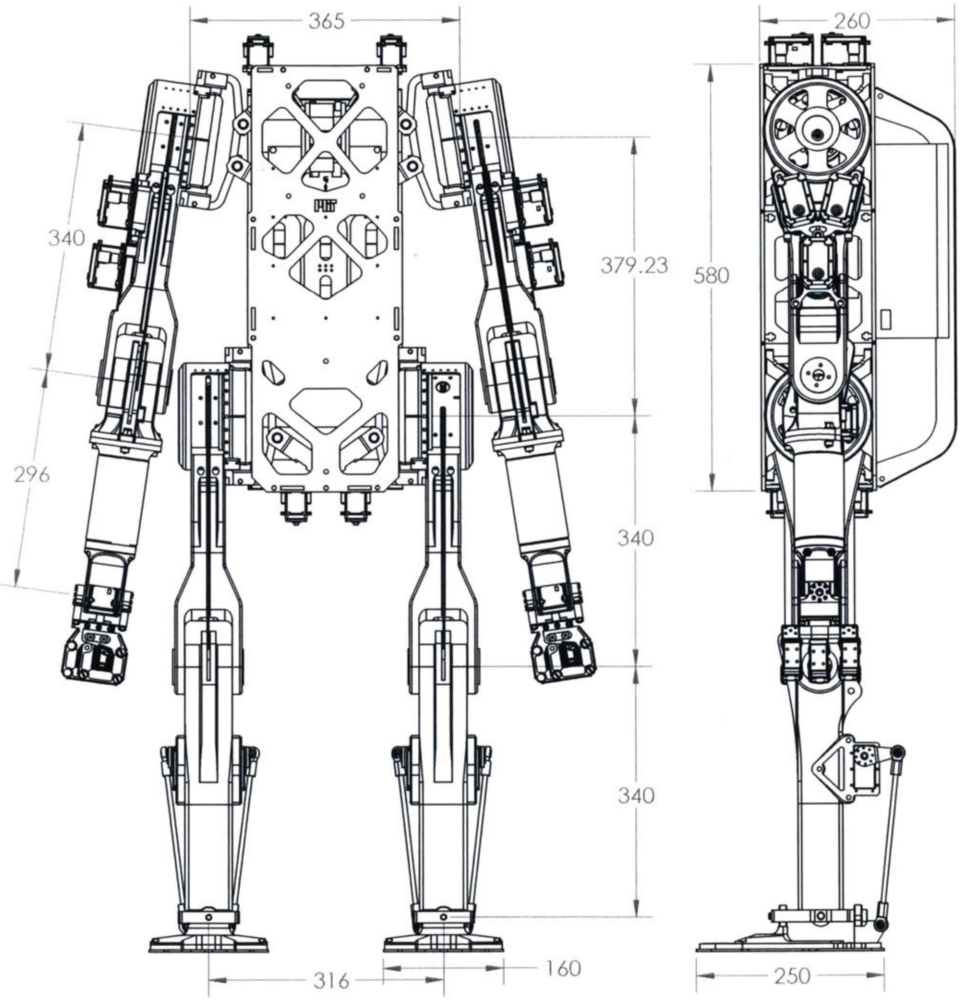

Figure 3-7: Dimensions of the HERMES robot. All values are in millimeters.

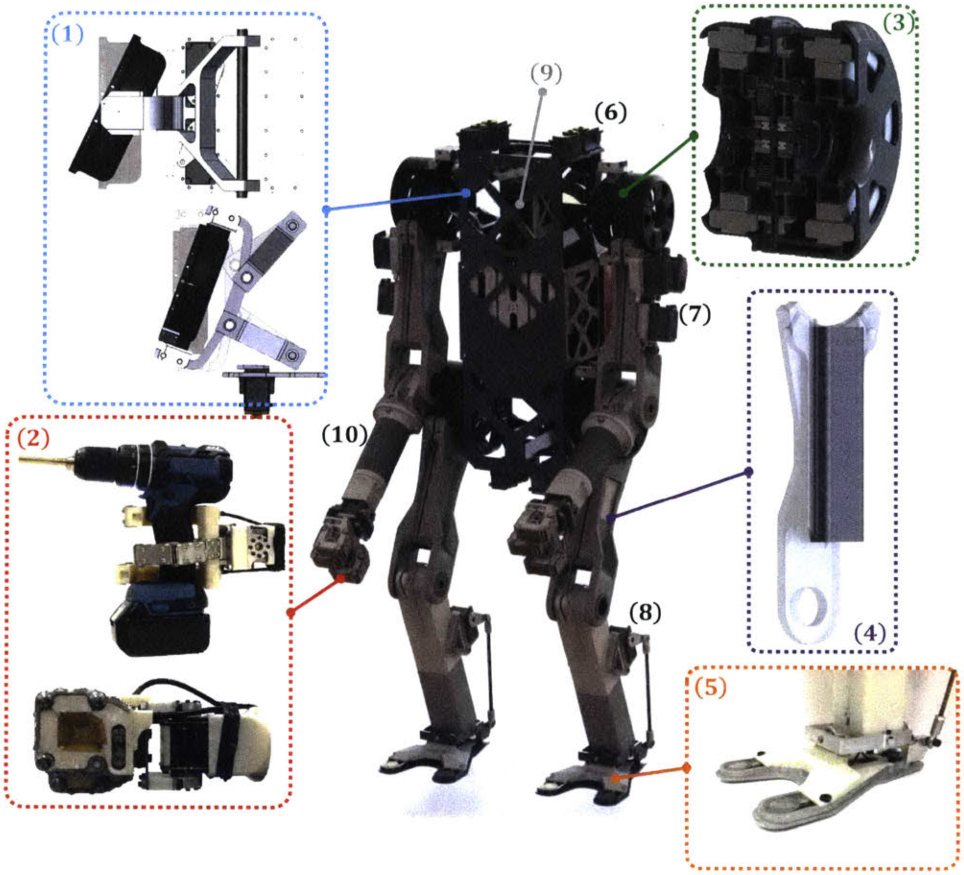

Figure 3-8: Key features of the HERMES humanoid design. The overall design of the HERMES robot incorporates several features unique to the power manipulation tasks. (1) Power plane actuator modules for each shoulder and hip are positioned by a 4-bar linkage that approximates spherical movement; (2) Three-fingered gripper that can grasp and operate common power tools. When closed, it is robust to impacts; (3) Coaxial Proprioceptive actuators drive the two power plane joints per limb; (4) Limbs are constructed with carbon-fiber tubing with an ABS plastic shell for high strength per weight; (5) Each foot has three embedded load cells that measure the robot Center of Pressure. The ankle uses a gimbal mechanism for rotation in two axes; (6) Compact servomotors drive two axes of shoulder rotation (yaw and roll) to reposition the proprioceptive actuation module.; (7) Compact servomotors drive the fingers through Bowden cables and are placed proximal to the body; (8) Two compact servomotors drive the ankle roll and pitch through a parallel gimbal mechanism. (9) The aluminum body cage is optimized for high stiffness and reduced weight. Power electronics for the Proprioceptive Actuators are located inside the cage. The Speedgoat xPC Target embedded computer is mounted inside a backpack enclosure; (10) Lightweight carbon-fiber forearm.

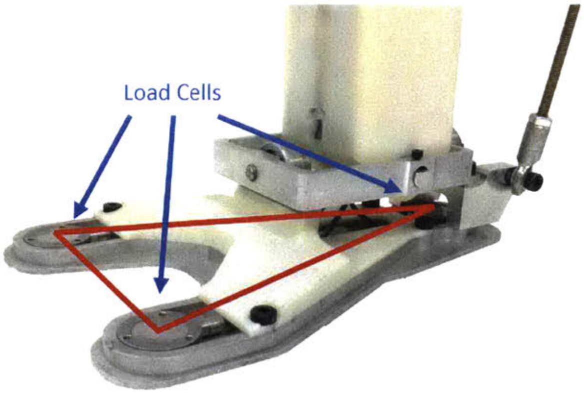

Figure 3-9: Detailed view of the load cell array mounted to HERMES' foot. These sensors are utilized to estimate the robot's Center of Pressure.

3.2.2 The Human-Machine Interface

This HMI is subdivided in two systems: (1) the Balance Feedback Interface (BFI) as described in Chapter 2 and (2) a low-latency mechanical Motion Capture (MoCap) suit. The MoCap suit is a passive exoskeleton device that monitors human end-effectors (hands and feet) positions and orientations relative to the torso. This low-latency device can achieve extremely high sampling rates (up to 10 kHz) when compared to commercial products [73][28], and avoids occlusion problems typical of camera-based systems. These are features required to achieve teleoperation of sudden high-speed motions.

3.3 Model-Free Teleoperation

This Section describes the feedback force based on a model-free strategy. This law does not require the adoption of a model for the robotic system because the Center of Pressure can be measured directly from the load-cells mounted on the robots feet. Hence, the feedback law is experimentally determined by the relative position of the CoP inside of the support polygon.

3.3.1 Control Strategy

Motion of the operator is mapped to the robot with modification on the task space level. First, the human hand positions relative to the body are scaled to the robot proportions

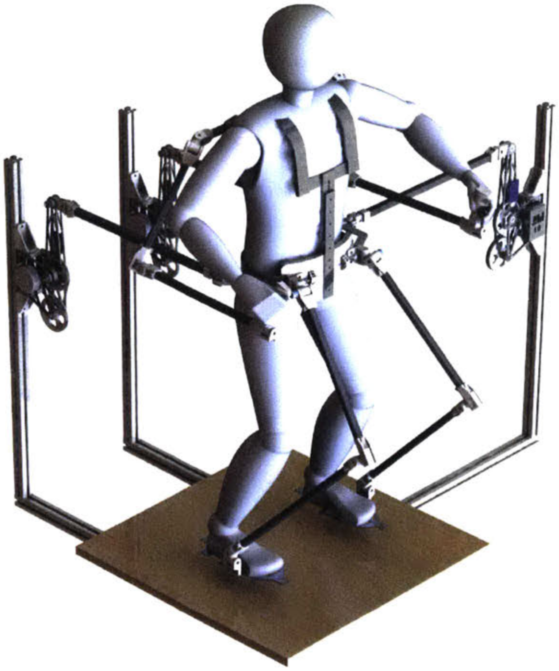

Figure 3-10: Human-Machine Interface including the Balance feedback interface (BFI) and Motion Capture (MoCap) suit.

using the ratio of arm lengths. Shoulder angles are directly mapped and elbow angles for the robot are computed from inverse kinematics.

$$\Delta\overrightarrow{X}_R^{Hand} = \frac{L_R^{Arm}}{L_H^{Arm}}\Delta\overrightarrow{X}_H^{Hand} \tag{3.1}$$

$$\Delta\overrightarrow{\Phi}_R^{Hand} = \Delta\overrightarrow{\Phi}_H^{Hand} \tag{3.2}$$

By using this method, the first-person camera view of robot arms shown to the operator appears in the same configuration as their own. The torso is mapped using two different methods. Horizontal motion in the Sagittal Plane of operator (Δy_H^{Hip}) corresponds to robot torso pitch ($\Delta\varphi_R^{Torso}$) . When the operator hips shift forward, the robot bends forward at the hips. Horizontal motion in the Frontal plane of the operator (Δx_H^{Hip}) corresponds similarly to horizontal movement of the robot hips (Δx_R^{Hip}).

$$\Delta\varphi_R^{Torso} = \alpha\Delta y_H^{Hip} \tag{3.3}$$

$$\Delta x_R^{Hip} = \beta\Delta x_H^{Hip} \tag{3.4}$$

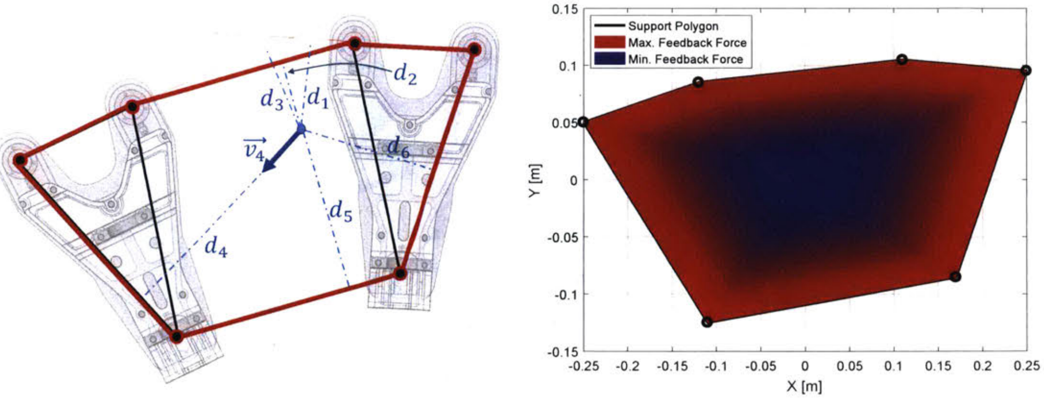

Figure 3-11: Left: Support polygon is the convex hull of the 6 contact points. The blue dot is the position of the robot center of pressure. Right: Feedback force magnitude visualized as a potential field. When the robot CoP is the near the edge of the support polygon, the feedback force applied to the human operator is at its maximum (red regions). Blue regions indicate near zero feedback force.

The robot is equipped with a stereo vision camera mounted according to human anatomic eye position. This camera follows the orientation of the operator's head in yaw and pitch, measured by the vision goggles worn by the operator, completing the immersive visual experience. Fig. 3-14-E and 3-14-F shows the camera view transmitted to the operator.

The relative position between the robot's Center of Pressure on the ground and its support polygon give an estimate of the stability of the robot in quasi-static standing [75]. This single metric is used to provide information about the robot's risk of tipping to the operator, through force feedback. The closer the robot CoP moves to the edge of the support polygon, the larger the magnitude of force applied to the operator according to equation (3.5)) and the overall force feedback map is shown in Fig. 3-11.

$$\vec{F}_{BFI} = -K_{BFI}\sum_{i=1}^{6}\frac{\vec{v}_i}{d_i} \tag{3.5}$$

3.3.2 Experimental results

For the system evaluation, the operator was instructed to stand in a comfortable position within the Balance Feedback Interface. Next, the startup sequence includes (1) the calibration of robot and human sensor readings (joint angles and force sensors), (2) test operation of individual robot joints, and (3) setting the robot in a nominal standing position with the knees slightly bent. During all experiments, a trained team member monitored two emergency stop switches that would shut off the robot and Balance Feedback Interface in the case of danger for the operator.

Balancing Experiments

The experienced human operator was instructed to try to balance the robot by any means without stepping, in response to several type of disturbances. The operator was not given visual or auditory feedback. To evaluate the performance of this strategy for balancing, three experiments were conducted:

1. Impact disturbance: A foam hammer was used to strike the back of the robot to provide an impulse disturbance at a random time, this is pictured in subfigure 3-12-A.
2. Inertial disturbance: The operator was instructed to rapidly swing their arms upwards with elbows straight, causing the robot to replicate the motion and induce a self-disturbance. See subfigure 3-12-B.
3. Unexpected loading disturbance: The operator was instructed to extend their arms forward with elbows straight such the robot replicated the pose. A weight of 2.9 kg was suddenly placed on the robot hand to induce a shift in the robot Center of Mass and Center of Pressure. See subfigure 3-12-C.

These three example scenarios illustrate how the Balance Feedback Interface (BFI) transmits to the human operator the general disturbances experienced by the robot utilizing a model-free strategy. The first experiment regards sudden impact from a rubber mallet. Here, the robot is struck from behind by an impulsive force that shifts the CoP of the machine. Fig. 2(A) shows the displacement of the Center of Pressure (CoP) and the resulting feedback force F_{BFI} produced. The plot also depicts the edge of the support polygon and the impulsive force measured by the instrumented hammer. The second experiment in subfigure 3-12-B, shows the result of a reactive torque on the body caused by the fast swing of

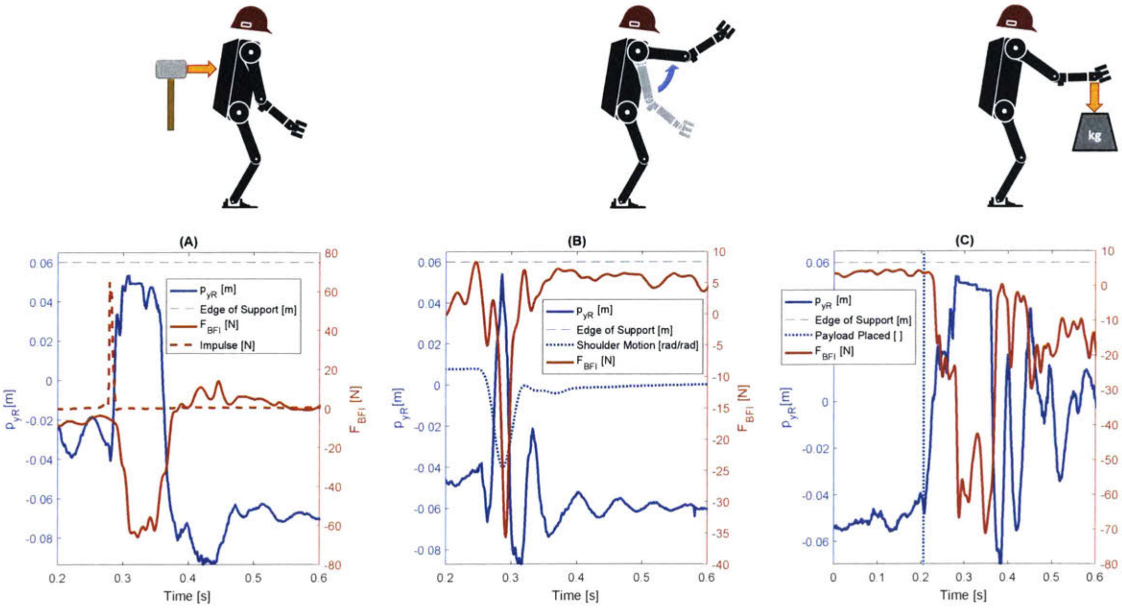

Figure 3-12: Stabilization trajectories during balancing experiments. (A-C) depict relevant signals, including robot CoP trajectory p_{yR} and the feedback force F_{BFI}, for three different perturbation conditions. (A) Hit from behind; (B) Arm swing; (C) Sudden payload. The robot was stabilized in all three experiments. Notice that, depending on the human input, there may exist an equilibrium position with non-zero (but small) BFI force, as shown in case (C).

the upper limbs. In the third experiment in subfigure 3-12-C, a $2.9kg$ payload is suddenly placed at the robot's hand when the arms were fully extended. Again, the addition of the extra mass to the limb shifts the CoP of the robot and generates feedback information to the operator. Provided this force feedback, the human is able to readjust the posture of the robot back to a safe configuration. In all these situations, the CoP proximity with the edge of support represents a level of danger, and this information is transferred through force applied by the BFI to the human's hip. The human performs correcting actions that allow the robot to balance and stay upright. Notice that the steady state feedback force F_{BFI} may not converge to zero due to friction in the transmission or minor inputs that are neglected by the operator.

Other Experiments

In addition to the balancing experiments, the directly teleoperated humanoid system is also able to complete other simple tasks, such as:

Figure 3-13: Manipulation examples. Crushing a can, operating a power drill and pouring water into a cup.

1. Fine manipulation: Figure 3-13 shows examples of manipulations conducted such as crushing an empty can, operating a handheld power drill, opening a bottle and pouring water into a cup. Subfigures 3-14-(D1-D3), show the double handed manipulation of a plastic bat, a task that involves both position and force control due to the closed kinematic chain formed by the robot arms and the rigid bat.

2. Firefighting: An operator trained in fire extinguisher use was commanded to teleoperate the robot to perform firefighting using visual feedback from the camera feed. The robot was remotely located from the operator. The fire was initiated and controlled by a professional firefighter, using propane bubbled through a water trough. This experiment is shown in Fig. 3-14-(C1-C3). The first-person view from the robot is shown in Fig. 3-14-F.

3. Power Manipulation: for instance swinging an axe to strike a simulated wooden door and punching through sheet rock wall. Subfigures 3-14(A1-A3) show the time-lapse of the axing motion while the punching sequence is shown in 3-14(B1-B3). Subfigures 3-14(E) and (F) show the first-person view from the robot embedded camera that the operator uses as feedback.

3.4 Why is this approach insufficient?

The HERMES System successfully demonstrates that a model-free teleoperation approach is sufficient to achieve simple behaviors such as the ones descried in this Chapter. These motions mostly involve upper-body control during semi-static conditions and completely

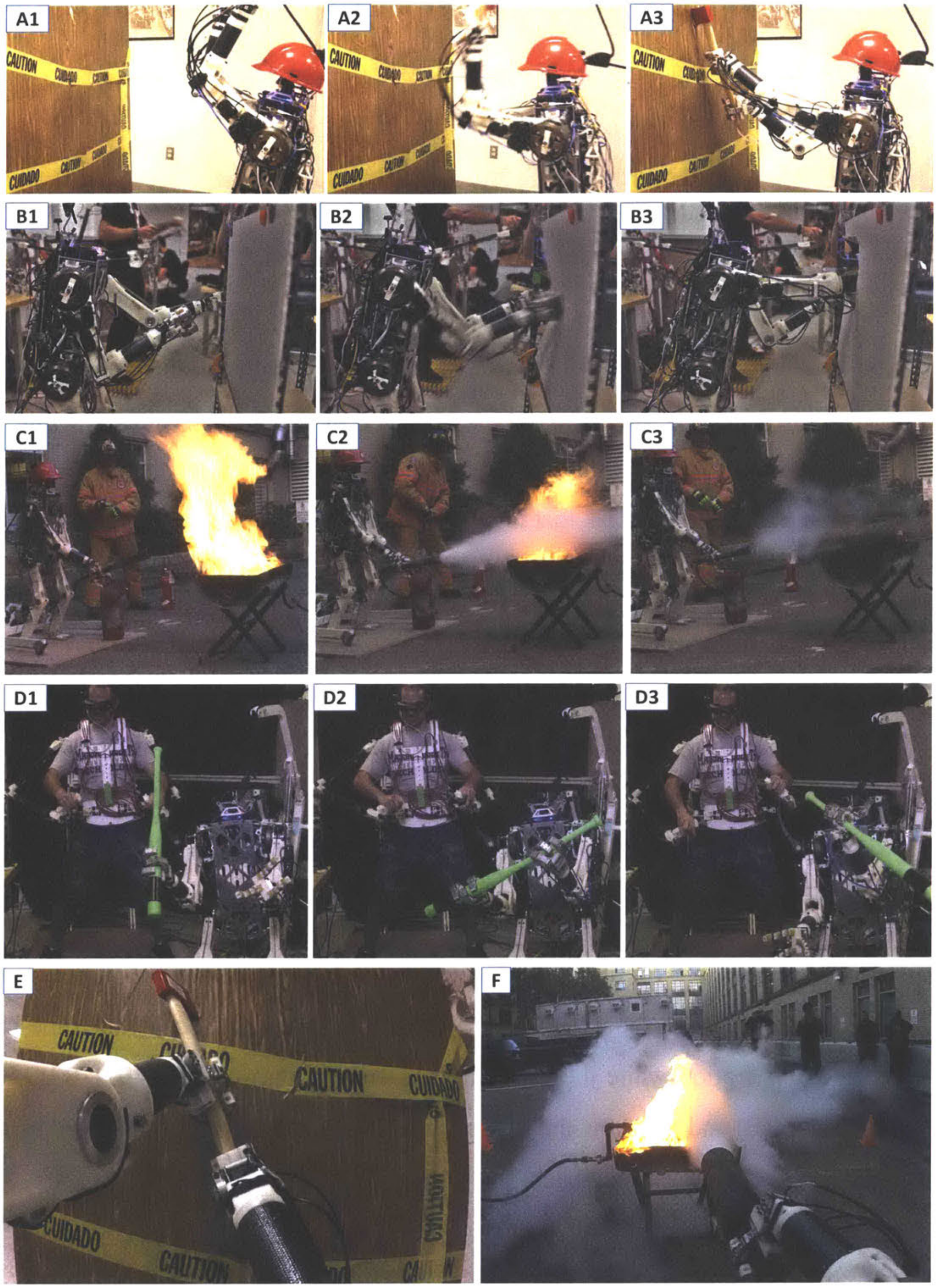

Figure 3-14: Teleoperated robot performing real-world tasks. (A1-A3) Time-lapse of axing experiment. (B1-B3) Time-lapse of punching experiment (C1-C3) Time-lapse of firefighting experiment (D1-D3) Time lapse of two-handed manipulation experiment (E) First-person view from the robot during the axing experiment (F) First-person view from the robot during the firefighting experiment.

disregards bipedal inherent underactuated and unstable dynamics. However, the HERMES robot was never able to walk. Stepping and walking are complex dynamic motions that involve a highly coordinated interplay between the Center of Mass state, the ground reaction forces and the feet placement simultaneously. In light of such complexity, we assume that a model-based teleoperation strategy is required to deal with the inherently unstable nature of human upright motion. Throughout the next Chapters, we attempt to identify the simplest model that is competent to capture the core dynamics that describe human motion strategy. This simple model will be utilized as the communication channel between the operator and the slave machine.

Additionally, for the strategies utilized in this Chapter, the human was completely responsible for both balancing the robot and conducting the required motor task. In addition to the requirement to self-balance, the burden of having full control over the robot's motor coordination results in a prohibitive increase of the human cognition load for more complex tasks. From the experience gained in the experiments from this Chapter, we anticipate that, in order to achieve extreme motor behaviors, the responsibility to stabilize the robot should be shared between the operator and the machine. For the remainder of this Thesis, we will attempt to identify the degree of autonomy that should be given to the Slave machine to complement human input.

To the author's knowledge, HERMES is the first humanoid robot to achieve extreme behaviors through whole-body bilateral teleoperation, contrasting the unilateral control commonly adopted in the literature. Moreover, instead of avoiding unexpected contact with the environment as is often done in robot control, HERMES is able to perform extreme behaviors that involve high impact forces. Despite the limitations of this system, a clear demonstration of the potential for bilateral teleoperation is presented.

Chapter 4

Model-Based Bilateral Teelopration

4.1 Introduction

Our first approach to tackle the problem of whole-body teleoperation, as presented in Chapter 3, neglected the natural dynamics of each system. In contrast, legged locomotion is mostly governed by dynamically stable trajectories (often quasi-passive) that cooperate with gravity to create sophisticated motions. In summary, the forces generated via contact with the ground, as well as reactive motions provided by the upper limbs, are utilized in parallel with strategic foot placement such that stable walking is achieved. Due to the complexity of such dynamics, the human can be utilized to provide the reference trajectory online while receiving physical feedback about the robot motion. To achieve this coupled behavior, first we analyze the equations of motion for the standing biped and briefly explain the mechanisms that are commonly used for balancing. From there, we expose the pendulum-like dynamics of the human Center of Mass and utilize a popular model for legged locomotion, the Linear Inverted Pendulum, to develop a coupling strategy between human and robot. This mapping is based on imposing dynamic similarity of both CoM states. Finally, after analyzing the linearized coupled dynamics, we show how the human is able to synchronously take steps with simulated robots with different scales, making evident the generality of the method. This generality is illustrated in Chapter 5 to control an underactuated system, the Cart-Pole, and later, in Chapter 7, to control Little HERMES, a small-scale bipedal robot.

4.2 Background on Balance Strategies

Legged locomotion is an extremely complex and nonlinear behavior that involves hybrid dynamics (continuous motions with discrete discontinuous events) and a large number of degrees of freedom. This underactuated dynamic system also possess severe input constraints that are defined by the properties of the intermittent contact with the environment (friction characteristics and inability to pull on the ground). In order to gain insights about this complex phenomena, researchers in Biomechanics and Robotics have recurred to simple models that are capable of capturing the core behavior under interest. More recently, [21] systematically derived the equations of motion for the standing human and exposed the contribution of each term, revealing fundamental strategies used for balancing on two legs. The motion of the human body can be described, without loss of generality, by the dynamics of the CoM. Additionally, an important point of the ground, the Center of Pressure [55], summarizes the net forces applied over the CoM and represents an important quantity for the indication of the robot control authority and stability.

Picture a human standing on two feet as represented by Figure 4-1-(A). Each leg can generate contact forces with the ground $\vec{F}^r_H$ and $\vec{F}^l_H$, which results in the motion of the human CoM. Utilizing Newton's Second Law, the planar linear equation can be written with the net forces F_{xH} and F_{zH} applied to the CoM

$$m_H \begin{bmatrix} \ddot{x}_H \\ \ddot{z}_H \end{bmatrix} = \vec{F}^r_H + \vec{F}^l_H = \vec{F}_{cH} = \begin{bmatrix} F_{xH} \\ F_{zH} \end{bmatrix}. \tag{4.1}$$

Moreover, assume the human can apply a net moment M_{yH} around the CoM using some sort of reaction torque such as waving the arms or rotating the torso, as depicted by Figure 4-1-(C) [21] [37]. We can now define a point on the ground, the Center of Pressure p_{xH}, where the net moment around the CoM equals zero:

$$F_{zH}\left(x_R - p_{xH}\right) - F_{xH} z_H + M_{yH} = 0,$$

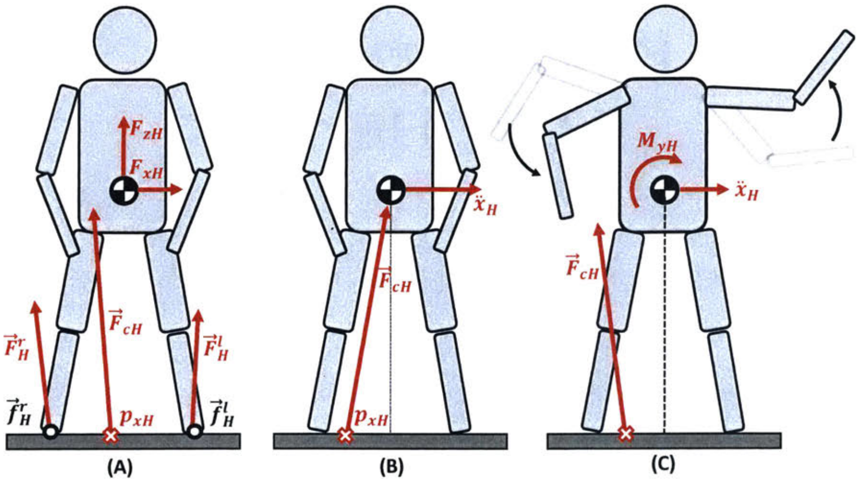

Figure 4-1: (A) The human apply contact forces on the ground that direct affect the body CoM. Mechanisms utilizing for balancing: (B) moving the CoP and (C) applying reaction moments around the CoM.

which can be rewritten as

$$p_{xH} = x_H - \frac{F_{xH}}{F_{zH}} z_H + \frac{M_{yH}}{F_{zH}}. \tag{4.2}$$

Utilizing the equation of motion for the horizontal acceleration, we finally get

$$p_{xH} = x_H - \frac{m_H \ddot{x}_H}{F_{zH}} z_H + \frac{M_{yH}}{F_{zH}}. \tag{4.3}$$

Equation (4.3) have three inputs that can manipulate the horizontal acceleration of the CoM. These inputs are the CoP position p_{xH}, the vertical force F_{zH} and the net moment around the CoM M_{yH}. The CoP can be placed by varying the relative vertical component of each foot contact force, or

$$p_{xR} = \frac{F^l_{zH} f^l_{xH} + F^r_{zH} f^r_{xH}}{F_{zH}}, \tag{4.4}$$

where f^l_{xH} and f^r_{xH} are the horizontal position of the left and right foot, respectively. Thus, by definition, because the human cannot pull on the ground, the CoP cannot exist anywhere outside the region between the feet (the Support Polygon):

$$p_{xH}^{min} = f_{xH}^{l} \leq p_{xH} \leq f_{xH}^{r} = p_{xH}^{max}. \tag{4.5}$$

The balancing mechanism that utilizes the CoP placement to regulate the CoM horizontal motion is known as "Ankle Strategy" [1]. Another way to regulate $\ddot{x}_H$ is to create a reaction moment M_{yH} around the CoM, known as the "Hip Strategy" [41]. Regulating the vertical component F_{zH} is a third possibility that has been recently explored to control robots [38]. However, it must be noticed that F_{zH} and M_{yH} are inputs that are also associated with the vertical position z_R and the roll orientation φ_{yH}. Hence, these inputs cannot be utilized to regulate balance indefinitely.

The most popular model utilized to describe and control walking is arguably the Linear Inverted Pendulum (LIP) [32][22]. The LIP model provides valuable insights about the legged locomotion unstable dynamics while being low dimensional and tractable. This model approximates the system as a point mass (the CoM) with a single point of contact with the floor (the CoP). Additionally, because there's no rotational inertia around the Center of Mass, all forces must be collinear with the line that connects the CoP and the CoM (such that $M_{yH} = 0$), see figure 4-2. The system also is constraint to maintain a constant nominal height, thus vertical acceleration is zero ($\ddot{z}_R = 0$), and the vertical component of the contact force must be equal to the gravitational force

$$F_{zR} = m_R g. \tag{4.6}$$

From figure 4-3 we can use the triangle similarity to obtain

$$\frac{F_{zR}}{F_{xR}} = \frac{h_R}{x_R - p_{xR}},$$

Where x_R is the horizontal position of the CoM of mass m_R at nominal height h_R, p_{xR} is the horizontal position of the CoP and F_{xR} corresponds to the horizontal component of the

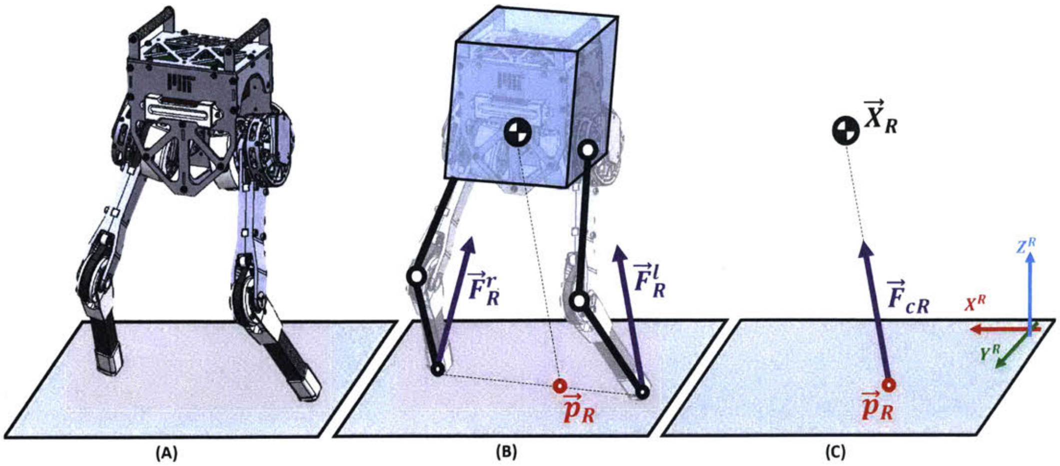

Figure 4-2: Model simplification for the Little HERMES robot. The robot in (A) is modeled as a single rigid body with massless legs in (B), which can be further simplified by a point mass, the Linear Inverted Pendulum, as shown in (C).

contact force $\overrightarrow{F}_c$. Utilizing Newton's law $F_{xR} = m_R\ddot{x}_R$, it can be reduced to

$$\frac{m_R g}{m_R \ddot{x}_R} = \frac{h_R}{x_R - p_{xR}}.$$

Thus, providing the equation of motion for the LIP

$$p_{xR} = x_R - \frac{g}{h_R}\ddot{x}_R,$$

or

$$p_{xR} = x_R - \frac{\ddot{x}_R}{\omega_R^2}, \tag{4.7}$$

where ω_R represents the linear natural frequency of the pendulum with nominal height h_R under gravitational field of magnitude g. Notice that the second order equation (4.7) tells us that the acceleration of the CoM is governed by its relative position with respect to the CoP. The unstable nature of the system is also clear from the opposing signs of the coefficients of x_R and $\ddot{x}_R$.

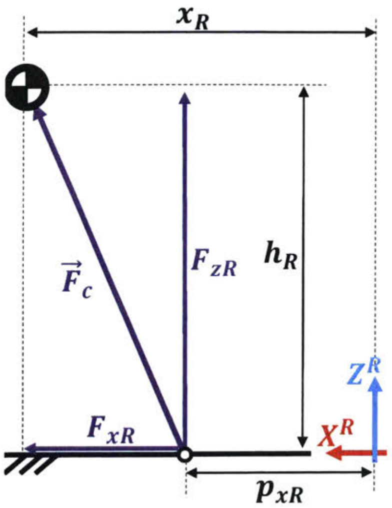

Figure 4-3: Linear Inverted Pendulum Model.

4.2.1 Stability of the LIP

The second order equation (4.7) can be written in State Space form with two variables

$$\dot{\vec{X}}_R = A\vec{X} + Bp_{xR}$$
$$\begin{bmatrix} \dot{x}_R \\ \ddot{x}_R \end{bmatrix} = \begin{bmatrix} 0 & 1 \\ \omega_R^2 & 0 \end{bmatrix} \begin{bmatrix} x_R \\ \dot{x}_R \end{bmatrix} + \begin{bmatrix} 0 \\ -\omega_R^2 \end{bmatrix} p_{xR}. \tag{4.8}$$

The state transition matrix A has eigenvalues $\pm\omega_R$. Thus, we can perform a change of variables and rewrite the system in canonical form, obtaining

$$\begin{bmatrix} \dot{\zeta}_{xR} \\ \dot{\xi}_{xR} \end{bmatrix} = \begin{bmatrix} -\omega_R & 0 \\ 0 & \omega_R \end{bmatrix} \begin{bmatrix} \zeta_{xR} \\ \xi_{xR} \end{bmatrix} + \begin{bmatrix} \omega_R \\ -\omega_R \end{bmatrix} p_{xR}. \tag{4.9}$$

Where the new states are defined by

$$\zeta_{xR} = x_R - \frac{\dot{x}_R}{\omega_R}, \tag{4.10}$$

$$\xi_{xR} = x_R + \frac{\dot{x}_R}{\omega_R}. \tag{4.11}$$

The state ζ_{xR} is associated with the stable eigenvalue $-\omega_R$ and is defined as the Convergent Component of Motion (CCM). The second state, ξ_{xR}, on the other hand, is associated with the unstable part of the dynamics and is defined as the Divergent Component of Motion (DCM) [70].

Previous work from Englsberger [15][14] show that controlling just the unstable portion of the dynamics, the DCM, is sufficient to make sure that the simple model is stable. In fact, assuming a constant DCM, we can utilize equation (4.11) to show that the CoM converges to the DCM with a first order behavior with time constant ω_R^{-1}, in other words,

$$\dot{x}_R = \omega_R\left(\xi_{xR} - x_R\right). \tag{4.12}$$

Additionally, if we assume constant ω_R, the time derivative of the DCM is given by

$$\dot{\xi}_{xR} = \dot{x}_R + \frac{\ddot{x}_R}{\omega_R}. \tag{4.13}$$

Utilizing equations (4.7) and (4.13) we can obtain the first order equation of motion of the DCM, given by

$$\dot{\xi}_{xR} = \omega_R\left(\xi_{xR} - p_{xR}\right). \tag{4.14}$$

Similarly to the equation of motion for the CoM, we see from (4.14) that the position of the CoP governs the time rate of change of the DCM. Moreover, assuming a constant CoP, the ξ_R moves *away* from p_{xR} with a first order behavior with time constant ω_R^{-1}, it is a naturally unstable state.

Other interpretations for the DCM

The definition for the composite state ξ_{xR} can also be obtained from other interpretations of the LIP dynamics. By solving equation (4.7) for $x_R(t)$, the work by Hof in [23] shows that, given initial conditions $x_R(0)$ and $\dot{x}_R(0)$, the minimum allowable (constant) position of the CoP to stop the CoM motion must be

$$p_{xR}^{min} = x_R(0) + \frac{\dot{x}_R(0)}{\omega_R}.$$

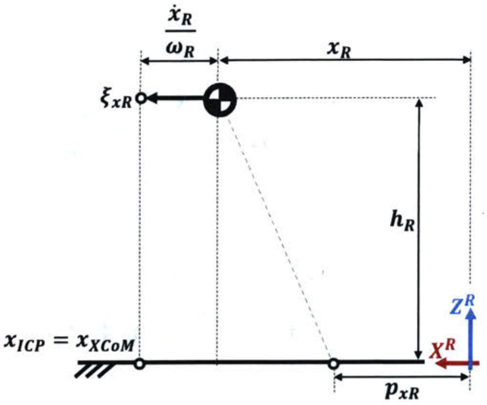

Figure 4-4: Linear Inverted Pendulum Model and the representation of the Divergent Component of Motion (DCM), the Instantaneous Capture Point (ICP) and the Extrapolated Center of Mass (XCoM).

The author defines this linear combination of the CoM as the Extrapolated Center of Mass (XCoM). Thus, in order to maintain the system stability, its necessary to guarantee that

$$p_{xR}^{min} \leq x_{XCoM}(t) \leq p_{xR}^{max} \tag{4.15}$$

for all time.

Similarly, authors at [58] define the LIP orbital energy. Given initial conditions $x_R(0)$ and $\dot{x}_R(0)$, the point foot of the robot must be instantaneously placed at a position

$$x_{ICP} = x_R(0) + \frac{\dot{x}_R(0)}{\omega_R},$$

such that the pendulum will naturally converge to the upright position when $x_R\left(t_{final}\right) = p_{xR}$. This point is defined as the Instantaneous Capture Point (ICP). The ICP is basically any x_R and $\dot{x}_R$ combination that lies perfectly on the Homoclinic Orbit of the pendulum.

The only subtle detail that differentiates the DCM from XCoM and the ICP is that the last two are ground projections of the linear combination of CoM states. On the other hand, the DCM is the point at height $z_R = h_R$ that is at a distance $\frac{\dot{x}_R}{\omega_R}$ from x_R. Figure 4-4 depicts the comparison between these three definitions.

4.3 Bilateral Feedback Based on the DCM

As described in Section 4.2, the DCM is closely related to the stability of the pendulum-like dynamics of legged locomotion. In fact, the relative position between this composite state ξ_{xR} and the system allowable Center of Pressure limits provides a sense of the control authority over the Center of Mass. Moreover, due to the unstable and underactuated nature of the Slave system, the state and force trajectories necessary to generate a walking motion must be dynamic. In this Section, we aim to generate this reference using a human operator and a bilateral feedback teleoperation strategy based on similarity.

It is intuitive to think that two shapes are geometrically similar if they can be made identical by scaling all dimensions by the same constant. The same way, two motions are defined as dynamically similar if they can be made identical by multiplying all lengths by some constant α_L, all times by a factor α_T and all forces by a ratio α_F. This principle is often used in biomechanics studies in order to compare the behavior of different animals across dramatically different physical scales [2][17].

In this Section we explore this idea in order to allow the slave robot to perform motions that are dynamically similar to the human motion in real-time through teleoperation. The caveat being that each system is governed by different characteristic time responses (natural frequencies). To mitigate this issue, we utilize bilateral force feedback to enforce the synchronization of master and slave.

4.3.1 Assumptions for Bilateral Teleoperation

The key idea of our approach is to transmit to the robot the human dynamic motion information instead of solely performing kinematic scaling as often is done in the literature. Additionally, we intend to provide a meaningful feedback to the operator such that s/he can freely re-plan this strategy online. Hence, to attain seamless dynamic synchronization between the two systems we adopt two key assumptions:

1. *Human motion can be closely described by a simple model.* The relative dynamics between the DCM and the contact forces (thus, the CoP) encompasses the main

method the operator utilizes for balancing and stepping [21]. Thus, this information is sufficient for the robot to reproduce these actions synchronously.

2. *Human adaptation to the coupled dynamics governs the overall performance.* Provided the appropriate interfacing mechanism, the operator will learn how to properly generate feasible motions for the complex dynamics of the coupled system. Through sufficient training, the feedback force allows the operator to adapt to new teleoperation conditions online.

4.3.2 Simple Models Utilized

Human Model

Figure 4-5 depicts the Frontal Plane variables and parameters used for the human operator in this study. These are: horizontal and vertical CoM positions x_H and z_H relative to the world-fixed coordinate frame for the human X^H and Z^H; torso roll orientation φ_H around the Y^H axis; right $\vec{f}^{\,r}_H = [f^r_{xH} \quad f^r_{zH}]^T$ and left $\vec{f}^{\,l}_H = [f^l_{xH} \quad f^l_{zH}]^T$ foot positions; Center of Pressure (CoP) position p_{xH}; net horizontal and vertical contact forces F_{xH} and F_{zH}; and net moment around CoM M_{yH}. The feedback force applied to the human by the BFI in the X^H direction is defined as F_{BFI}. This model is completely defined by the total mass m_H, moment of inertia I_H around the CoM, and nominal height h_H. In this work we consider I_H to be approximately constant. Notice we can relate the net ground reaction force shared by both feet $\vec{F}_H$ with the net forces and moment applied to the CoM by

$$\vec{F}_H = \begin{bmatrix} F_{xH} \\ F_{zH} \end{bmatrix},$$
$$M_{yH} = F_{zH}(x_R - p_{xH}) - F_{xH}(z_R - p_{zR}). \tag{4.16}$$

The horizontal and vertical components of the ground reaction forces (F_{xH} and F_{zH}) as well as the CoP p_{xH} can be directly measured by the force plate. The net moment M_{yH}, on the other hand, is estimated utilizing equation (4.16). The vertical component of the operator CoP p_{zH} is considered zero for all experiments in this Thesis.

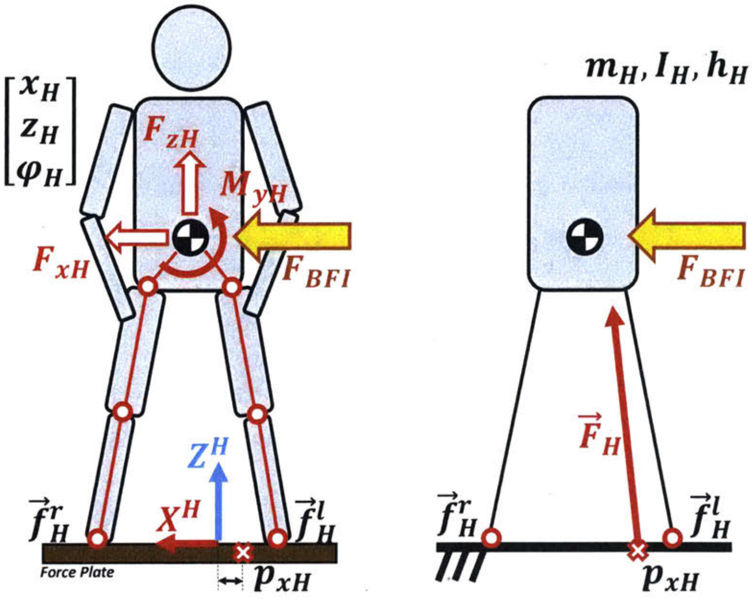

Figure 4-5: Model and simplifications utilized for human operator.

Robot Model

Similarly to previous work for legged robots [15][26], in this thesis a simplified model is assumed for the robotic platform. In this scenario the following assumptions are made:

1. The robot is a single rigid body with floating base.
2. Legs are massless force sources.
3. Feet have point contact with the ground.
4. No foot impact dynamics.
5. No communication delay between operator and robot.
6. Robot is constrained to move in the Frontal Plane.

Analogous to the human model, the robot model is completely defined by three parameters: (i) the total mass m_R; (ii) the moment of inertia I_R around the CoM; and (iii) the nominal height above the ground h_R. As shown in Figure 4-6, the robot frontal plane model has three DoFs: horizontal x_R and vertical z_R position of the CoM in respect to the world-fixed frame X^R and Z^R for the robot; and body roll orientation φ_R around the Y^R axis. The right

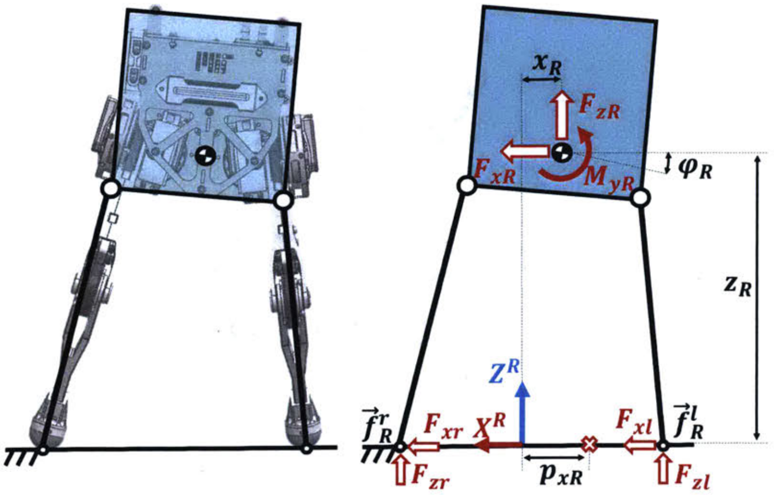

Figure 4-6: Frontal Plane model utilized for bipedal robot. This model is completely defined by the mass, moment of inertia around the CoM and nominal height.

foot at position $\vec{f}^r_R$ can apply a tangential force F_{xr} and normal force F_{zr} when in contact with the ground; analogously, the left foot can do the same at point $\vec{f}^l_R$ with F_{xl} and F_{zl}. The point p_{xR} represents the horizontal component of the distance between the Center of Pressure of the robot measured and the coordinate frame X^R and Z^R.

4.3.3 Similarity-Based Mapping and Feedback Law

In Section 4.2.1 we analyze how the DCM is closely related to the stability of the model for legged locomotion. Now, we aim to achieve the geometric similarity of the DCM between both systems, the operator and the robot:

$$\frac{\xi_{xR}}{h_R} = \frac{\xi_{xH}}{h_H}. \tag{4.17}$$

Following the same rational, the time evolution of these two states can be made dynamically similar and also consistent with their own natural frequency if we impose the dimensionless equality

$$\frac{\dot{\xi}_{xR}}{h_R\omega_R} = \frac{\dot{\xi}_{xH}}{h_H\omega_H}. \tag{4.18}$$

Notice that, from the DCM equation of motion (4.14), we see that if the equality (4.18) holds, than it is also true that

$$\frac{\xi_{xR} - p_{xR}}{h_R} = \frac{\xi_{xH} - p_{xH}}{h_H}. \tag{4.19}$$

Suggesting that dynamic similarity is preserved if the relative distance between the CoP and the DCM is also preserved (if there is no net moment around the human or robot CoM). If we replace equation (4.13) in (4.18) we obtain

$$\frac{\xi_{xH}}{h_H} - \frac{x_H}{h_H} + \frac{\ddot{x}_H}{h_H \omega_H^2} = \frac{\xi_{xR}}{h_R} - \frac{x_R}{h_R} + \frac{\ddot{x}_R}{h_R \omega_R^2}. \tag{4.20}$$

This result will be utilized later on.

Horizontal Force Scaling

The Frontal Plane horizontal CoM dynamics of robot and human can be written by analyzing figures 4-5 and 4-6:

$$m_R \ddot{x}_R = F_x^{ff} + F_x^{fb}, \tag{4.21}$$

$$m_H \ddot{x}_H = F_{xH} + F_{BFI}. \tag{4.22}$$

In (4.21) the robot controller is composed of feedfoward F_x^{ff} and feedback F_x^{fb} terms, these together represent the net forces applied to the CoM (if there is no external disturbance applied to the robot, $F_{ext} = 0$). The robot feedback force is given by the linear law

$$F_x^{fb} = K_x \left(\frac{\xi_{xH}}{h_H} - \frac{\xi_{xR}}{h_R} \right), \tag{4.23}$$

with error compensation gain K_x. Moreover, as defined before, the term F_{xH} in equation (4.22) represents the net horizontal force that the operator applies on his/her own CoM by interacting with the ground, and F_{BFI} is the horizontal force applied by the Balance Feedback Interface.

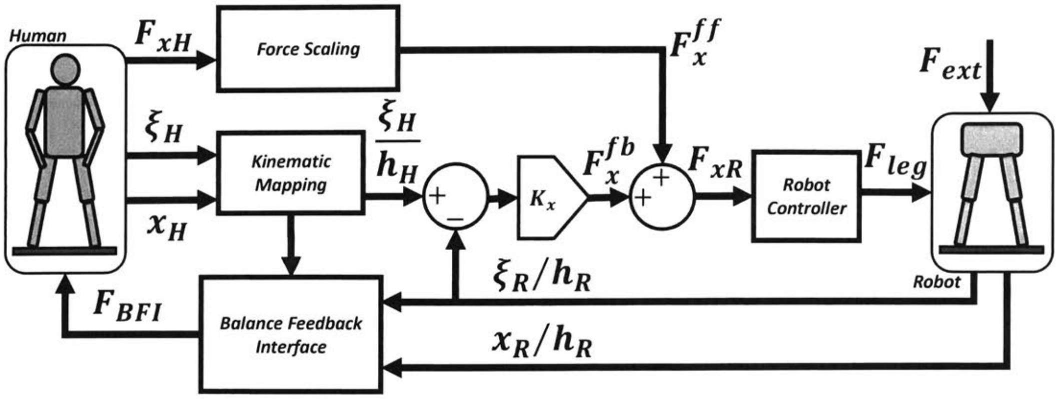

Figure 4-7: Block diagram for the control-loop for the horizontal dynamics.

Now, equation (4.20) can be expanded using equations (4.21) and (4.22):

$$\frac{\xi_{xH}}{h_H} - \frac{x_H}{h_H} + \frac{F_{xH} + F_{BFI}}{m_H h_H \omega_H^2} = \frac{\xi_{xR}}{h_R} - \frac{x_R}{h_R} + \frac{F_x^{ff} + F_x^{fb}}{m_R h_R \omega_R^2}. \tag{4.24}$$

Considering zero DCM tracking error ($F_x^{fb} = 0$), to satisfy equation (4.24), we define the feedfoward term that represents the dimensionless scaling of the human horizontal force component

$$F_x^{ff} = \frac{m_R h_R \omega_R^2}{m_H h_H \omega_H^2} F_{xH}, \tag{4.25}$$

and the feedback law that takes care of the residual difference such that we can achieve the equality (4.18). Thus

$$F_{BFI} = m_H h_H \omega_H^2 \left(\frac{\xi_{xR} - x_R}{h_R} - \frac{\xi_{xH} - x_H}{h_H} \right), \tag{4.26}$$

which can also be written as

$$F_{BFI} = m_H h_H \omega_H^2 \left(\frac{\dot{x}_R}{h_R \omega_R} - \frac{\dot{x}_H}{h_H \omega_H} \right). \tag{4.27}$$

Equations (4.25), (4.26) and the expression for F_x^{fb} now define all terms from (4.21) and (4.22). The system input for the horizontal closed-loop dynamics is the human force F_{xH}. Figure 4-7 depicts the teleoperation control loop for horizontal dynamics.

Vertical Force Scaling

From the general CoP equation (4.3), the time-varying natural frequency of each model is given by the expression $\omega_i^2 = \frac{F_{zi}}{m_i z_i}$ [21], with $i = R, H$. We can simply preserve the vertical dynamic similarity of the system by writing the equality

$$\frac{F_{zR}}{m_R z_R \omega_R^2} = \frac{F_{zH}}{m_H z_H \omega_H^2},$$

or

$$F_z^{ff} = \frac{m_R z_R \omega_R^2}{m_H z_H \omega_H^2} F_{zH}. \tag{4.28}$$

Similarly to equation (4.25), equation (4.28) gives us the feedfoward term of the vertical force generated by the robot controller. Notice that, for a constant height, the vertical force scaling is simply

$$F_z^{ff} = \frac{m_R h_R \omega_R^2}{m_H h_H \omega_H^2} F_{zH}.$$

CoP Geometric Similarity

An important characteristic of the approach utilized here is that the force scaling and feedback laws, defined previously, lead to the synchronization of the Center of Pressure of robot and human. In fact, to achieve simultaneous change of stance and stepping, the robot should reproduce human CoP trajectory such that each foot can be lifted off simultaneously. Evaluating the dimensionless CoP error δ_p we write

$$\delta_p = \frac{p_{xH}}{h_H} - \frac{p_{xR}}{h_R}. \tag{4.29}$$

Considering negligible (for now) moments M_{yi} around the CoM, the CoP equation is given by [55]

$$p_{xi} = x_i - \frac{m_i \ddot{x}_i}{F_{zi}} z_i, \tag{4.30}$$

for the human ($i = H$) and robot ($i = R$). Plugging in the equations of motion (4.21) and (4.22) in equation (4.30), we obtain the error

$$\delta_p = \frac{x_H}{h_H} - \frac{F_{BFI} + F_{xH}}{h_H F_{zH}} z_H - \frac{x_R}{h_R} + \frac{F_x^{ff} + F_x^{fb}}{m_R F_{zR}} z_R.$$

This can be reduced using the feedfoward F_x^{ff} (4.25), feedback F_x^{fb} (4.23) and BFI force F_{BFI} (4.27) expressions to

$$\delta_p = \left(1 + \frac{K_x}{m_H h_H \omega_H^2}\right)\left(\frac{\xi_{xH}}{h_H} - \frac{\xi_{xR}}{h_R}\right). \tag{4.31}$$

Equation (4.31) indicates that if there is no tracking error the robot will reproduce the scaled human CoP trajectory ($\frac{p_{xH}}{h_H} = \frac{p_{xR}}{h_R}$). This result was expected from equality (4.19). Additionally, the deviation between robot and human CoP is also proportional to the gain K_x, discussed next.

Robot Controller Feedback Gain K_x

By analyzing equation (4.31), we note that the feedback gain K_x represents the correction magnitude of the robot balancing controller as the DCM tracking error becomes larger. Although it is intuitive that this gain should be large enough such that the tracking error is small, very large values will cause the robot CoP dynamics to considerably deviate from human reference. Additionally, lower robot feedback gain K_x improves the system stability in the presence of human-to-robot communication delay during bilateral teleoperation. In this work, we intend to exploit human balancing strategies and choose K_x to be relatively small such that the feedfoward term F_x^{ff} dominates the robot horizontal dynamics. Motivated by human motion characteristics here we define this gain such that the feedback bandwidth is equivalent to the robot linearized inverted pendulum dynamics. Thus, $\sqrt{\frac{K_x}{h_R m_R}} = \omega_R$, or

$$K_x = m_R h_R \omega_R^2. \tag{4.32}$$

Notice that the feedback error in F_x^{fb} is dimensionless, thus K_x has force units. And because of the proportionality of ξ_i, with the CoM velocity $\dot{x}_i$ this feedback law also provides damping to the controller.

Balance Feedback Interface Force Dynamics

With equations (4.25) and (4.26) and the feedback gain from (4.32) we can rewrite the equations of motion of the horizontal coupled dynamics in Space State form

$$\dot{q}(t) = Aq(t) + Bu(t). \tag{4.33}$$

Here we define the state vector

$$q = \begin{bmatrix} x_R & \xi_{xR} & x_H & \xi_{xH} \end{bmatrix}^T,$$

and input

$$u = F_{xH}.$$

The state transition matrix is given by

$$A = \begin{bmatrix} -\omega_R & \omega_R & 0 & 0 \\ -\omega_R & \omega_R - \frac{K_x}{m_R h_R \omega_R} & 0 & \frac{K_x}{m_R h_H \omega_R} \\ 0 & 0 & -\omega_H & \omega_H \\ -\frac{h_H \omega_H}{h_R} & \frac{h_H \omega_H}{h_R} & 0 & 0 \end{bmatrix}, \tag{4.34}$$

and the input mapping matrix

$$B = \begin{bmatrix} 0 \\ \frac{h_R \omega_R}{m_H h_H \omega_H^2} \\ 0 \\ \frac{1}{m_H \omega_H} \end{bmatrix}. \tag{4.35}$$

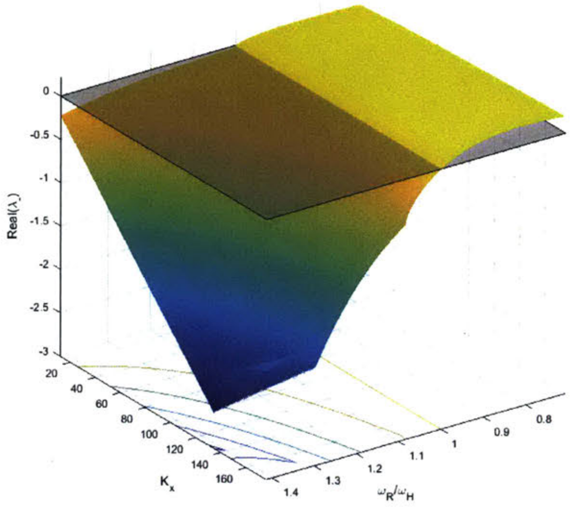

Figure 4-8: Real part of the fourth eigenvalue λ_- of state transition matrix A. Notice that the system is open-loop unstable (positive real component) for $\omega_R < \omega_H$ independently of K_x. The plane splits the space between positive and negative Z coordinates.

The eigenvalues of the state transition matrix in (4.34) for K_x given by (4.32) are

$$\lambda_1 = 0, \quad \lambda_2 = -\omega_H,$$
$$\lambda_{3,4} = \lambda_{+,-} = \frac{-\omega_R \pm \sqrt{\omega_R(4\omega_H - 3\omega_R)}}{2}, \tag{4.36}$$

which have positive real part eigenvalues for $\omega_H > \omega_R$ (robot has a slower natural frequency than the human). This unstable eigenvalue indicates that the operator must actively stabilize the robot with a larger scale ($h_R > h_H$). A different gain K_x will lead to a different transition matrix A and different eigenvalues. However, as shown on Figure 4-8, the system is always open-loop unstable for any $\omega_R < \omega_H$ independently of the choice of K_x.

Taking the Laplace Transform of the State Space equation and solving for the state vector, we obtain

$$Q(s) = (A - sI)^{-1} BU(s), \tag{4.37}$$

from which we can extract the influence of the force F_{xH} on each CoM response in Laplace domain

$$\frac{X_H(s)}{F_{xH}(s)} = \frac{1}{m_H}\frac{(s+\omega_R)^2}{sD(s)}, \tag{4.38}$$

$$\frac{X_R(s)}{F_{xH}(s)} = \frac{h_R\omega_R^2}{m_H h_H \omega_H^2}\frac{(s+\omega_H)^2}{sD(s)}. \tag{4.39}$$

with

$$D(s) = (s+\omega_H)\left(s^2 + s\omega_R + \omega_R^2 - \omega_R\omega_H\right). \tag{4.40}$$

Notice that if $\omega_R = \omega_H$ equations (4.38) and (4.39) reduce to

$$\frac{X_H(s)}{F_{xH}(s)} = \frac{1}{m_H s^2},$$

$$\frac{X_R(s)}{F_{xH}(s)} = \frac{h_R}{h_H}\frac{1}{m_H s^2},$$

which completely decouples both systems ($F_{BFI} = 0$). For this condition, the operator moves as if controlling his/her own body as the robot simply follows a linearly scaled CoM trajectory. Ideally, under no external disturbances, $F_{BFI} = 0$.

The input that controls the coupled system is the human contact force F_{xH}. Thus, from the state space matrix equation (4.37) we can solve for each state and write the force produced by the BFI from (4.26):

$$\frac{F_{BFI}(s)}{F_{xH}(s)} = (\omega_R - \omega_H)\frac{s^2 - \omega_H\omega_R}{D(s)}. \tag{4.41}$$

Interestingly, the feedback force sign and gain in (4.41) is directly proportional to the difference in the natural frequencies of the human and the robot, $\omega_R - \omega_H$. But the feedback force never goes unbounded if this difference increases. In fact we can show that

$$\lim_{\frac{\omega_R}{\omega_H}\to\infty}\frac{F_{BFI}}{F_{xH}}(s) = \lim_{\frac{\omega_R}{\omega_H}\to 0}\frac{F_{BFI}}{F_{xH}}(s) = -\frac{\omega_H}{(s+\omega_H)}.$$

Considering External Disturbances

Assume that the robot experiences an external force F_{ext} applied horizontally to its CoM, we can rewrite equation (4.21) as

$$m_R \ddot{x}_R = F_x^{ff} + F_x^{fb} + F_{ext}. \tag{4.42}$$

Now, we expand the input vector to

$$u = \begin{bmatrix} F_{xH} & F_{ext} \end{bmatrix}^T,$$

and the input matrix to

$$B = \begin{bmatrix} 0 & 0 \\ \frac{h_R \omega_R}{m_H h_H \omega_H^2} & \frac{1}{m_R \omega_R} \\ 0 & 0 \\ \frac{1}{m_H \omega_H} & 0 \end{bmatrix}. \tag{4.43}$$

And we can show that

$$\frac{F_{BFI}(s)}{F_{ext}(s)} = \frac{m_H h_H \omega_H^2}{m_R h_R \omega_R^2} \frac{s^2}{D(s)}. \tag{4.44}$$

Thus, the external force F_{ext} applied to the robot is filtered before the transmission to the operator. Indeed, the transmitted feedback force is mitigated according to the robot's capacity to deal with the disturbance, if ω_R is large enough, the force influence is substantially reduced. This is evident by

$$\lim_{\frac{\omega_R}{\omega_H} \to \infty} \frac{F_{BFI}}{F_{ext}}(s) = 0.$$

Unexpected forces applied to the robot are transmitted to the operator through the BFI according to equation (4.44). This input is normalized according to robot parameters (m_R, h_R, and ω_R), and scaled back up to human proportions. Notice that, with this strategy, only transient dynamics are transmitted, steady state disturbances produce zero feedback:

$$\lim_{s\to 0}\frac{F_{BFI}}{F_{ext}}(s)=0.$$

Yet, if this disturbance force can be either estimated or measured by the robot, we can extend the feedback equation (4.27) to

$$F_{BFI}=m_H h_H \omega_H^2\left(\frac{\dot{x}_R}{h_R\omega_R}-\frac{\dot{x}_H}{h_H\omega_H}\right)+\frac{m_H h_H \omega_H^2}{m_R h_R \omega_R^2}\hat{F}_{ext}. \tag{4.45}$$

Preserving the required dynamic similarity between both systems. This is the inverse force scaling that is utilized for the robot feedfoward term F_x^{ff} in equation (4.25).

Considering Non-zero Moments around the CoM

During the majority of the time, humans regulate the Angular Momentum around the CoM closely to zero. But these moments can be non-negligible during teleoperation for certain balancing strategies [21]. In addition, the robot may be required to produce non-zero moments around its CoM. For this scenario we extend the CoP equation (4.30) to include the moment component M_{yi} around the CoM [55]

$$p_{xi}=x_i-\frac{m_i\ddot{x}_i}{F_{zi}}z_i+\frac{M_{yi}}{F_{zi}}, \tag{4.46}$$

for $i=R,H$.

To preserve the synchronous support matching result from equation (4.31), the moment that the robot generates must have the same dimensionless contribution to the CoP equation as human input. Thus,

$$\frac{M_{yH}}{z_H F_{zH}}=\frac{M_{yR}}{z_R F_{zR}},$$

or, plugging in equation (4.28),

$$\frac{M_{yH}}{m_H z_H^2 \omega_H^2}=\frac{M_{yR}}{m_R z_R^2 \omega_R^2}.$$

This relation provides the feedfoward law for the moment the robot should apply to its own CoM using the contact forces or other mechanisms (such as a Reaction Mass):

$$M_y^{ff} = \frac{m_R z_R^2 \omega_R^2}{m_H z_H^2 \omega_H^2} M_{yH}. \tag{4.47}$$

Writing down the angular equations of motion of the model in Figure 4-6 we have

$$I_R \ddot{\varphi}_R = M_y^{ff} + M_y^{fb}, \tag{4.48}$$

$$I_H \ddot{\varphi}_H = M_{yH}. \tag{4.49}$$

Thus, for perfect roll tracking ($M_y^{fb} = 0$), we can use the feedfoward equation (4.47) and write the angular acceleration equality

$$\ddot{\varphi}_R = \frac{I_H}{I_R} \frac{m_R z_R^2 \omega_R^2}{m_H z_H^2 \omega_H^2} \ddot{\varphi}_H. \tag{4.50}$$

Taking the integral with respect to non-dimensional time ($t\omega_R$ and $t\omega_H$), we have

$$\dot{\varphi}_R = \frac{I_H}{I_R} \frac{m_R z_R^2 \omega_R}{m_H z_H^2 \omega_H} \dot{\varphi}_H, \tag{4.51}$$

and, from second integral,

$$\varphi_R = \frac{I_H}{I_R} \frac{m_R z_R^2}{m_H z_H^2} \varphi_H. \tag{4.52}$$

Equations (4.51) and (4.52) provide the proper angular coordinate transformation between both systems. Notice the similarity of these equations to the dimensional analysis of [58] and [43].

Final Remarks for the Teleoperation Law

The presented methodology enforces dynamic similarity between human and machine with simultaneous support change. Nevertheless, there are a few details that should be kept in mind when applying the teleoperation mapping strategy presented here:

1. There will always exist a force F_{BFI} applied to the human during motion if $\omega_R \neq \omega_H$, even for perfect DCM tracking.
2. The sign and gain of the feedback force in equation (4.41) depends on the relative natural frequency difference between robot and operator.
3. The BFI force transmits external forces F_{ext} filtered by robot dynamics (equation (4.44)).
4. We assume that the human motion strategy is embedded in the relative dynamics between the Divergent Component of Motion ξ_{xH} and the contact force F_{xH}.
5. The systems is open-loop unstable for $\omega_H > \omega_R$ (independent of K_x, see Figure 4-8).
6. If $\omega_H = \omega_R$, both systems have decoupled dynamics under no external disturbances.

A geometric interpretation of our method is provided in Figure 4-9 utilizing the point mass Linear Inverted Pendulum (LIP) model [58]. Assume the human behaves as LIP, meaning that the net force $\frac{F_{xH}^{net}}{m_H g}$ with dimensionless components $\frac{F_{xH}+F_{BFI}}{m_H g}$ and $\frac{F_{zH}}{m_H g}$ is collinear with the line that connects $\frac{x_H}{h_H}$ and $\frac{p_{xH}}{h_H}$, and there is no net moment around the CoM ($M_{yH} = M_{yR} = 0$). From the pendulum natural frequency $\omega_i = \sqrt{\frac{g}{h_i}}$, the force scaling proposed in this work leads to $\frac{F_{xR}}{m_R g} = \frac{F_{xH}}{m_H g}$ and $\frac{F_{zR}}{m_R g} = \frac{F_{zH}}{m_H g} = 1$. Similarly, for perfect DCM tracking, we have $\frac{\xi_R}{h_R} = \frac{\xi_H}{h_H}$ and $\frac{p_{xR}}{h_R} = \frac{p_{xH}}{h_H}$. Also, if $\omega_R \neq \omega_H$, robot and human CoM do not match ($\frac{x_R}{h_R} \neq \frac{x_H}{h_H}$). For this scenario, the feedback force applied to the operator $\frac{F_{BFI}}{m_H g}$ complements the ground reaction force $\frac{F_{xH}}{m_H g}$ such that the net forces applied to the human and robot CoM present the same dimensionless direction (collinear with the line that connects the dimensionless CoM $\frac{x_i}{h_i}$ and the dimensionless CoP $\frac{p_{xi}}{h_i}$).

4.3.4 Leg Force Controller

So far we depicted the procedure to define the net forces and moments the robot must apply on its own CoM (F_{xR}, F_{zR}, and M_{yR}) in order to follow the reference human motion. In this section, we show how to use these net forces and the knowledge of the contact points in order to generate the proper force distribution to each leg. The robot maintains

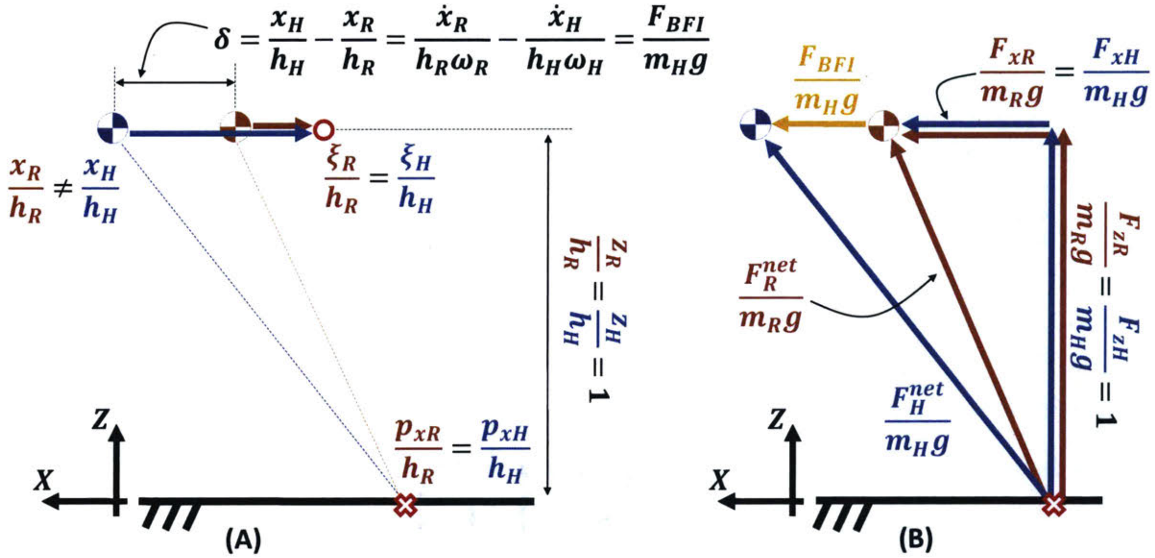

Figure 4-9: Dimensionless geometric interpretation of our approach. Figure (A) presents the dimensionless kinematics of both systems. Figure (B), on the other hand, shows the dimensionless force information for the same instant as figure (A). The human variables are depicted in blue while robot variables are depicted in brown. Both CoP's are represented by the red "X" on the ground and both DCM's as the red circle. Assume perfect DCM tracking ($\frac{\xi_{xR}}{h_R} = \frac{\xi_{xH}}{h_H}$) and that the human behaves as a LIP. The net human ground reaction force with normalized components $\frac{F_{xH}+F_{BFI}}{m_H g}$ and $\frac{F_{zH}}{m_H g}$ is collinear with the line that connects $\frac{x_H}{h_H}$ and $\frac{p_{xH}}{h_H}$. The dimensionless force produced by the Human-Machine Interface $\frac{F_{BFI}}{m_H g}$ guarantees that the resulting force applied to the robot CoM $\frac{F_{xR}}{m_R g}$ has the same normalized direction as the human net ground reaction force: it lies collinear to the line that connects $\frac{x_R}{h_R}$ and $\frac{p_{xR}}{h_R}$.

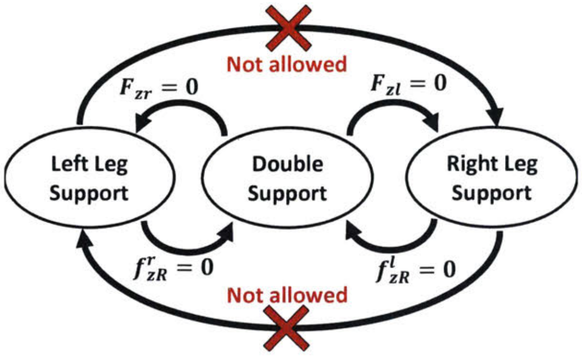

Figure 4-10: Leg force controller State Machine. If one of the required vertical forces are less or equal to zero the state transits from double to single support. The contact is only allowed to apply forces against the ground again when the z component of the foot position f^i_{zR} is equal to zero. The model does not allow transition from right to left leg single contact or vice-versa, but the double support transition is allowed to be infinitely fast.

balance by controlling the interaction forces between its feet and the ground, similarly to the strategy used in [49]. The net forces and moment applied to the robot CoM are given by the feedfoward and feedback terms

$$\begin{bmatrix} F_{xR} \\ F_{zR} \\ M_{yR} \end{bmatrix} = \begin{bmatrix} F_x^{ff} \\ F_z^{ff} \\ M_y^{ff} \end{bmatrix} + \begin{bmatrix} K_x \left(\frac{\xi_{xH}}{h_H} - \frac{\xi_{xR}}{h_R} \right) \\ K_z \left(\frac{\xi_{zH}}{h_H} - \frac{\xi_{zR}}{h_R} \right) \\ K_\varphi \left(\frac{\xi_{\varphi H} I_H}{m_H h_H^2} - \frac{\xi_{\varphi R} I_R}{m_R h_R^2} \right) \end{bmatrix}, \tag{4.53}$$

with $\xi_{zi} = z_i + \frac{\dot{z}_i}{\omega_i}$ and $\xi_{\varphi i} = \varphi_i + \frac{\dot{\varphi}_i}{\omega_i}$, $i = R, H$.

Furthermore, the robot balance and posture controller is divided in two conditions: *double support* and *single support*. The first controller is active when desired forces to be applied to the robot CoM do not require negative vertical forces, meaning that both contact points are preserved. The second controller is used when one contact is lost and the robot can no longer maintain both feet on the ground. This controller usually regulates leg forces under very large lateral disturbances or extreme state configurations, such as when taking a step. Figure 4-10 depicts the conditions for stance change. As will be shown, the actual robot may achieve aerial phases, when both feet loose contact with the ground. However, for the simulations in this Chapter, this condition is prohibited.

Double Support

In the vicinity of the nominal posture the leg contact forces are generated using equation (4.53) to calculate the desired net forces and moment to be applied to the CoM. Disregarding the contact constraints the system is overactuated: there are four available contact forces to be regulated to produce two net forces and one net moment around the CoM. Thus we can formulate the linear system given by

$$
\begin{aligned}
F_{xr} &= F_{xR}\frac{F_{zr}}{F_{zR}}, \qquad (4.54)\\
F_{xl} &= F_{xR}\frac{F_{zl}}{F_{zR}}, \qquad (4.55)\\
F_{zr} + F_{zl} &= F_{zR}, \qquad (4.56)\\
F_{zr}(x_R - f^r_{xR}) + F_{zl}(x_R - f^l_{xR}) - F_{xr}(z_R - f^r_{zR}) - F_{xl}(z_R - f^l_{zR}) &= M_{yR}. \qquad (4.57)
\end{aligned}
$$

Notice that equations (4.54) and (4.55) together contain the equation $F_{xr} + F_{xl} = F_{xR}$ and also state that the contact point with larger vertical force will also generate a larger portion of the desired horizontal contact force. This second condition is imposed in order to reduce the chance of violating friction constraints.

Solving the linear system from equations (4.54) to (4.57) provide the contact forces F_{xr}, F_{xl}, F_{zr}, and F_{zl} to be applied to the ground in order to produce the desired motion. Because of the massless legs assumption, these forces are mapped to joint torques τ using the contact Jacobian, $\tau = J_c^T F_{leg}$. Here we assume each leg has three actuated DoFs: hip ad/abduction and hip/knee flexion/extension. If the solution of the linear system yields a negative vertical force for either leg it means that the robot lost one of the contact points and now stands in single support. Thus, only two contact forces are available to generate the net desired forces: a condition of *single support*.

For more complex systems, a very common strategy to solve the problem of force distribution is to develop an optimization-based controller (often Quadratic Programming) that takes into account the contact constraints and other limitations of the system, such approach is becoming increasingly popular in the literature [52][79][39]. As an extension of the present work, one could measure independent human leg contact forces and use this information as near-optimal seed for the controller. An estimation of human joint torque could improve even further the optimization process.

Single Support

The single support condition means the robot only has two contact forces allowed with the ground. Thus, we are required to define a force distribution gain γ that balances the effort to generate the required horizontal force and also to minimizes roll moment. Thus, for instance, during left leg support, we assign

$$F_{zl} = F_{zR}, \tag{4.58}$$

$$F_{xl} = \gamma F_{ZM} + (1-\gamma) F_{xR}, \tag{4.59}$$

$$0 \leq \gamma \leq 1.$$

where F_{ZM} is the horizontal force necessary to create the desired moment M_{yR} around the CoM:

$$F_{ZM} = \frac{F_{zl}(x_R - f^l_{xR}) - M_{yR}}{(z_R - f^l_{zR})}.$$

During the simulations in this Chapter we utilize $\gamma = 1$. For experiments with the actual robot, this value was reduced to $\gamma = 0.8$. This gain represents a trade-off between controlling the horizontal state or the roll angle. We found that this value can be experimentally tuned according to the ratio between the robot mass and moment of inertia.

Swing Leg Controller

During single support, the robot is allowed to utilize the swing leg to track the operator's relative foot position. However, from the point feet assumption, the system is unstable if it stands for long periods of time in single support.

The robot legs are massless for the simulations developed in this Chapter, thus the robot feet have no defined dynamics. To model the robot's ability to track the foot reference, we define that the swing foot is able to follow the operator's foot with a first order behavior with time constant ω_s^{-1}. For instance, the left foot position during swing starting at time t_{s0} is given by

$$\vec{f}^{\,l}_{R}(t) = \vec{f}^{\,l}_{R}(t_{s0}) + \frac{h_R}{h_H}\left(1 - e^{\omega_s(t-t_{s0})}\right)\vec{f}^{\,l}_{H}(t). \tag{4.60}$$

For experiments with the actual robot, when the physical robot limb actually has finite inertia, a different swing foot controller will be defined later in Chapter 7.

4.3.5 Control Summary

In this Section we provide a brief summary of the method explained this far and highlight the most relevant equations. The overall procedure for a single control iteration occurs as follows:

1. Given the measured human CoM state, Center of Pressure p_{xH} and ground reaction forces F_{xH} and F_{zH}, we utilize equations (4.11) and (4.46) to estimate the human DCM ξ_{xH} and moment M_{yH}.
2. Next, we use equations (4.25), (4.28) and (4.47) to calculate the feedfoward terms for the robot controller F_x^{ff}, F_z^{ff} and M_y^{ff}.
3. In parallel, the feedback term is calculated using equations (4.23) and (4.32) in addition to the estimated human and robot states.
4. With the feedfoward and feedback terms, the robot controllers define the desired efforts F_{xR}, F_{zR} and M_{yR} to be applied by the legs according to (4.53).
5. Equations (4.54) to (4.57) are now utilized to define the force to be applied by each point foot.
6. The feet forces are adjusted according to the contact constraints: unilateral vertical force ($F_{zi} \geq 0$) and horizontal friction boundaries ($|F_{xi}| \leq \mu F_{zi}$), for $i = r, l$.
7. A state machine defines the double or single support conditions and modify the stance leg force accordingly using (4.58) and (4.59).

8. If in single support, the swing leg state is updated utilizing (4.60).
9. Finally, the feedback force F_{BFI} to be applied to the operator is calculated using equation (4.27).

4.3.6 Simulation Results

To validate the proposed strategy for teleoperation developed in this work we analyze the system performance while the human operator interacts with a simulated robot through the BFI under different conditions. First, we evaluate the coupled dynamic behavior regarding the robot scale and natural frequency. Next, we inspect how external forces F_{ext} applied to the robot are transmitted to the human through the BFI. And finally, we show how the proposed method from this work allows the operator to take steps synchronously with the simulated machine. In all experiments, a trained operator is asked to stand in the BFI and perform the given tasks. The force plate is calibrated under nominal static conditions. For all experiments we define the gravity constant as $g = 9.81 m/s^2$ and the friction coefficient $\mu = 0.6$ for the robot ground-feet interaction (assumed rubber foot on hard tile floor). The real-time robot simulator updates the robot states with an integrator with fixed time-step of $1 ms$.

Feedback Dependence on Robot Size

Given the human operator nominal mass ($m_H = 90kg$), moment of inertia around CoM ($I_H = 10.5kgm^2$) and nominal height ($h_H = 1m$), we analyze the teleoperation behavior for three different scale machines: small ($h_R = h_H/2$), medium ($h_R = h_H$), and large ($h_R = 2h_H$), see Figure 4-11. Human moment of inertia I_H was experimentally estimated by fitting the model to the data from movements with large moments around the CoM, similar to [21]. Following cubic scaling for volume, the small robot is about eight times lighter than the human ($m_R = m_H/8 \approx 12kg$), the medium robot has the same mass as the operator ($m_R = m_H$), and the large robot is about eight times heavier ($m_R = 8m_H = 720kg$). The moment of inertia for each experiment is proportionally scaled such that $I_R = I_H \frac{m_R h_R^2 \omega_R^2}{m_H h_H^2 \omega_H^2}$ [43].

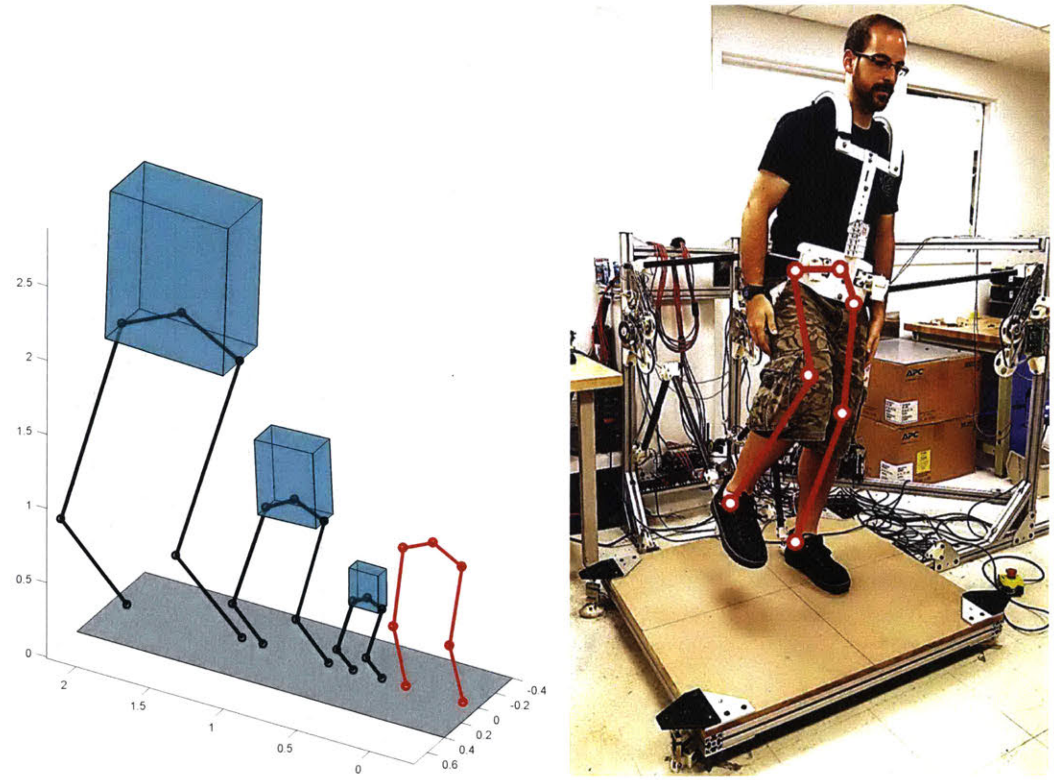

Figure 4-11: Different robot scales utilized in the experiments. In red is depicted the human lower body tracking model. We analyze the behavior for three different scale machines: small ($h_R = h_H/2 = 0.5m$), medium ($h_R = h_H = 1m$), and large ($h_R = 2h_H = 2m$). Masses are scaled to the length ratio cubed $m_R = m_H \left(\frac{h_R}{h_H}\right)^3$.

The force produced by the BFI given by equation (4.26) enforces that both systems are bounded to have similar DCM normalized time rate of change in length (h_i) and time ($t\omega_i$). Notice that the sign and magnitude of F_{BFI} depends on the relative difference in human and robot natural frequencies: $\omega_R = \omega_H$ should produce $F_{BFI} = 0$ under no external disturbances, and $\omega_R > \omega_H$ produces a feedback force in phase with F_{xH}, while $\omega_R < \omega_H$ yields F_{BFI} that is out of phase with F_{xH}. Figure 4-12 depicts these results. Intuitively, when the robot has faster dynamics than the operator ($\omega_R > \omega_H$), the BFI speeds up the movements of the human through positive feedback. The opposite is verified for the larger machines ($\omega_R < \omega_H$).

In Figure 4-13 we confirm that, as expected, $\frac{x_R}{h_R} \neq \frac{x_H}{h_H}$ when $\omega_R \neq \omega_H$; instead the proposed feedback law enforces that $\frac{\xi_R}{h_R} = \frac{\xi_H}{h_H}$. Notice that the motion frequency also varies according to height, for low ω_R the feedback force produces damping that tends to slow down the lateral motion, typical of larger scale legged systems. Analogously, smaller robots have faster characteristic time responses, in this scenario F_{BFI} leads to speed up human motion.

Feedback Dependence on External Disturbances

Unexpected forces applied to the robot are transmitted to the operator through the BFI according to equation (4.44). This input is normalized according to robot parameters (m_R, h_R, and ω_R), and scaled back up to human proportions. Figure 4-14 displays the force feedback F_{BFI} given external forces F_{ext} applied to the virtual robot by physically loading a force sensor. Notice that, with this strategy, only transient dynamics are transmitted, steady state disturbances produce zero feedback: $\lim_{s \to 0} \frac{F_{BFI}}{F_{ext}}(s) = 0$. The figure also shows the corrective feedback force F_x^{fb} that the robot autonomously applies.

Change of Stance and Stepping

A core advantage of our approach is that it allows natural change of stance and stepping. It is worth mentioning that the robot controller does not impose a CoP trajectory, instead it defines a feedfoward force scaling that leads to Center of Pressure matching. By moving one's own body under coupled dynamics, the operator induces a CoP condition on the robot

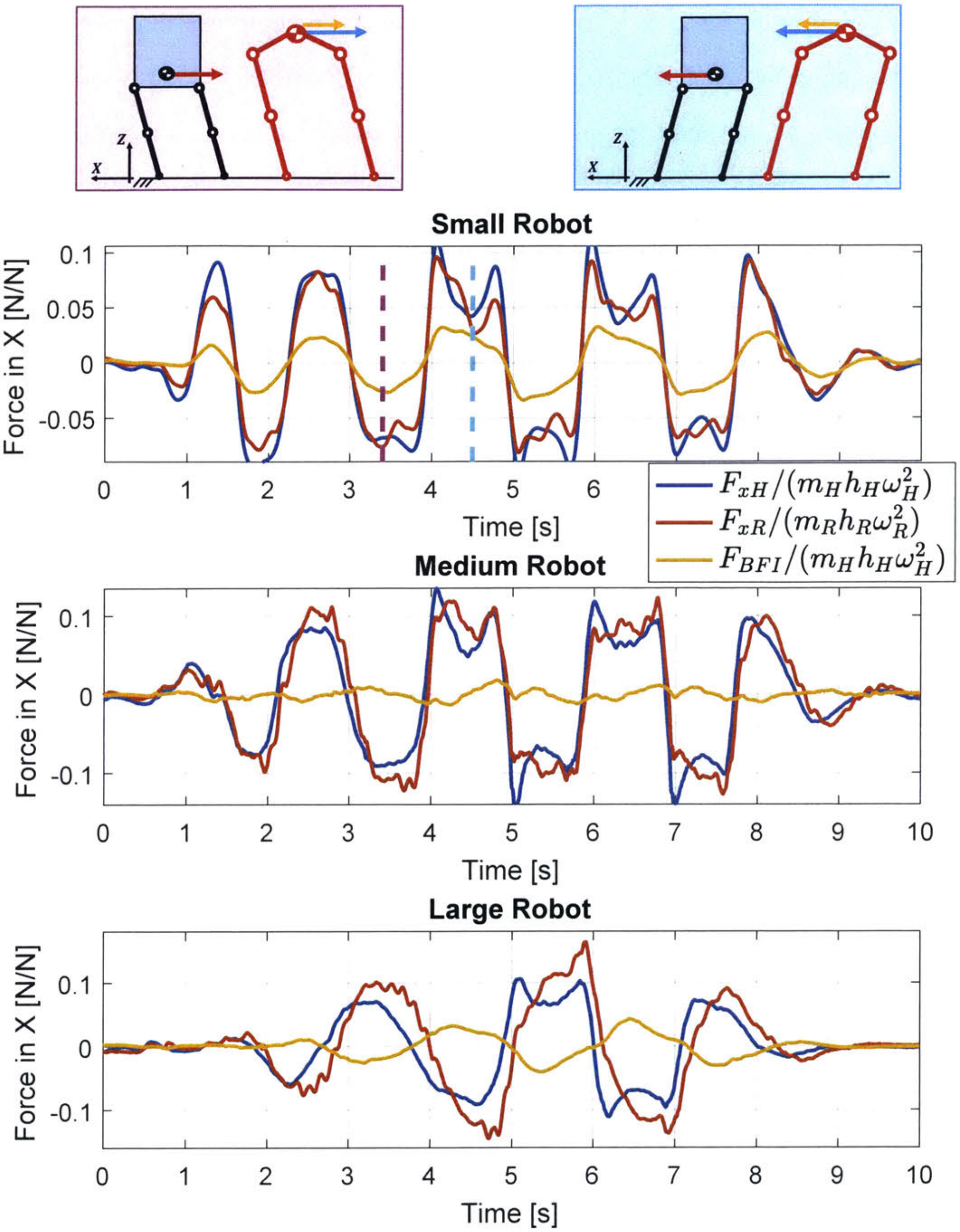

Figure 4-12: Horizontal forces applied to each system CoM for different robot scales. All forces are normalized by the mass of the system they act upon. Top plot: Small robot with $m_R = 12kg$, $h_R = h_H/2 = 0.5m$, and $\omega_R > \omega_H$. Here the BFI force is in phase with the human horizontal contact force. The cartoon shows snapshots for this scenario at $\approx 3.4s$ (left - magenta line) and $\approx 4.5s$ (right - cyan line). The arrows represent the horizontal forces with the same color code as the plots. Middle plot: Medium robot with equal human scale $m_R = 90kg$, $h_R = h_H = 1m$, and $\omega_R = \omega_H$. Ideally, we should have $F_{BFI} = 0$ under no external disturbances. Bottom plot: Large robot with $m_R = 720kg$, $h_R = 2h_H = 2m$, and $\omega_R < \omega_H$. The feedback force F_{BFI} is out of phase with F_{xH}. In this scenario the coupled system is open loop unstable.

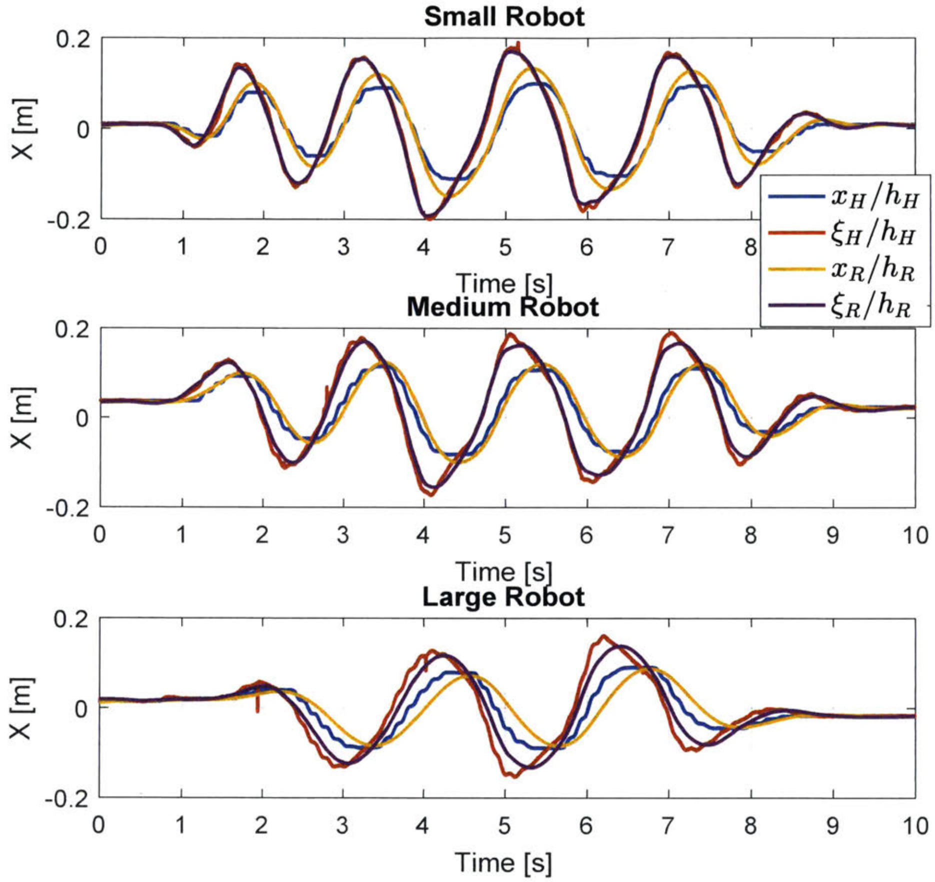

Figure 4-13: Tracking performance for different robot scales. As expected, for appropriate Extrapolated Center of Mass (XCoM) tracking, the Center of Mass (CoM) of human and robot do not match unless $\omega_R = \omega_H$. Interestingly, for equal XCoM, the small robot CoM in the upper plot precedes human CoM while the opposite is verified for the large scale robot on the bottom plot. Also, due to the force feedback the comfortable motion frequency varies according to the size, it is intuitive to think that larger systems have slower stepping frequency. The cartoon in Figure 4-12 shows snapshots for the small robot scenario at $\approx 3.5s$ (left) and $\approx 4.5s$ (right).

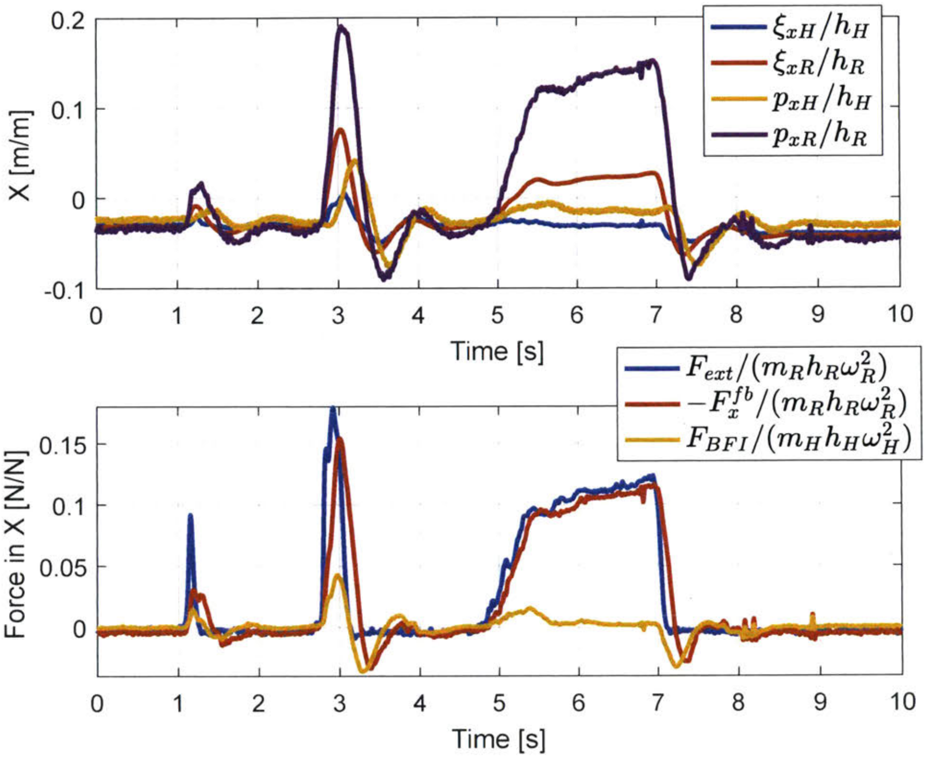

Figure 4-14: Time evolution of horizontal dynamics during external disturbance F_{ext} applied to the robot. Notice how, in this scenario, robot and human CoP do not match while $F_{ext} \neq 0$. In fact, the difference between both values is proportional to the robot corrective action given by the gain K_x according to (4.31). The bottom graph depicts the dynamics of external force F_{ext} applied to the robot transmitted to the operator through the BFI. All values are normalized according to the parameters of the system they act upon. The Interface high-pass filters these forces such that steady state disturbances provide no force feedback (see equation (4.44)). The negative of the robot feedback force F_x^{fb} is displayed so it can be compared to the external disturbance.

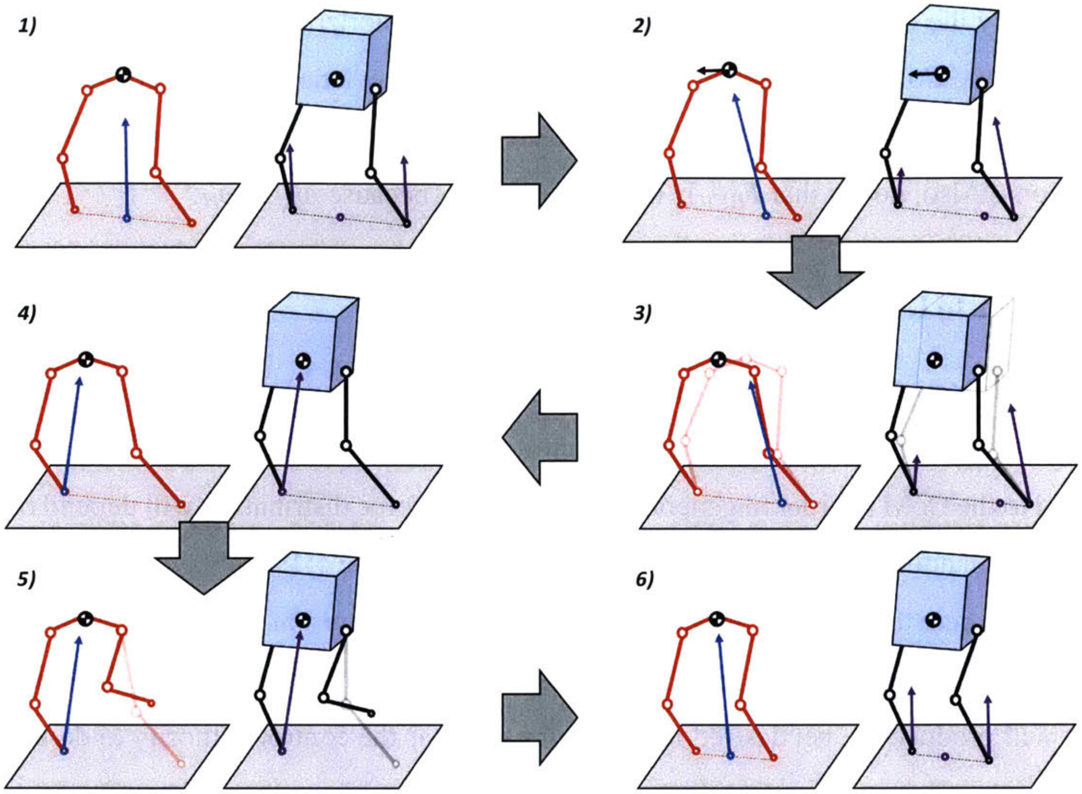

Figure 4-15: Stepping sequence during teleoperation, the human is depicted as the red linkages while the robot is represented by the blued cube with black legs. (1) Human and robot stand in place with the CoP mid-way between the two contact points. (2) The human shifts its CoP to the left and the robot reproduces this action due to the force mapping. (3) The shear component of the ground reaction force shifts the human and robot CoM to the right. (4) At a certain moment, both systems drive their respective CoP to the right foot. The robot senses that it lost support on the left foot. (5) The zero contact force on the left foot allows the robot to track the operator's swing leg trajectory. (6) The robot places its foot at a distance geometrically similar to the operator's left foot.

such that one foot can be lifted off in order to take a step. Figure 4-15 breaks down the dynamics during stepping.

Figure 4-16 depicts the tracking performance of a half human-scale robot ($h_R = 0.5m$) taking side steps while tracking the operator DCM. As expected, the CoM of both systems do not match, on the other hand, the robot is able to take synchronous steps with the human due to the CoP geometric similarity. In fact, notice that the robot CoM *precedes* human CoM trajectory. Figure 4-17 shows the time evolution of the X component of relevant points, including the position of the left and right feet for each system. Areas in red represent left leg single support while regions in green show right leg single support, as depicted by the cartoon. Finally, Figure 4-18 shows the horizontal and vertical net forces applied to the CoM by the operator and the robot. Small deviations from normalized F_{xR} to F_{xH} are assumed to be due to small corrections by the feedback term F_x^{fb} and small height variations. Also, notice that F_{BFI} is in phase with F_{xH} because $\omega_R > \omega_H$.

Robustness to Uneven Terrain

A characteristic of the controller presented in this work is that it is robust to uneven terrain and multiple contacts. The operator transmits to the robot the reference net forces to be applied to the CoM in order to generate motion, but the force distribution will depend on the robot control authority defined locally in the machine. Figure 4-19 displays a teleoperation condition where the robot steps onto an obstacle that is not present for the operator. Notice in Sub-figure 4-19-4 how the ground contacts are different from the human reference. The robot will produce the net desired force as long as it has the control authority to do so.

4.4 Discussion

4.4.1 Why not track CoM?

It is very intuitive to think that the teleoperation mapping should attempt to make the robot reproduce the human CoM motion. But such control law is more restrictive than the strategy proposed here. It requires that both systems match the CoM position as well as their first and second time rates of change simultaneously. Given the unstable and underactuated nature of the LIP, tracking CoM may generate infeasible trajectories for systems with considerably different natural frequencies. In addition, for this teleoperation strategy to be extended to legged robots, the slave machine must be able to reproduce the master CoP trajectory such that both systems can take simultaneous steps. Assume, for example, that $\frac{x_R}{h_R} = \frac{x_H}{h_H}$ for all time, then it is also true that $\frac{\dot{x}_R}{h_R} = \frac{\dot{x}_H}{h_H}$ and $\frac{\ddot{x}_R}{h_R} = \frac{\ddot{x}_H}{h_H}$ for all time. From equation (4.7), we can see that the dimensionless CoP difference in this case is

$$\delta_{px} = \frac{p_{xR}}{h_R} - \frac{p_{xH}}{h_H} = \frac{\ddot{x}_H}{h_H}\left(\frac{1}{\omega_R^2} - \frac{1}{\omega_H^2}\right).$$

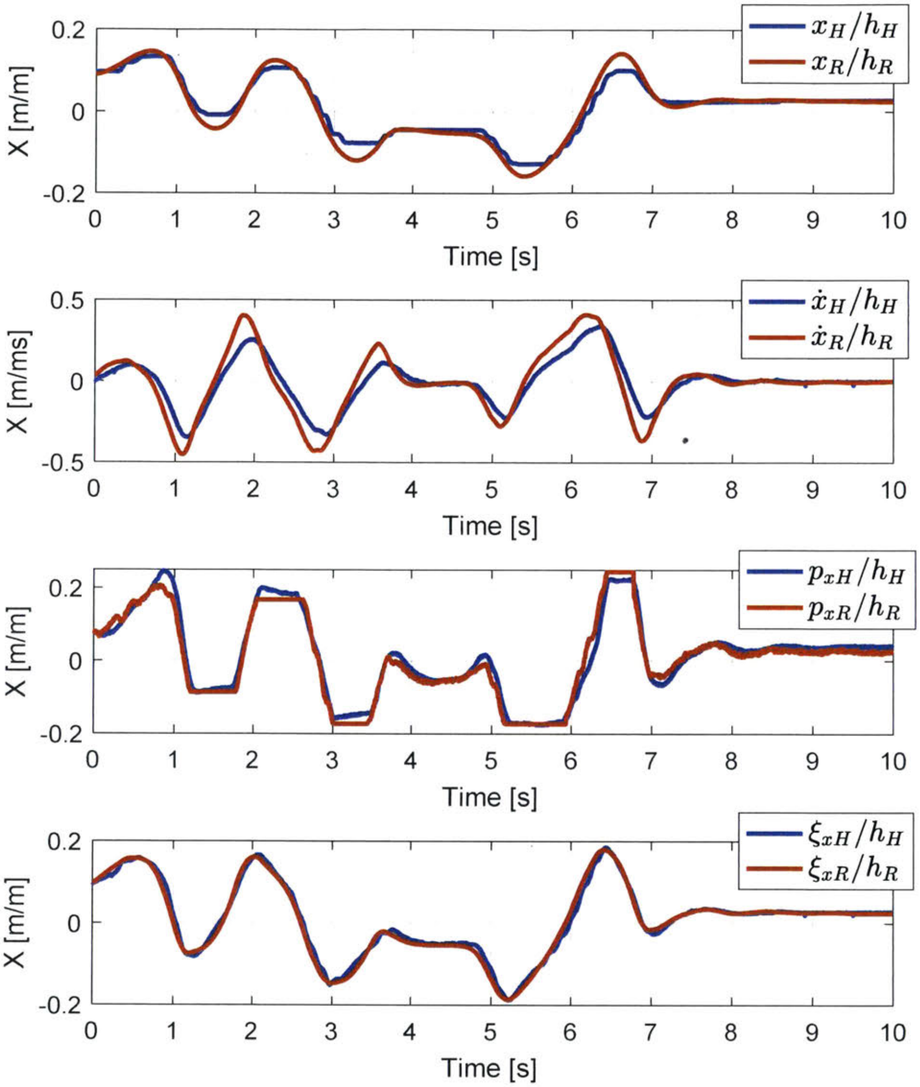

Figure 4-16: Horizontal evolution of human and small scale robot states during dynamic teleoperation of side stepping. Values are normalized according to each system nominal height h_R and h_H. Notice that for perfect XCoM tracking $\frac{\xi_R}{h_R} = \frac{\xi_H}{h_H}$ the robot normalized Center of Pressure p_{xR} reproduces human CoP p_{xH} trajectory (see equation (4.31)). Also, because $\omega_R > \omega_H$ the robot CoM in the top plot precedes human CoM. When $\dot{x}_R = 0$, the human CoM velocity $\dot{x}_H$ has a positive value, thus the robot CoM presents a larger amplitude such that both XCoM's can match.

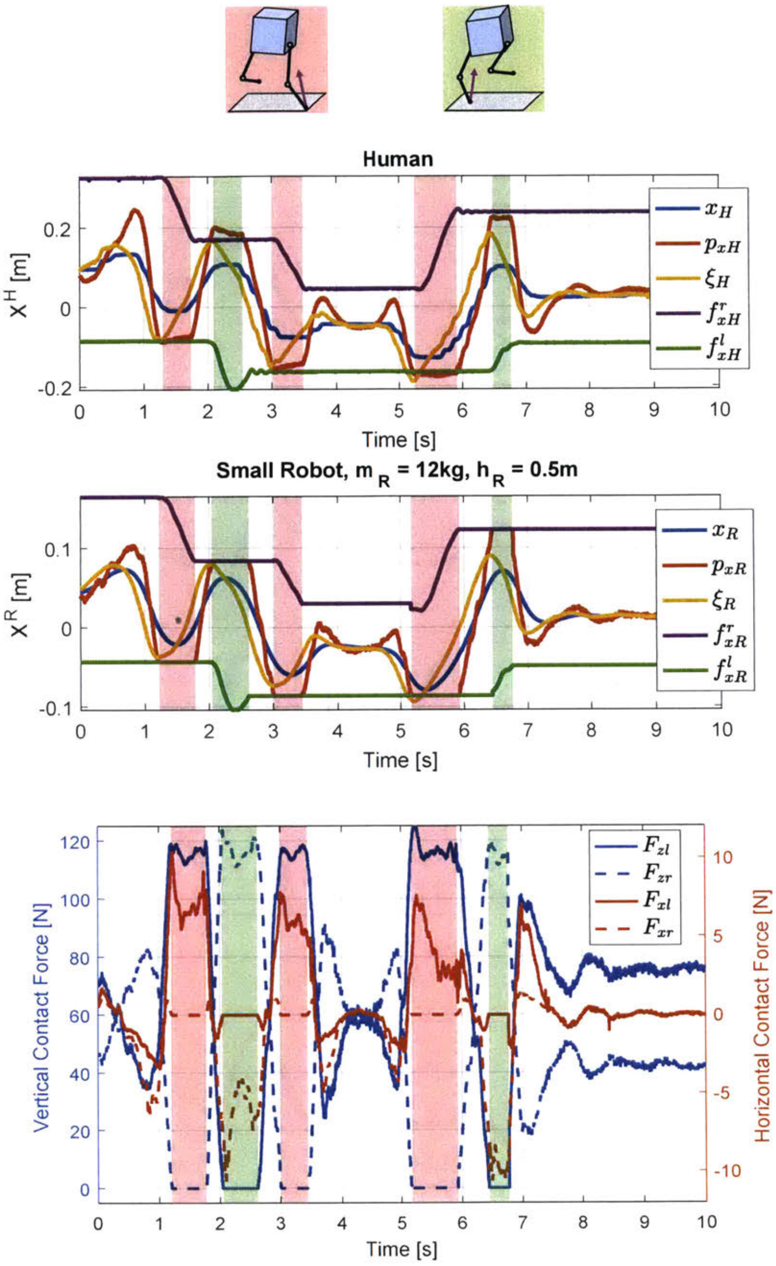

Figure 4-17: Detailed depiction of horizontal component of human (top) and small scale robot (bottom) relevant variables during dynamic teleoperation of side stepping. Center of Mass x_i, Center of Pressure p_{xi}, Extrapolated Center of Mass ξxi, and right and left foot positions f^r_{xi} and f^l_{xi} (with $i = R, H$) are shown. Values are normalized according to each system nominal height h_R and h_H. Regions in red represent left leg stance while regions in green account for right leg stance, as indicated by the cartoon. The robot is capable of following human stepping reference by synchronously shifting the support foot from left to right and then back. During single stance the human CoP varies slightly (due to small ankle torque and/or errors on the CoP estimation) while the robot CoP remains constant (point feet model). The bottom plot displays the ground reaction forces for the left (solid lines, F_{xl}, F_{zl}) and right (dashed lines, F_{xr}, F_{zr}) feet, notice that the forces reduce to zero during swing phase of the foot.

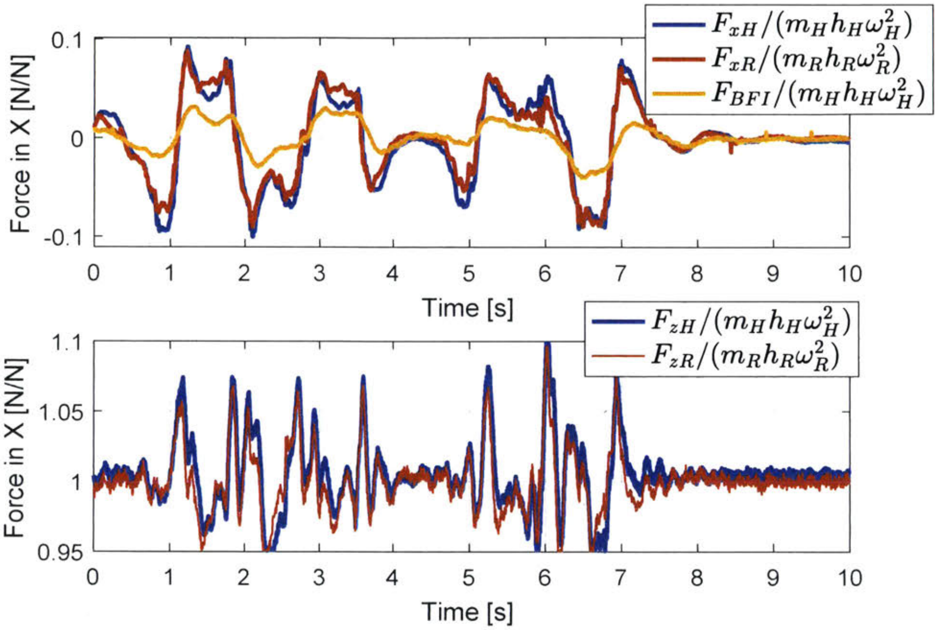

Figure 4-18: Vertical and horizontal contact forces applied to human and robot CoM during dynamic teleoperation of side stepping. All values are normalized according to the parameters of the system they act upon. Top: horizontal components of the net contact (F_{xR} and F_{xH}) and BFI (F_{BFI}) forces. We believe that the small deviations from F_{xR} and F_{xH} are due to variations on CoM height and horizontal XCoM tracking error correction. Bottom: Vertical components of the net contact forces F_{zR} and F_{zH}. Notice the large deviation from the baseline gravitational force $\frac{m_i g}{m_i h_i \omega_i^2} = 1$.

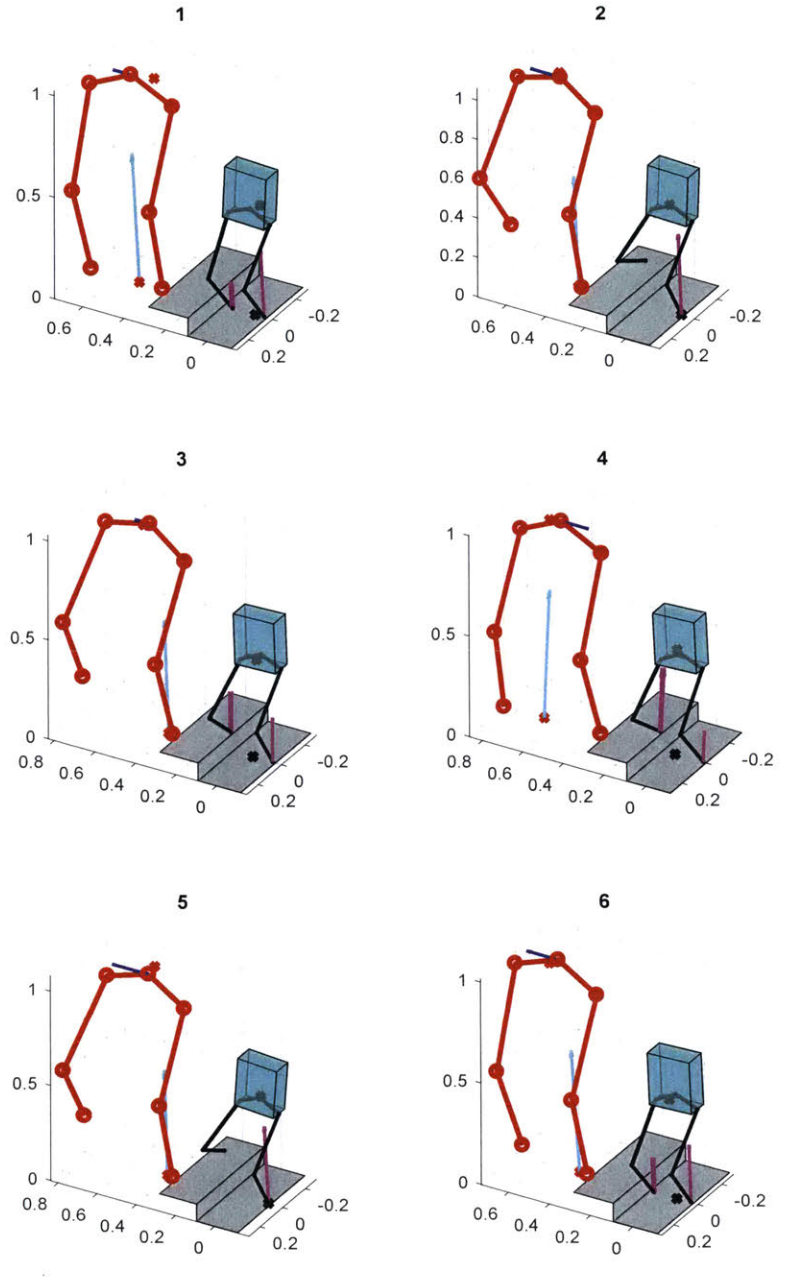

Figure 4-19: Snapshots of human (in red) and robot (bold black) during dynamic teleoperation of side up-stepping. Robot contact forces for each leg are shown in magenta in order to depict support conditions; the human net force is also displayed (in cyan). Our approach is robust to ground variations between operator and machine: in this example the robot steps onto an obstacle that is not present for the human operator. Notice in Sub-figure 4 the contact points for human and robot are different due to the presence of ground irregularity. The feedback force F_{BFI} applied to the operator's CoM is shown in dark blue.

Which means that the CoP error is proportional to the relative scale difference and the motion acceleration. Suggesting that highly dynamic motions may violate the stability condition in (4.15) if master and slave have substantially different scales, even if the human motion is stable. Simply tracking a scaled CoM reference is an insufficient condition for dynamic stability for the LIP.

The work in [23] shows that it is sufficient to stabilize just the unstable component of the dynamics (the DCM), and the CoM will track this composite state while constrained by its own natural frequency. It is straightforward to see that, for a constant ξ_{xR},

$$\dot{x}_R = \omega_R \left(\xi_{xR} - x_R \right),$$

which means that the CoM exponentially converges to the DCM.

4.4.2 Limitations to the Approach

In this Chapter we describe the evaluation of the strategy with robots that range from half to two times human size. As shown by the State Space analysis in this Chapter, there is no limit to the difference between human and robot scale for this particular model, however, for real applications, there is a limit to how fast or slow the human can move and, thus, synchronize with the machine. Additionally, different characteristics of the system may dictate the dynamic behavior across different scales. Pushing this discrepancy to the limit, if the robot lies in the microscopic scale, friction and atomic forces are likely to be non-negligible. In contrast, too large robots may be difficult to control due to the extremely low natural frequency, making hard for the operator to plan dynamic motions. It stays as an open problem to establish the boundaries of the difference between human and robot scales.

Moreover, we make simplifying assumptions that are required to be addressed for the implementation of this teleoperation scheme in a real system. These are:

1. No impact dynamics when the robot foot comes in contact with the ground. We address this limitation by designing legs with high Impact Mitigation Factor (IMF) [80], as described in Chapter 6.

2. Robot legs are massless. In Chapter 6 we show how we place the actuators proximal to the body and reduce leg reflected inertia, approximating this assumption.
3. The controller requires the ability to regulate the ground reaction forces. Chapter 6 describes the design of a Proprioceptive actuation scheme that achieves high bandwidth force control via commanded motor current and leg kinematics [63].
4. The dynamics on the Frontal and Sagittal Planes can be decoupled and are analogous. The controller of a real 3D robot will need to simultaneously stabilize both planes, which in actuality have coupled dynamics.
5. No communication delay between operator and robot. It is unclear how much lag the strategy proposed here can tolerate but we anticipate that state observers can help mitigate this issue.
6. The simple model does not take into account the limited joint travel and torque saturation of real robots. This is usually addressed by an optimization controller that properly distributes the torques across all joints [79].

Other common issues on legged robot control such as accurate state estimation, sensor noise and drift, contact instability and force bandwidth are anticipated to be relevant for real applications.

Chapter 5

Dynamic Bilateral Teleoperation of the Cart-Pole

5.1 Introduction

This Chapter presents the experimental evaluation of the bilateral feedback law for the teleoperation of an underactuated dynamic system: the Cart-Pole. This physical system illustrates in many levels another simple model, the Linear Inverted Pendulum (LIP); a popular template for legged robot control and, in this Chapter, the mapping channel between the operator and robot. We develop a scaling strategy based on geometric and kinematic similarity in order to generate dynamically feasible trajectories for the LIP with a natural frequency different than the human's. Moreover, by modifying the classic equations for the Cart-Pole, we show how it can competently represent the proposed template quantitatively and visually. Experiments where a human operator dynamically controls slave systems with slower or faster natural frequencies illustrate the efficacy of the proposed method. The study done in this Chapter is a proof of concept of the proposed control strategy in a physical system, and a step towards building a Human-Machine Interface that dynamically synchronize operator and legged robot in order to eventually achieve complex motor behaviors that require dynamic change of stance and stepping.

5.2 The Cart-Pole System

To illustrate the proposed strategy, we implement the bilateral feedback teleoperation law between a human operator and the Cart-Pole (see Figure 5-1). This is a 2 DoF underactuated system that closely resembles the LIP model utilized for the control of legged robots. It is essentially composed by a cart that moves on a linear rail (representing the robot CoP p_{xR}) and a pendulum that is passively attached to this cart. Moreover, the linear natural frequency of this pendulum is given by $\omega_R = \sqrt{\frac{g}{h_R}}$. Thus, by rotating the whole system on the X^R axis by an angle φ, we can change the effective gravity that the pendulum experiences and modify the natural frequency to $\omega_R = \sqrt{\frac{g cos(\varphi)}{h_R}}$. This trick is utilized to evaluate the control law for systems with different dynamics and is shown on Figure 5-2. Additionally, for this particular experiment, we assume that the human CoM height is approximately constant, $z_H \approx h_H$, and that the operator does not generate significant moments around the CoM, $M_{yH} \approx 0$. This assumption is a reasonable approximation for basic stepping motions [21] [22].

5.2.1 Cart-Pole Linear Model

The State Space equation of motion for the cart pole system is given by the linear matrix equation

$$\dot{\vec{q}}_{cp} = A_{cp}\vec{q}_{cp} + B_{cp}F_m,$$

which can be expanded to

$$\begin{bmatrix} \dot{p}_{xR} \\ \ddot{p}_{xR} \\ \dot{\theta} \\ \ddot{\theta} \end{bmatrix} = \begin{bmatrix} 0 & 1 & 0 & 0 \\ 0 & 0 & -\frac{g' h_R^2 m_R^2}{D} & 0 \\ 0 & 0 & 0 & 1 \\ 0 & 0 & \frac{g' h_R m_R M_T}{D} & 0 \end{bmatrix} \begin{bmatrix} p_{xR} \\ \dot{p}_{xR} \\ \theta \\ \dot{\theta} \end{bmatrix} + \begin{bmatrix} 0 \\ \frac{I_T}{D} \\ 0 \\ \frac{-h_R m_R}{D} \end{bmatrix} F_m, \tag{5.1}$$

where p_{xR} is the position of the cart of mass m_b; and θ is the angle that the inverted pendulum of length h_R, mass m_R, and moment of inertia I_R have with the Z^R axis. The motor

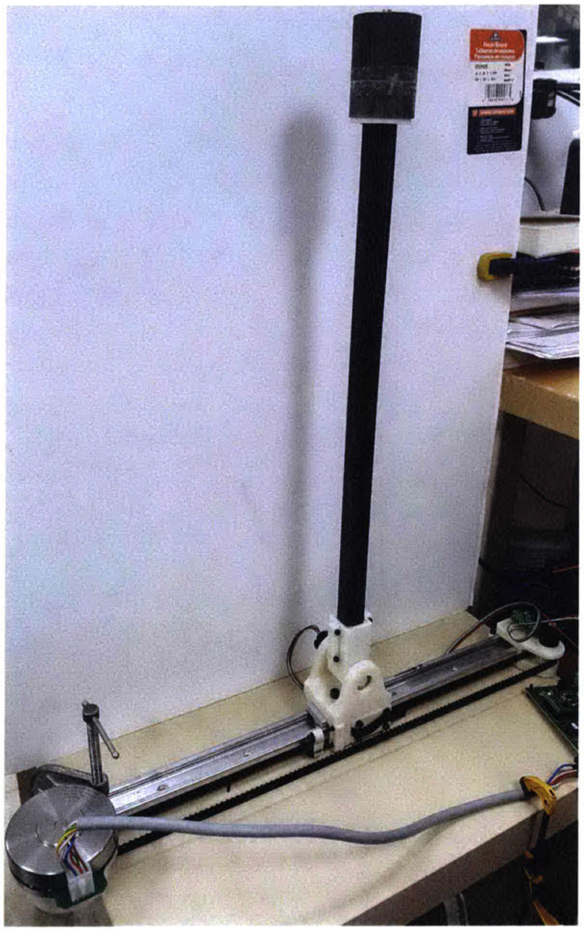

Figure 5-1: Cart-Pole constructed for the experiments in this Chapter.

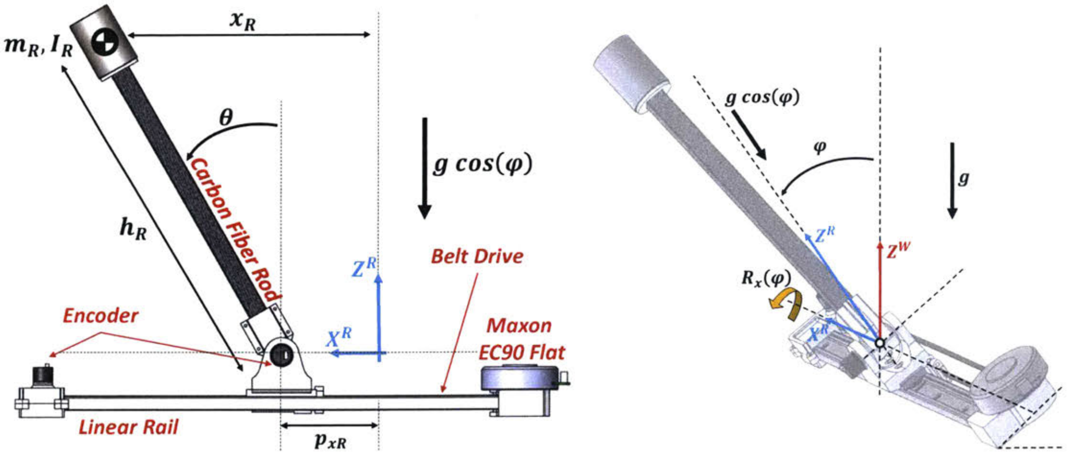

Figure 5-2: Left: Experimental cart-pole system utilized to represent the LIP model. The cart is positioned on the linear rail using a belt driven transmission and a torque-dense brushless motor. Its position p_{xR} models the robot CoP and defines the pendulum CoM acceleration. Right: by tilting the entire system about an angle φ around the X^R axis, we select the effective gravity that the pendulum experiences and, as a consequence, its natural frequency ω_R.

exerts a force F_m on the cart. Moreover, the constant D, the total mass M_T, total inertia around the pivot I_T, effective gravity g', and motor force are given by

$$\begin{aligned}
D &= m_R m_b h_R^2 + I_R\left(m_R + m_b\right),\\
M_T &= m_R + m_b,\\
I_T &= m_R h_R^2 + I_R,\\
g' &= gcos(\varphi),\\
F_m &= \frac{\tau}{r_p}.
\end{aligned}$$

Where φ is the angle between the robot Z^R and the world fixed Z^W; τ is the motor torque; and r_p is the radius of the driving pulley.

We can perform a change of variables to obtain the dynamics for the states in interest

$$\vec{q}_R = [p_{xR} \quad \dot{p}_{xR} \quad x_R \quad \xi_{xR}]^T$$

using the linear transformation

$$T_R = \begin{bmatrix} 1 & 0 & 0 & 0 \\ 0 & 1 & 0 & 0 \\ 1 & 0 & h_R & 0 \\ 1 & \frac{1}{\omega_R} & h_R & \frac{h_R}{\omega_R} \end{bmatrix}.$$

Thus, the new state transition matrices for $\vec{q}_R = T_R \vec{q}_{cp}$ are

$$A_R = T_R A_{cp} T_R^{-1},$$
$$B_R = T_R B_{cp}.$$

5.2.2 Cart-Pole Controller

Although the Cart-Pole shares valuable dynamic insights with the LIP model, its controller is fundamentally different from that of a legged robot. While the position of the CoP for the legged machine is defined by the forces applied against the ground, the position of p_{xR} is defined by physically moving the cart on the linear rail. Thus, due to the cart mass m_b, the Cart-Pole's CoP inherently has a finite bandwidth. In order to be able to reproduce the force bandwidth of a legged machine, the Cart-Pole actuator must have fast dynamics by reducing the actuator reflected inertia (by increasing r_p) and increasing the motor torque capacity. Here we utilize the Maxon EC90 Flat 48V.

The controller implemented for the cart pole is simply given by the linear full-state feedback law

$$F_m = -K_{cp}\left(\vec{q}_R - \vec{q}_R^{\,ref}\right). \tag{5.2}$$

Of which the gain $K_{cp} = [k_1 \quad k_2 \quad k_3 \quad k_4]$ can be obtained by methods such as a Linear Quadratic Regulator (LQR). Notice that the scalars k_1 and k_2 are positive values and define the PD controller that positions p_{xR} at the reference. The term k_4, on the other hand, is a negative value (positive feedback) that attempts to track the DCM reference ξ_{xR}^{ref}. Thus, while the absolute value of k_1 and k_2 define the tracking bandwidth of p_{xR}^{ref}, the difference between k_1 and k_4 defines the trade-off between CoP and DCM tracking. Finally, because in this work we attempt to track the DCM dynamics, the k_3 for CoM feedback is expected to be relatively low. In fact, during experiments we observe that setting this value to zero does not affect the overall teleoperation performance.

The reference vector is defined according to the teleoperation law described in the previous Chapter. The CoP and DCM references are simply given by the geometric similarity

$$p_{xR}^{ref} = \frac{h_R}{h_H} p_{xH}, \tag{5.3}$$

$$\xi_{xR}^{ref} = \frac{h_R}{h_H} \xi_{xH}. \tag{5.4}$$

Because of the LIP model, the CoM reference must take the horizontal force into account. Thus, we can plug equations (4.25) and (5.3) in the pendulum equation of motion (4.7) and obtain

$$x_R^{ref} = \frac{h_R}{h_H} \left(p_{xH} + \frac{F_{xH}}{m_H \omega_H^2} \right). \tag{5.5}$$

Finally, because the reference for the cart velocity would require the estimation of the time rate of change of the human force (which is unreasonably noisy for real systems), we simply set $\dot{p}_{xR}^{ref} = 0$. Thus, the reference is given by the transformation

$$\vec{q}_R^{ref} = \begin{bmatrix} p_{xR}^{ref} \\ \dot{p}_{xR}^{ref} \\ x_R^{ref} \\ \xi_{xR}^{ref} \end{bmatrix} = T_{ref} \vec{q}_H = \begin{bmatrix} \frac{h_R}{h_H} & 0 & 0 \\ 0 & 0 & 0 \\ \frac{h_R}{h_H} & 0 & \frac{h_R}{m_H h_H \omega_H^2} \\ 0 & \frac{h_R}{h_H} & 0 \end{bmatrix} \begin{bmatrix} p_{xH} \\ \xi_{xH} \\ F_{xH} \end{bmatrix}.$$

The complete closed-loop teleoperation is illustrated on Figure 5-3.

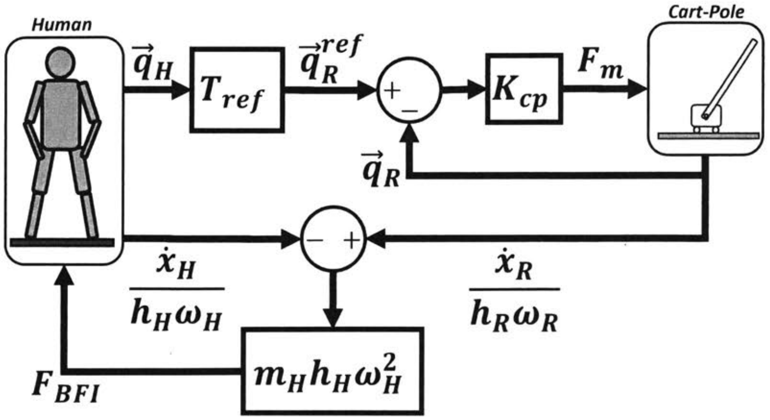

Figure 5-3: Block Diagram of the human and cart-pole closed-loop system. The human data is mapped to the robot as a feedback reference for the LQR controller utilizing the proposed teleoperation law. Simultaneously, the BFI applies to the operator forces that are proportional do the dimensionless difference in the CoM velocities.

5.3 Experimental Procedure and Results

For all three single-trial experiments in this section, an experienced operator performed side-to-side motions while standing on the BFI, including taking steps in place. Moreover, he was asked to minimize actions that cause large moments around the CoM such as arm swing or trunk roll (in order to validate the LIP model as shown in [21]). The pendulum length was defined as $h_R = 55cm$, the mass as $m_R = 1kg$ and we assumed $I_T \gg I_R$, or $I_R \approx 0$. Also, $r_p = 12.15mm$. The LQR gain K for all experiments was obtained by utilizing the cost matrices $Q = diag\left(\begin{bmatrix}15000 & 1 & 1 & 15000\end{bmatrix}\right)$ and $R = 10^{-1}$.

Figures 5-4 and 5-5 show the time evolution of the operator and pendulum CoP and DCM for $\varphi = 0°$ and $\varphi = 65°$, respectively. When $\varphi = 0°$, the pendulum has faster natural frequency than the operator: $\omega_R = 4.22s^{-1} > \omega_H = 3.12s^{-1}$. On the other hand, when $\varphi = 65°$, the natural frequency of the pendulum drops to $\omega_R = 2.75s^{-1}$, which correspond to an effective gravity of $g' = 0.77g$ (or a pendulum length of $h_R = 1.3h_H$). Two factors are noticed here: (i) the satisfactory tracking performance of both variables $\frac{p_{xR}}{h_R}$ and $\frac{\xi_{xR}}{h_R}$, and (ii) the inherent lower frequency of the motion when $\omega_R < \omega_H$. Figure 5-6 shows a snapshot of the teleoperation during single support, notice the unstable configuration of the pendulum and the geometric similarity between both systems (here $\frac{x_R}{h_R} = \frac{x_H}{h_H}$ because both CoM velocities are near zero).

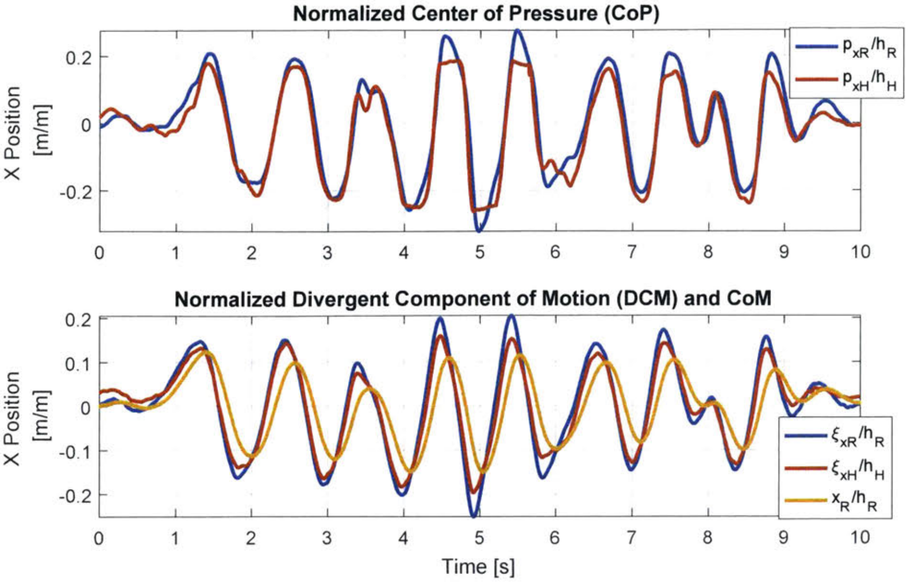

Figure 5-4: Experimental result for the teleoperation of a inverted pendulum with faster dynamics $\omega_R = 4.22s^{-1}$. The coupling between human and robot attempts to synchronize the robot ξ_{xR} and p_{xR} with the human reference. The RMSE for the CoP similarity is $0.05[m/m]$ and for the DCM similarity is $0.029[m/m]$.

Moreover, Figure 5-7 displays the human horizontal contact force F_{xH} and the feedback force F_{BFI} for both values of ω_R. Notice that when $\omega_R > \omega_H$ these forces are almost in phase, in fact the feedback is generated in order to speed up the human motion. The opposite is verified when $\omega_R < \omega_H$, when these forces are completely out of phase and the feedback force produces the effect of drag, slowing down the motion. In both cases, the resulting behavior lies between the natural response of both systems. This can be verified by the time delay of $\frac{p_{xR}}{h_R}$ in respect to $\frac{p_{xH}}{h_H}$ that we see in Figure 5-5 but is not evident in Figure 5-4. From equation (4.18) both DCM have similar dynamics, but are bounded by their characteristic response time. Refer to Figure 4-9 for a geometric interpretation of the result and the direction of the feedback force F_{BFI}.

Finally, the last experiment is depicted in Figure 5-8. Here, we set the gravity angle to $\varphi = 65^\circ$, thus $\omega_R < \omega_H$. Next, we evaluate the pendulum's ability to follow the operator during a prolonged single stance posture, with and without feedback. We set up the experiment such that the linear rail hard-stop coincides with the human foot position, thus the cart is physically not capable of moving beyond that point. From equation (4.14), if

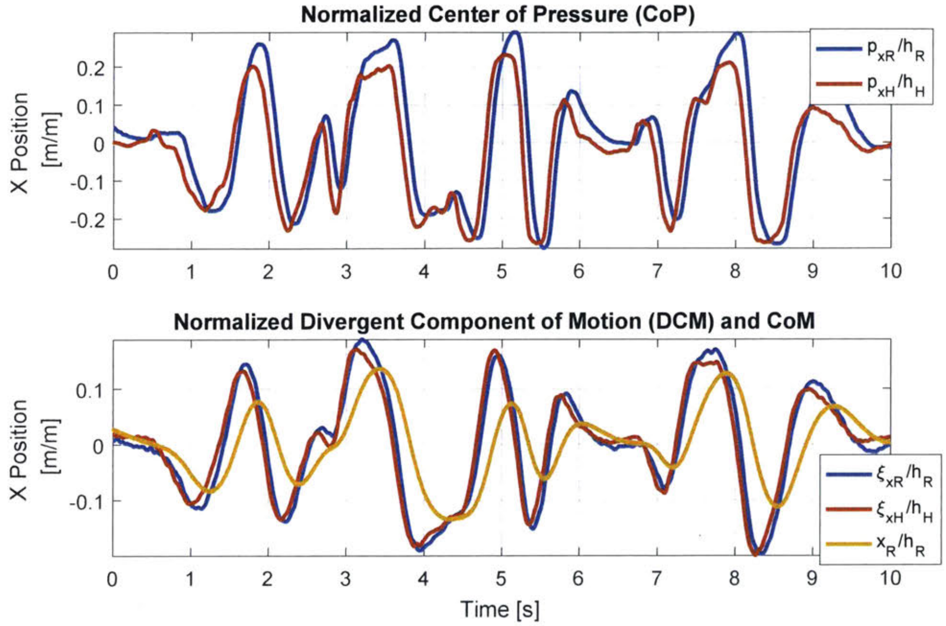

Normalized Center of Pressure (CoP)

Normalized Divergent Component of Motion (DCM) and CoM

Figure 5-5: Experimental result for the teleoperation of a inverted pendulum with slower dynamics $\omega_R = 2.75s^{-1}$. The coupling between human and robot attempts to synchronize the robot ξ_{xR} and p_{xR} with the human reference. The time delay ($\approx 80ms$) between p_{xR} and p_{xH} is due to the fact that the robot has slower dynamics than the human ($\omega_R < \omega_H$). The underactuated pendulum is unable to perform a dynamic motion that exceeds its characteristics time response (notice that $\dot{\xi}_{xR} = \omega_R(\xi_{xR} - p_{xR})$). Despite the short delay, the cart reproduces $\frac{h_R}{h_H} p_{xH}$ closely. The RMSE for the CoP similarity is $0.08[m/m]$ and for the DCM similarity is $0.023[m/m]$.

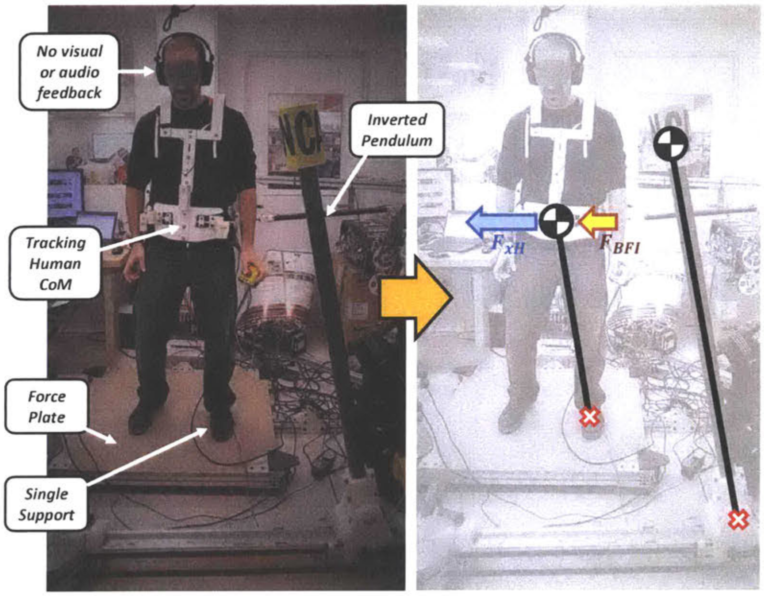

Figure 5-6: Snapshot of stepping experiment from Figure 5-4 at $\approx 5s$. The proposed teleoperation law enforces geometric similarity between operator and slave, from the single stance condition on the picture we can see that both systems share the same scaled CoP and the unstable configuration. Extreme pendulum angles can reach up to $\pm 10^\circ$ during dynamic motions. The direction of the human horizontal contact force is indicated in blue. In this case $\omega_R > \omega_H$, thus the feedback force F_{BFI} in yellow is on the same direction as F_{xH}.

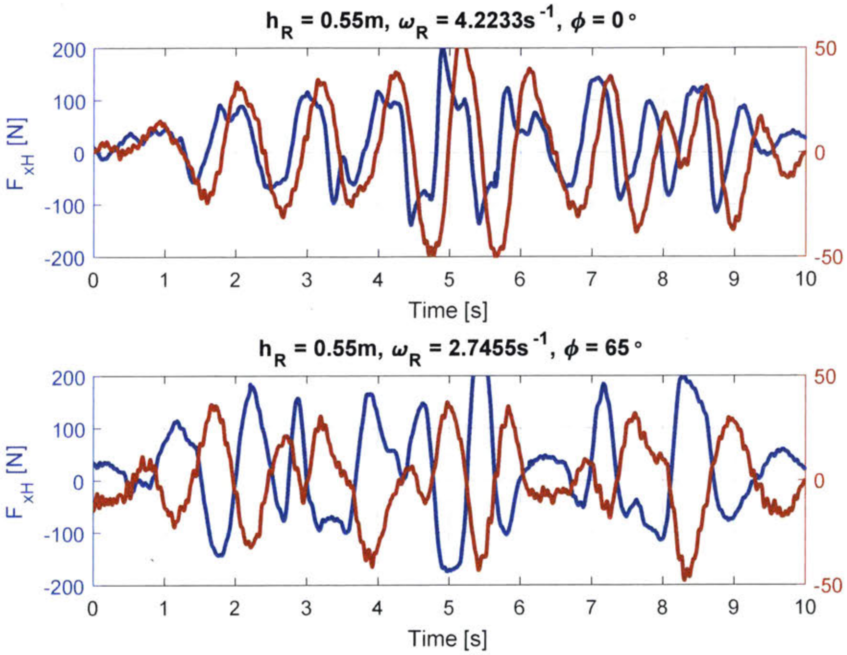

Figure 5-7: Horizontal forces applied to the human CoM during teleoperation of a faster (top) and slower (bottom) inverted pendulum. For the fast system, the feedback force, measured with a single-axis load cell, is on the same direction as the contact force, increasing the speed of the motion. In contrast, when the system is slower, the force is on the opposite direction, generating drag and slowing down the human motion.

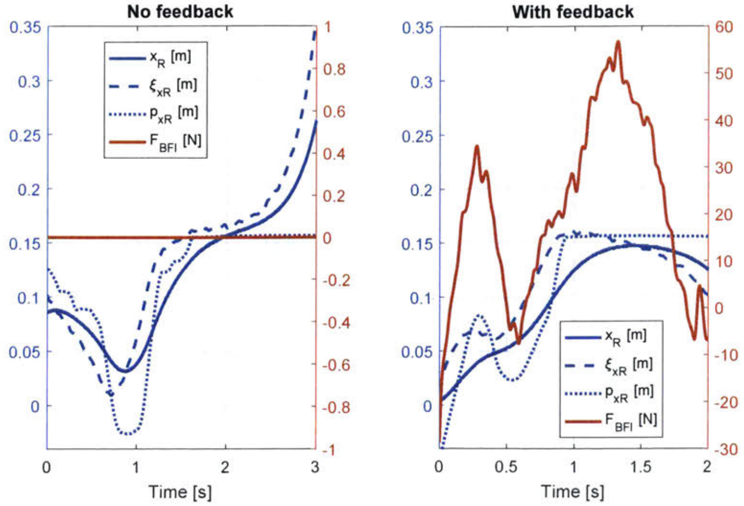

Figure 5-8: Evaluation of the stability of the inverted pendulum during teleoperation. Left: when there is no force feedback ($F_{BFI} = 0$) the motion towards single support is too fast and the cart cannot stabilize the pendulum with high orbital energy. Right: with the aid of the feedback information, the human generates a motion that does not exceeds the limits of balance of the cart-pole, which successfully stabilizes the pendulum during a prolonged single support posture.

the robot has slower natural frequency, it is required to place the CoP further away in order to achieve the same CoM acceleration. Thus, if there's no feedback ($F_{BFI} = 0$) and the pendulum orbital energy is too high, the cart will not be able to prevent the pendulum from tipping over, a situation we see on Figure 5-8-left. The right sub-figure, in contrast, shows the same scenario in the presence of F_{BFI}. This feedback input is able to slow down human motion, reducing the pendulum orbital energy and preventing instability. The robot motion is rendered stable given that the operator provides a stable trajectory.

5.4 Discussion

This study evaluates the feasibility of utilizing similarity for the mapping between human operator and bipedal robot. It is important to point out that the feedback force F_{BFI} is not designed solely to improve the stability of the slave robot, it is utilized basically to synchronize two system with different time characteristics. The goal of the strategy presented here is not to balance the pendulum, it is to create dynamic motion references online using human input. In other words, the BFI is utilized for:

1. Applying forces to the operator such that the master system generates dynamically feasible trajectories for the robot to track.
2. Inform the human operator about the robot dynamic characteristic (ω_R).
3. Inform the human about robot tracking performance (including external disturbances).

Hence, we assume that if the operator is aware of the robot dynamic state in real-time, then s/he can generate motions that are inherently stable for both systems or even create novel motion and balance strategies.

We can interpret the feedback gain k_4 for the ξ_{xR} state as the degree of "balancing autonomy" of the pendulum. If set to zero, the force applied to the cart is solely dependent on the human CoP reference (given that $k_1 \gg k_3$), thus, the human is completely responsible for maintaining the pendulum upright. In contrast, if k_4 is very large, the pendulum stability is effectively regulated by the LQR controller, regardless of the reference $\overrightarrow{q}_R^{ref}$. Proper tuning of this term reflects on the teleoperation performance and it is closely related to the robot controller feedback gain K_x from equation (4.32) [62].

The experimental setup utilized here provides an intuitive and visually appealing representation of the LIP, the template model commonly utilized for robot control. Nevertheless, despite not hurting the results of the analysis provided in this Chapter, this approach has some inherent disadvantages. For instance, the force lag from Figure 5-7 or the p_{xR} overshoot when the operator is in single support between $4s$ and $6s$ from Figure 5-4 are likely caused by:

1. The inertial properties of the cart and finite p_{xR} bandwidth. Accounted for the motor reflected inertia, the cart mass is about $m_b \approx \frac{I_{rotor}}{r_p^2} = 2kg$. This was mitigated by utilization of a torque-dense actuator.
2. The p_{xR} state feedback instead of force feedfoward. Ideally, for the control of a legged robot, equation (4.25) is utilized as a feedforward term for CoP placement. Here, because p_{xR} is a state, this information is mapped to the robot as feedback

reference. Thus, the cart position may not be able to faithfully reproduce the real CoP trajectory.

3. The simplicity of the LIP model. Although very powerful to represent core human motor behavior, the LIP cannot describe the full-body dynamics of the operator. Small moments around the CoM and vertical accelerations can corrupt the reference provided to the robot.

Finally, human learning plays an important role in all system that involve human and robot interaction. Although not the topic of this work, we assume that long-term experience with the control interface could greatly improve the synergy of the closed-loop system.

The next Chapters will describe the implementation of this methodology on a real bipedal robot Little HERMES [61]. The methods evaluated here can be directly extended to this scenario. The difference being that the robot can change the support stance and we prescribe the robot ground contact forces F_{xR} and F_{zH} instead of the CoP position. Additionally, because this robot is about $\frac{1}{3}$ human scale, the bilateral teleoperation strategy presented here will be fundamental for performing dynamic motions from human data in real-time.

Chapter 6

Design Principles for Dynamic Legged Robots

6.1 Introduction

The MIT Little HERMES, depicted in Figure 6-1, unifies a collection of design principles that are crucial for dynamic legged robots. These principles range from the actuator selection [80] and sensor design [11] to the overall system architecture such that agile walking and balancing maneuvers can be effectively implemented.

A robot that can successfully navigate the world functions due to the harmonic interplay between the hardware, the environment and the control algorithm. Thus, the machine cannot work properly if the designer does not take into account these three core items when planning the overall system architecture. Little HERMES' hardware design greatly facilitates robot control by exploring several key concepts that are described in this Chapter. First we show how the hardware design can be driven by the model template utilized for simulation and control from Chapter 4. Second, by proper actuation and transmission selection, open loop force control can be achieved through proprioception [63]. Next, by careful mass distribution, the system can effectively mitigate impacts and generate high bandwidth motions and forces. An impact-robust soft foot sensor is also developed, a lightweight device considerably more appropriate for locomotion than conventional force/torque (F/T) sensors [11]. Finally, we cover the overall system architecture, giving more details about

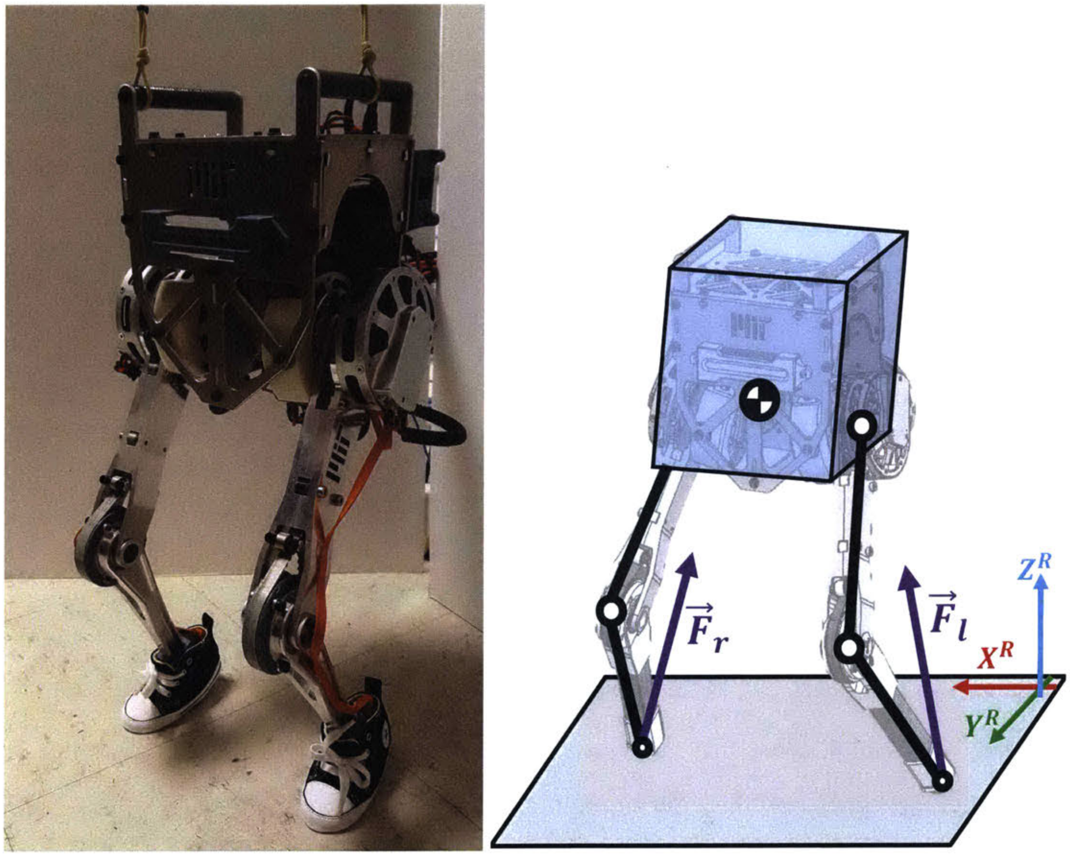

Figure 6-1: Left: The small-scale biped Little HERMES. Right: Single rigid-body model utilized for Little HERMES. The system is designed such that this simple template represents a major portion of the real system dynamic behavior. The legs are assumed to be massless force sources and can generate contact forces $\overrightarrow{F}_r$ and $\overrightarrow{F}_l$.

the computer control capabilities and the electronic setup.

6.2 From Template Model to Hardware Design

Many of the state-of-the-art legged machines are designed by independently developing the control algorithm and the physical system. On the other hand, the most successful highly dynamic machines are designed with a template in mind, often in such way that simplified models can be more effectively implemented [27][51][19]. The development of Little HERMES follows a similar approach. From Chapter 4 we define a template based on a single rigid-body floating base on which the legs are massless force sources (Figure 6-1).

In this model, the CoM is fixed to the floating base, the moment of inertia is given by a constant tensor (in the body-fixed frame) and the required joint torques to produce a desired contact force $\overrightarrow{F}_c$ is simply given by the Jacobian mapping $\overrightarrow{\tau} = J_c^T \overrightarrow{F}_c$ (due to the massless legs assumption). Where J_c is the Jacobian for the contact points. Each leg has three DoF: hip abduction/adduction, hip flexion/extension, and knee flexion/extension. The point feet can generate three components of forces when in contact with the ground (normal and shear). By regulating the ground reaction forces, the robot is able to generate momentum-based [41] and classic CoP-based [37] strategies to move and balance. The adoption of such template simplifies the state estimation and the regulation of joints torque to track CoM trajectories.

6.3 Actuator and Transmission Design for Proprioception

The actuator design plays a fundamental role regarding the robot's ability to properly control contact forces at high bandwidth: the basic assumption of most model-based controllers. To achieve such characteristic we adopt three key principles: (i) high torque-density motor; (ii) transparent actuator transmission; and (iii) current-control with regeneration capabilities. Little HERMES utilizes six custom actuator modules (see Figure 6-2) based on the commercial gimbal motor *ex-8 150KV* shown in Figure 6-3. The large gap radius actuator provides high torque density (continuous torque divided by mass $\frac{\tau_c}{m}$) imper-

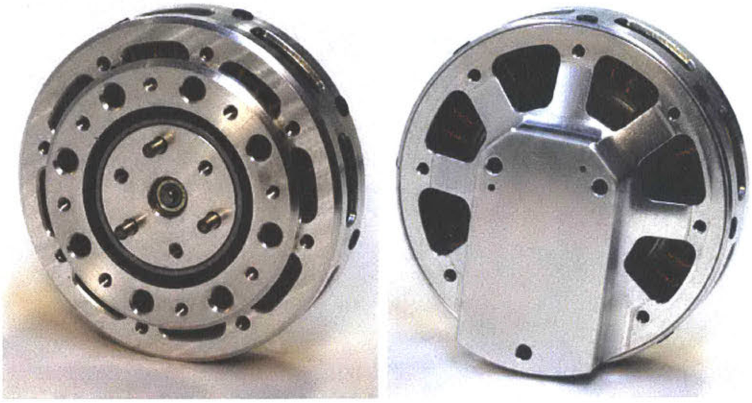

Figure 6-2: Custom brushless electric actuator. The high torque density reduces the gear reduction requirement, rendering a low reflected inertia and friction, characteristics that aid backdrivability of the limbs and impact robustness.

Figure 6-3: Electric gimbal motor with large gap radius utilized in the custom actuator. This motor is modified to include a 6 : 1 planetary gearbox and a custom driver.

ative for legged locomotion [63]. The low gear ratio (6:1), single stage planetary gearbox allows efficient torque transmission in both ways (negative and positive work) in a extremely compact form factor. The low-gearing and single-stage transmission minimizes friction losses, backlash, reflected rotor inertia, complexity and maintenance. The planetary setup provides multiple gear meshing contact points which distribute the stress to better handle impact during locomotion. Finally, the motor is current-controlled at high frequency ($40kHz$) by a custom driver. During negative joint work the controller recirculates part of the net energy back into the battery, working as an electric spring. Major characteristics are listed on Table 6.1. All these features allows backdrivability and precise open loop torque control at high bandwidth [63].

Table 6.1: Table of Parameters for Custom Actuator.

Motor parameter	Value
Continuous Torque	$5Nm$
Intermittent Torque	$17Nm$
Torque Constant (output)	$0.45Nm/A$
Rotor Inertia (output)	$0.0023kgm^2$
Gear ratio	$6:1$
Outer radius	$96mm$
Thickness	$40mm$
Weight	$480g$

6.4 Leg Design and the Impact Mitigation Factor

The leg design directly effects the robot's ability to control the contact forces with the environment and also mitigate unexpected impacts that often occur during locomotion. Low mass limbs require considerably less inertial and gravitational torque from the actuators, increasing force bandwidth and improving swing leg agility. Little HERMES' actuators are all placed proximal to the body, reducing leg inertia and leading to an effective CoM position that is virtually independent from leg state. Figure 6-4 shows the robot in several extreme leg configurations, revealing only small deviation of the CoM from the nominal position. Figure 6-4 also depicts a detailed view of the belt transmission for the knee, allowing the actuator to be mounted coaxially with the hip motor and near the CoM.

Leg inertia and motor reflected inertia also ultimately define limb backdrivability and the ability to absorb impacts with the environment. A previous study [80] evaluated this effect for floating base legged systems and the main results are covered here. Consider the floating base legged system with equations of motion described by the matrix expression

$$H\ddot{\vec{q}} + h\left(\vec{q}, \dot{\vec{q}}\right) = S^T \vec{\tau} + J_c^T \vec{F}_c. \tag{6.1}$$

Where H is the inertia matrix, h is the Coriollis and Gravitational torques vector, $\vec{\tau}$ is the vector of joint torques and S is a input selection matrix. The inertia matrix H and the robot state q can be split in a floating base component (H_b and $\vec{q}_{bb}$) and a leg component (H_{ll}

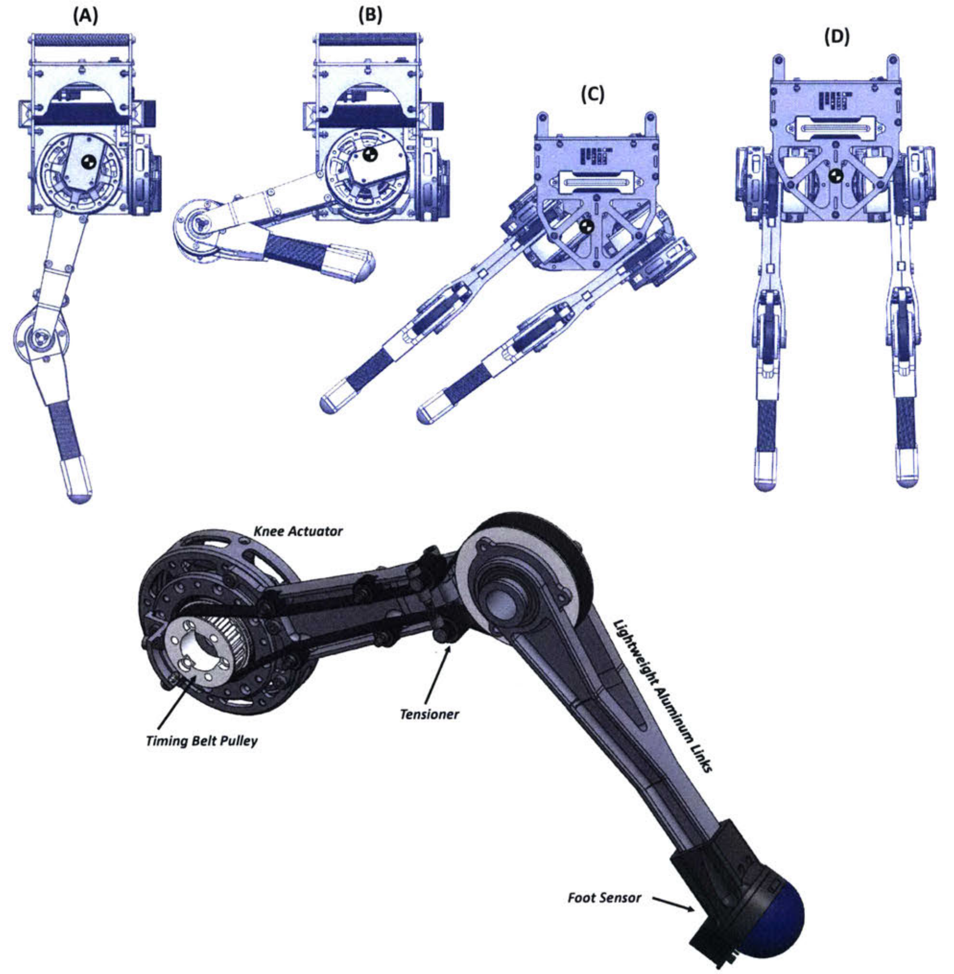

Figure 6-4: Top: Extreme configurations of the robot's limbs. Notice the small CoM deviation from nominal position: about 24*mm* from A to B and 19*mm* for C to D. Bottom: Detailed view of the highly efficient 1.6:1 timing belt transmission to drive the knee. The large wrapping angle on both the motor and knee pulleys, reduces tooth stress and wear. The knee actuator is mounted proximal to the body and in a collinear axis with the hip flexion/extension motor.

and $\overrightarrow{q}_l$):

$$H = \begin{bmatrix} H_{bb} & H_{bl} \\ H_{lb} & H_{ll} \end{bmatrix}, \quad \overrightarrow{q} = \begin{bmatrix} \overrightarrow{q}_b \\ \overrightarrow{q}_l \end{bmatrix}. \tag{6.2}$$

If the systems impacts the ground with velocity v, the impulse generated is given by $\rho = -\Lambda v$. Thus, the operational space inertia matrix (from the foot point of contact with Jacboian J_c) is given by $\Lambda = \left(J_c H^{-1} J_c^T\right)^{-1}$. Similarly, splitting the contact Jacobian between body and leg components gives $J_c = \begin{bmatrix} J_b & J_l \end{bmatrix}$. And an operational space inertia matrix equivalent to all joints locked in place (infinite motor reflected inertia and limb inertia)

$$\Lambda_L = \left(J_b H_{bb}^{-1} J_b^T\right)^{-1}. \tag{6.3}$$

The Directional Impact Mitigation Factor (DIMF) is given by the ratio between the complete Λ and the locked Λ_L operational space matrices given a certain direction $\hat{e}$.

$$\xi_{\hat{e}} = 1 - \frac{\hat{e}^T \Lambda \hat{e}}{\hat{e}^T \Lambda_L \hat{e}}. \tag{6.4}$$

This dimensionless term represents inertial energetic losses during impact and partially characterize backdrivability. An $\xi_{\hat{e}} = 1$ indicates perfect inertial backdrivability that eliminates all impact, similarly $\xi_{\hat{e}} \rightarrow 0$ indicates the opposite as $\Lambda \rightarrow \Lambda_L$. Notice that the actuator reflected inertia is included in the inertia matrix H_{ll}. Thus, large gear ratios increase the limb reflected inertia and reduces the robot's ability to deal with impact. The DIMF can also evaluate the effect of the actuator reflected inertia for impact losses. Given the rotor inertia I_{rotor} and transmission reduction N_t, the leg will experience an added inertia of $I_{rotor} N_t^2$. In fact, adding the motor inertia modifies the operational space inertia matrix such that [80]

$$\Lambda = \left(J_c \left(H + H_{rotor}\right)^{-1} J_c^T\right)^{-1}. \tag{6.5}$$

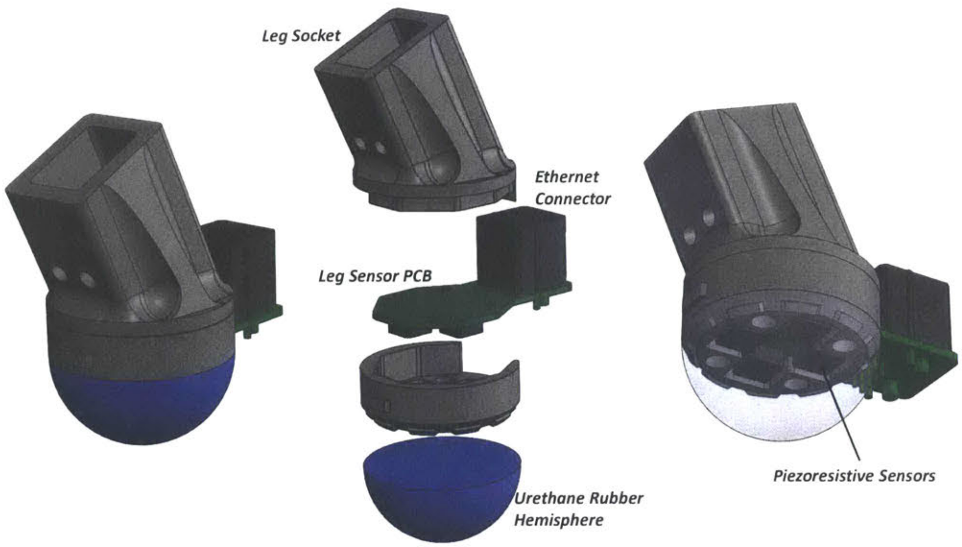

Figure 6-5: CAD representation of the robot's soft foot sensor. The hemispherical urethane rubber contacts the ground and deforms under load. The pressure increase from this deformation is captured by an array of pizeoresistive sensors. This lightweight, waterproof device can measure shear and normal forces applied to the rubber hemisphere.

6.5 Foot Sensor

To measure accurate ground reaction forces, a sensing footpad was customized for Little HERMES. This is based on the previous work with piezoresistive sensor (modified from the *MPXH6400A* from *Freescale Semiconductor*) arrays embedded in polyurethane rubber that was developed for the MIT Cheetah robot [11]. Instead of a rectangular footpad shape as in previous works, the polyurethane rubber material (Vytaflex 40) was made spherical to better simulate point contact. A rubber material is used so that the footpad is robust to repeated impacts [11] such as when Little HERMES is undergoing locomotion. Figure 6-5 shows a cutaway view that depicts the arrangement of the sensors within the footpad.

6.5.1 Calibration

The output voltages $\overrightarrow{V} = [V_1 \quad V_2 \quad V_3 \quad V_4]^T$ provided by the array of piezoresistive sensors is surprisingly linearly proportional to the forces applied to the feet's sole. In fact, the normal and shear components of the force $\overrightarrow{F}^{foot} = \left[F_x^{foot} \quad F_y^{foot} \quad F_z^{foot}\right]^T$ can be closely

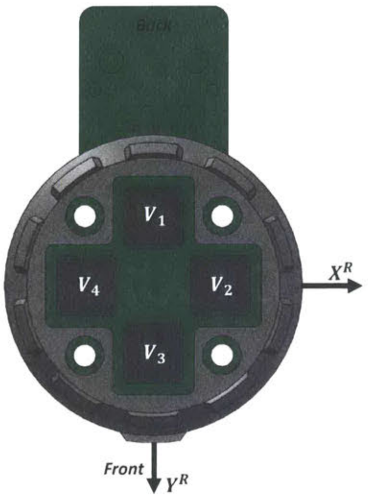

Figure 6-6: Array of four pizeoresistive sensors mounted to the bottom of the foot sensor, inside the urethane hemisphere (not shown).

estimated by the linear matrix expression

$$\vec{F}^{foot} = K^{foot}\vec{V},$$

where K^{foot} is a constant matrix calibrated from the collected data. Intuitively, the normal component is proportional to the absolute sum of all values while the shear components can be estimated by the difference between two opposing sensors. The foot sensor was calibrated using a commercially available force/torque sensor *ATI Delta SI-660-60* from *ATI Industrial Automation*. The linear behavior is achieved in part due to the hardness of the urethane rubber utilized here (40 *ShoreA*). Harder materials provide higher sensitivity to force but saturates the sensors at a lower load. This design trade-off must be considered for the fabrication of these sensors.

It is important to point out that the feet sensors were used in this work as simple contact switches and to measure the time evolution of the robot CoP. They were not utilized for closed-loop force control, which is achieved by current-based open-loop torque control and leg kinematics, which we define as Proprioceptive force control [63]. Figures 6-7 and 6-8 shows the feet force control performance during experiments on a force plate from *Kistler Instruments* type *9260AA3*.

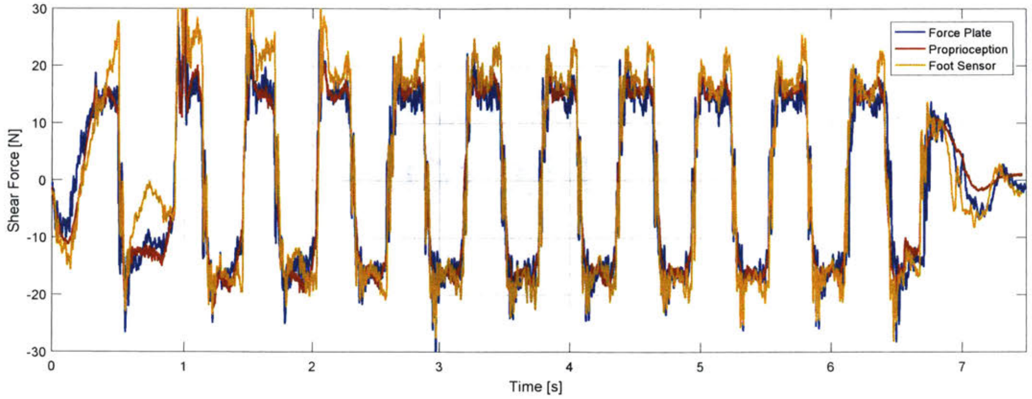

Figure 6-7: Shear component of the total contact force for a stepping in place experiment. Proprioception is defined as the foot force open-loop control performed via commanded motor current and leg kinematics alone, without utilization of force-torque sensors.

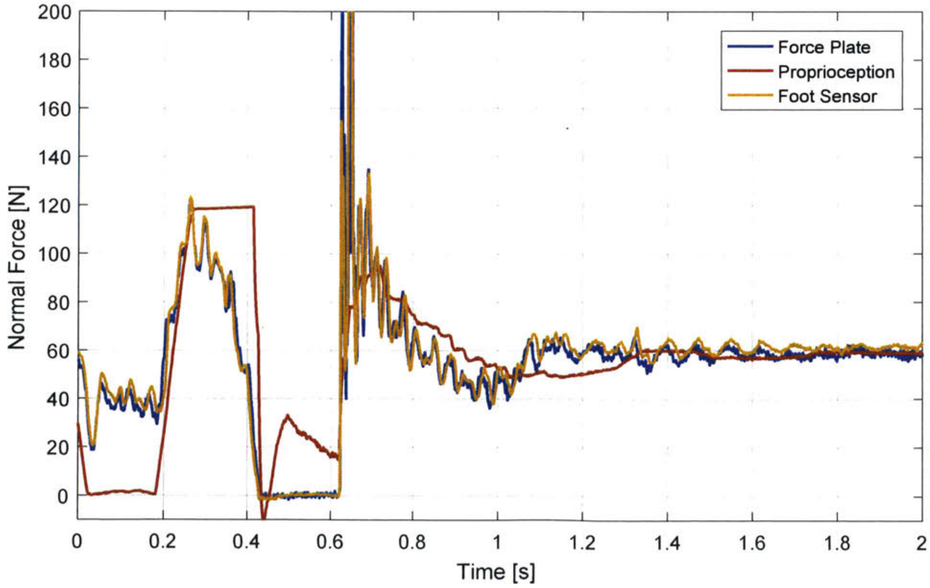

Figure 6-8: Normal component of the total contact force for a jumping experiment. Proprioception is defined as the foot force open-loop control performed via commanded motor current and leg kinematics alone, without utilization of force-torque sensors.

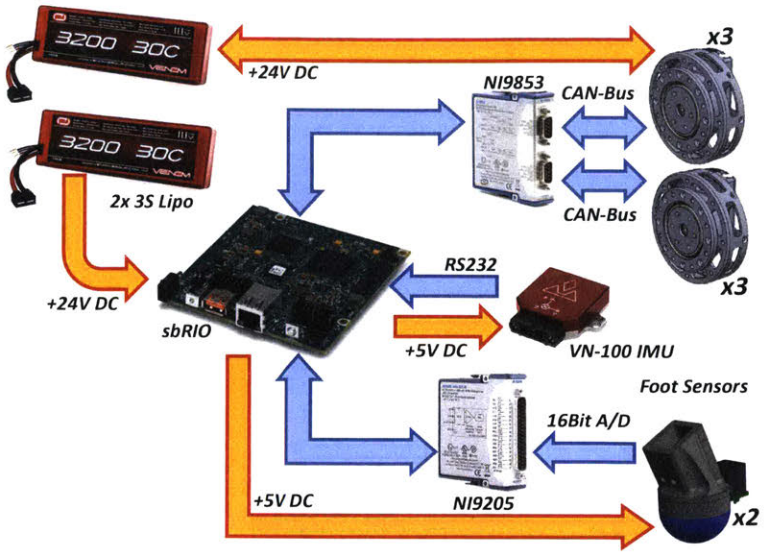

Figure 6-9: System Layout for Little HERMES. The real-time computer communicates in high-speed CAN bus with the six actuators and interfaces with the IMU and foot sensors. The whole system is powered by two LiPo 3S batteries. Red arrows indicate power bus and blue arrows indicate low-power communication. Bidirectional arrows represents buses that flows both ways.

6.6 System Architecture

The overall system layout is depicted in Figure 6-9 and the machine main dimensions is shown in Figure 6-10. The main embedded real-time computer is a NI9606 sbRIO from *National Insturments* with a Xilinx Spartan-6 FPGA. It communicates with the six actuators through a dual channel high-speed CAN-bus card NI9853. A second card for Analog Inputs, NI9205, interfaces the main computer and the foot sensors. A *VectorNav* VN-100 IMU provides body orientation and angular rates at $100Hz$. The control loop time in the real-time computer is programmed to be $1.8ms$. The whole system is powered by two 3-Cell *Venom* Lithium Polymer batteries with hard case. A voltage regulator isolates the DC input provided to the computer from the power applied to the motors. The batteries are placed close to the robot CoM in order to reduce body rotational inertia.

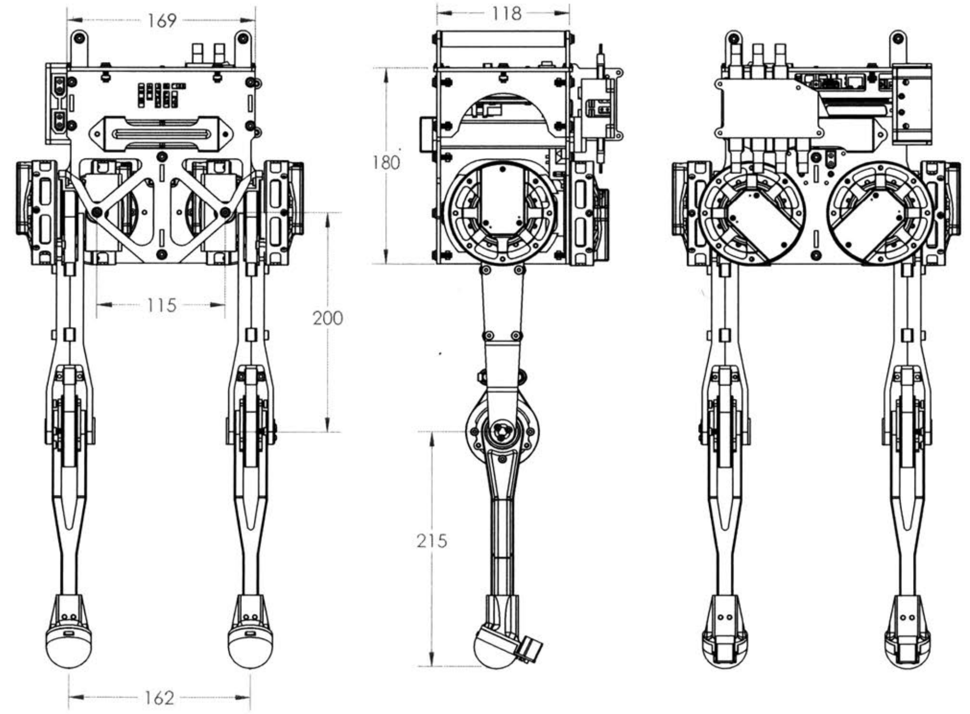

Figure 6-10: Major dimensions and characteristics of Little HERMES. The scheme shows the coaxial hip/knee actuators, carbon fiber lower leg, and other important features. The machine weights about 6*kg* with the batteries and embedded computer. All dimensions are in millimeters.

6.7 Discussion

Proper design of actuators and sensors for legged robots is an issue that is often overlooked in the robotics community. We argue that the capability of a machine of performing dynamic tasks rely heavily on the co-design of the hardware and the controller. This Chapter describes a collection of design principles that are essential to allow legged robots to achieve behaviors that require force control, negative work and impact. This design process illustrates a paradigm shift from the classic high-gear-ratio robots with stiff joints to machines that can achieve programmable compliant behavior at high bandwidth. Following this idea, Little HERMES' design approximates the physical hardware to the model utilized in Chapter 4. Design approaches similar to the one described in this Chapter are becoming more popular in the literature [63][34][59][44][27].

Moreover, Little HERMES is a relatively simple robot with only three Degrees of Freedom per leg. The challenge of reducing the limb inertia becomes considerably harder when a large number of joints are involved, especially with the inclusion of ankle/wrist joints. Moreover, the small scale of the robot permits the utilization of off-the-shelf electric actuators for Proprioceptive force control. Larger robots may require electric motors with custom configurations (windings and magnets), as in the case of the MIT Cheetah robot [63]. Finally, the point feet assumption allows the design of a simple foot sensor. A robot model with finite-size foot would require a sole with a much larger array of piezoresistive sensors. Additionally, a similar sensor would wear out much faster when utilized in heavier machines.

Chapter 7

Bilateral Teleoperation of a Dynamic Bipedal Robot

7.1 Introduction

The realization of the bilateral teleoperation strategy introduced in Chapter 4 on a real machine requires addressing a multitude of challenges. These challenges include limitations of the simple model utilized in this Thesis, as well as the physical constraints inherent in the hardware. In this Chapter, we first define the scope of the experiments and narrow down the study to a particular plane of the dynamics in order to gain fundamental insights about the system behavior. For all the experiments in this Chapter, we constrain Little HERMES' motion to the Frontal Plane by utilizing a spherical Boom as shown in Figure 7-1. It must be noted that the theory present here is analogous in the Frontal or Sagittal Planes. The teleoperation law presented in Chapter 4 needs to be modified here to include swing leg dynamics and controller transitions due to impacts. Next, we show the complete picture of the closed-loop system and the computational flow for each particular subsystem. Finally, we describe in more detail the relevant experiments conducted with the bipedal robot such as dynamic balancing and taking steps in place, the basic behaviors necessary for walking.

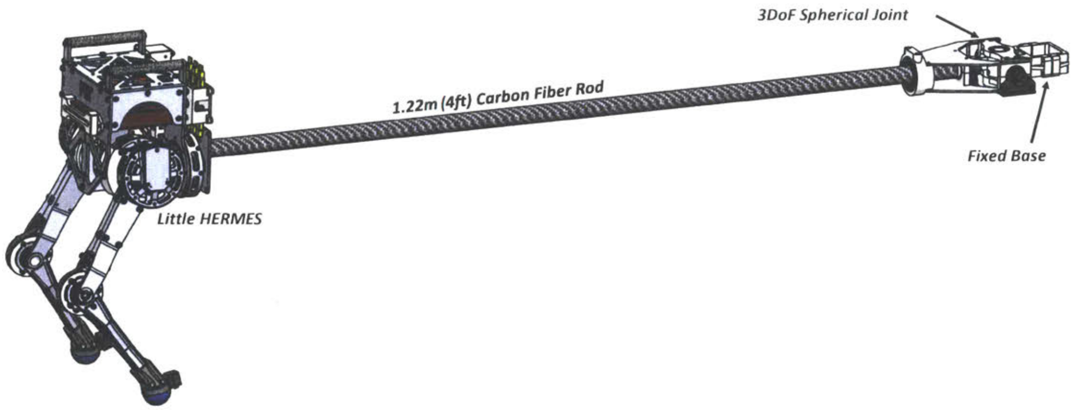

Figure 7-1: The robot is constraint move approximately in the Frontal Plane using a spherical boom with a large radius. The utilization of a long Carbon Fiber rod improves the accuracy of such approximation.

7.2 Robot Controller

7.2.1 Similarity-Based Scaling

Let's define the stance ratio to be the ratio between the CoM height z_R and the horizontal distance d_R between feet, as shown in Figure 7-2. In Chapter 4, because we assumed in simulation that the legs had no swing dynamics, the virtual robot was always able to maintain a stance ratio similar to the human's ($\frac{d_R}{z_R} = \frac{d_H}{z_H}$).

However, because the human and robot structures are fundamentally different, they may have different nominal distance between the feet, which is usually dictated by the distance between hip joints. For example, in this chapter, human nominal ratio for this particular operator is $\frac{d_{0H}}{h_H} = \frac{0.6m}{1.25m} = 0.48$, while the robot nominal ratio is $\frac{d_{0R}}{h_R} = \frac{0.3m}{0.38m} = 0.625$. Thus, we need to modify the previous presented equations for dynamic scaling in order to account for this difference. Horizontal geometric scaling is normalized according to the nominal distance between feet d_{0i}, and vertical geometric scaling is performed with the vertical height h_i, for $i = [H, R]$. Thus, equations (4.17) and (4.18) now are written

$$\frac{\xi_{xR}}{d_{0R}} = \frac{\xi_{xH}}{d_{0H}}, \tag{7.1}$$

$$\frac{\dot{\xi}_{xR}}{d_{0R}\omega_R} = \frac{\dot{\xi}_{xH}}{d_{0H}\omega_H}. \tag{7.2}$$

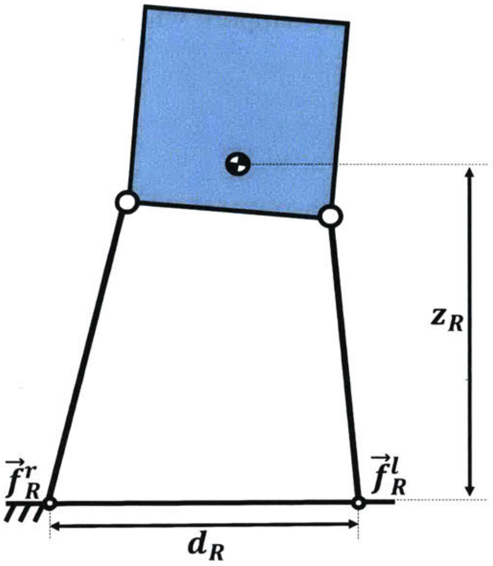

Figure 7-2: Representation of the robot stance ratio: the ratio between the horizontal distance between feet and the CoM height $\frac{d_R}{z_R}$. For the experiments in this Chapter, horizontal scaling components are normalized using the nominal distance d_{0R} and d_{0H}.

Following the same procedure as before, we can rewrite the horizontal force scaling (4.25) and the Feedback Control (4.27) law as

$$F_x^{ff} = \frac{m_R d_{0R} \omega_R^2}{m_H d_{0H} \omega_H^2} F_{xH}, \tag{7.3}$$

$$F_{BFI} = m_H d_{0H} \omega_H^2 \left(\frac{\dot{x}_R}{d_{0R}\omega_R} - \frac{\dot{x}_H}{d_{0H}\omega_H} \right). \tag{7.4}$$

Notice that the vertical force scaling is maintained the same as in equation (4.28). However, the feedfoward term for the moment around the CoM from equation (4.47) must now be

$$M_y^{ff} = \frac{m_R d_R z_R \omega_R^2}{m_H d_H z_H \omega_H^2} M_{yH}. \tag{7.5}$$

The leg force controller for the stance leg is the same as the one described for the simulated robot. Given the number of contacts and the feet position, we can estimate the desired leg forces from equations (4.54) to (4.57). If flight is to occur (loss of both contact points), the robot is required to maintain a prescribed leg impedance at nominal stance and wait for contact. Additionally, given the finite inertia of the real robot legs, we cannot use the swing leg controller as presented in equation (4.60). Hence, we must now define a controller for the swing leg during single support, when the robot attempts to follow human foot trajectory.

Swing Leg Controller

Swing leg control is performed in joint space by determining the joint trajectory reference from inverse kinematics. For instance, given the right foot trajectory

$$\vec{f}^{\,r}_{Rref}(t) = \begin{bmatrix} f^r_{xRref}(t) \\ f^r_{yRref}(t) \\ f^r_{zRref}(t) \end{bmatrix},$$

we evaluate the the desired joint space trajectory

$$\vec{\theta}^{\,r}_{Rref}(t) = \begin{bmatrix} \theta^r_{1Rref}(t) \\ \theta^r_{2Rref}(t) \\ \theta^r_{3Rref}(t) \end{bmatrix},$$

and their first and second time derivatives, $\dot{\vec{\theta}}^{\,r}_{Rref}(t)$ and $\ddot{\vec{\theta}}^{\,r}_{Rref}(t)$. Thus, during left leg support, the commanded torques for the right leg are given by

$$\vec{\tau}^{\,r}_{R}(t) = \begin{bmatrix} \tau^r_{1R}(t) \\ \tau^r_{2R}(t) \\ \tau^r_{3R}(t) \end{bmatrix} = K^r_p\left(\vec{\theta}^{\,r}_{Rref} - \vec{\theta}^{\,r}_{R}\right) + K^r_d\left(\dot{\vec{\theta}}^{\,r}_{Rref} - \dot{\vec{\theta}}^{\,r}_{R}\right) + K^r_{ff}\ddot{\vec{\theta}}^{\,r}_{Rref}.$$

Where K^r_p, K^r_d and K^r_{ff} are proportional, derivative and feedfoward gains. The controller for the left leg during right leg support is analogous.

Because the robot is constrained to move in the frontal plane, the off-plane reference for the foot $f^r_{yRref}(t)$ is simply set to zero. The horizontal reference in X^R direction is provided given human current foot position normalized by the nominal feet spam d_{0H}. Hence, we write

$$f^r_{xRref}(t) = f^l_{xR}(t) + \frac{d_{0R}}{d_{0H}}\left(f^r_{xH}(t) - f^l_{xH}(t)\right). \tag{7.6}$$

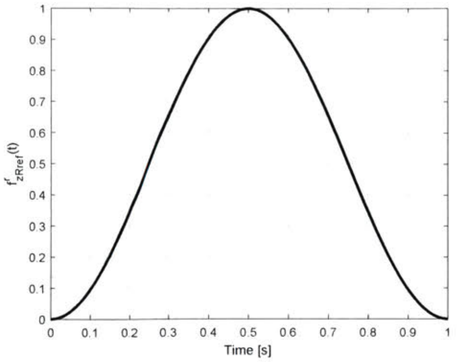

Figure 7-3: Predefined swing foot vertical trajectory. The robot follows this swing trajectory when it detects a loss of contact. The amplitude $A_H(t)$ is adjusted according to human swing foot height. If the robot touches the ground early during swing, the trajectory is terminated and the robot holds that foot in place.

Because the swing time is normally very short $(150 - 200ms)$, a different strategy is adopted for the vertical foot trajectory reference (Z^R). At every occasion that the robot detects a loss of a point of contact of, for example, the right foot, it immediately follows a predefined trajectory that is simply readjusted according to the human right foot height. This foot trajectory is define as

$$f^r_{zRref}(t) = \begin{cases} f^r_z(t_0) + \frac{A_H(t)}{2}\left[1 - cos\left(2\pi\frac{t-t_0}{T_s}\right)\right], & t_0 \leq t \leq Ts \\ f^r_z(t_0), & otherwise \end{cases}.$$

Which is depicted in figure 7-3 for initial swing time $t_0 = 0s$, constant vertical amplitude $A_H(t) = 1m$ and swing time $T_s = 1s$. Noticed that any other function, such as a Bezier Polynomial, can be utilized here. Finally, we scale the term $A_H(t)$ from the human foot height:

$$A_H(t) = \frac{h_R}{h_H} f^r_{zH}(t).$$

For the experiments conducted in this Chapter, we fix $T_s = 0.2s$. Figure 7-4 shows a typical vertical tracking performance for the robot taking steps. As future work, the human swing time can be predicted by the initial vertical take-off velocity of the foot. More interestingly, if the human swing leg trajectory can be anticipated, the robot foot tracking performance

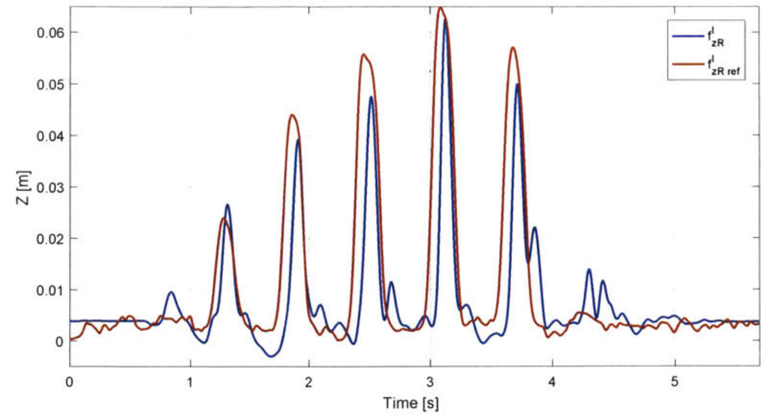

Figure 7-4: Tracking performance for left swing foot during right leg stance. Notice that the swing time is only about $200ms$. In addition, the feet do not rest at zero height because this data is collected from leg kinematics, which can accumulate error. Despite lightweight, the real leg inertia prevents the foot from following arbitrarily fast trajectories.

can be improved even further.

7.2.2 Torque Smoothing

The controllers for each component of the state machine are considerably different from each other because the impedance of the robot's environment varies greatly between contact and swing. On the other hand, commanding discontinuous forces to the robot legs may cause a number of issues such as contact instabilities and/or large input steps. To mitigate this issue we introduce a term that smoothly transitions the commanded torque between each state machine controller.

We define a binary variable C^r that instantaneously flip according to the contact condition of the right foot, defined by a minimum vertical force F_{min} measured by the foot force sensor, or

$$C^r = \begin{cases} 1, & F^r_{zR} \geq F_{min} \\ 0, & otherwise \end{cases}.$$

The smooth contact indicator $\alpha^r(t)$ transfer function for the right foot is, thus, given by

$$\frac{\alpha^r(s)}{C^r(s)} = \frac{1}{\tau_c s + 1}.$$

Where τ_c is a contact transition timing constant that, for the experiments in this work, we define as $\tau_c = 10ms$, and the minimum force as $F_{min} = 1N$. Finally, after evaluating an equivalent variable α^l for the left leg, the torque that is commanded to the right leg joints, is given by

$$\vec{\tau}^r_R = \alpha^r\alpha^l\vec{\tau}^r_{DS} + (1-\alpha^r)\alpha^l\vec{\tau}^r_{LS} + \alpha^r\left(1-\alpha^l\right)\vec{\tau}^r_{RS} + (1-\alpha^r)\left(1-\alpha^l\right)\vec{\tau}^r_{FP},$$

where $\vec{\tau}^r_{DS}$, $\vec{\tau}^r_{LS}$, $\vec{\tau}^r_{RS}$ and $\vec{\tau}^r_{FP}$ are the commanded motor torques from the double support, left leg support, right leg support and flight phase controllers, respectively. The controller for the left leg torques is analogous.

7.3 Control Loop and Data Flow

Figure 7-5 depicts the detailed computational flow for the teleoperation strategy adopted during the experiments. In this Section, we break down the control-loop and describe each block of the diagram independently. In figure 7-5, green blocks indicates procedures that are carried out once before the control loop starts, dark blue blocks indicate input data from sensors, red blocks represent commanded effort to the actuators, the arrow in magenta indicate information flow from robot to the BFI, while the yellow arrow shows the opposite flow. Each of the steps represented by the gray boxes in the BFI control loop are described next:

1. H_0: The BFI joint angles are set to initial positions to be calibrated and the force offset is measured from the force plate sensors.

2. H_1 to H_3: The angle from each joint is measured from the $12bit$ encoders as well as the values recorded by the force plate and BFI force sensor.

3. H_4 and H_5: Performing forward kinematic of the serial linkages, we calculate the feet spatial position and the torso posture, which provides the states for the model.

4. H_6: From the current CoM state, the Divergent Component of Motion can be estimated.

5. H_7: The CoP, as well as the contact forces are measured utilizing the force plate. The total moment M_{yH} around the CoM is, thus, calculated from the CoP equation (4.46).

6. H_8: Next, we perform the similarity-based scaling of the human DCM as well as the horizontal and vertical forces. This information is transfered to the robot's controller.

7. H_9: An e-Stop button is available for the operator to deactivate the BFI actuator in case of danger.

8. H_{10}: From the comparison between robot and human states, the feedback force F_{BFI} is commanded to the actuator.

The subsystems for the robot control loop are also described:

1. R_0: The robot's leg joints are positioned at known configurations so the encoders offset can be measured. At the same time, we record the offset value measured by the feet force sensors.

2. R_1 to R_3: All the joints encoder values are read, as well as the body linear acceleration, angular velocities and angular orientations from the Inertial Measurement Unit (IMU). The forces measured by the feet are obtained.

3. R_4: From the leg forward kinematics we can estimate the feet position relative to the body.

4. $R5$: Given the force measured by the feet sensors, we define the number of valid contact points.

5. R_6 and R_7: From the leg kinematics, number of contact points and IMU readings we estimate the CoM state. These can be utilized to estimate the robot's DCM.

6. R_8 and R_9: Given the DCM, the contact point(s) position and the human reference from the similarity-based mapping, the robot selects the state machine controller and defines the required forces each leg must produce.

7. R_{10} and R_{11}: The task-space forces are mapped into joint-space torques utilizing the contact Jacobian matrix $\overrightarrow{\tau} = J_c^T \overrightarrow{F}_{leg}$. Additionally, the commanded joint torques are filtered using the contact transition variables α^r and α^l.

8. R_{12} and R_{13}: To improve the stability during contact, a small joint-level damping term is added. Additionally, to avoid leg singularities and other extreme configurations, soft stops are superimpose to the leg controller.

9. R_{14}: An e-Stop button is available for the operator to turn off all the robot joints in case of danger.

10. R_{15}: Finally, the real-time computer commands the desired torques to the robot actuators.

7.4 Experimental Results

Several experiments were conducted in order to evaluate the performance of the proposed teleoperation mapping and control law. It must be noticed that, given the point foot design of the robot, any stepping action must be achieved via a dynamically stable trajectory, in other words, the robot is unable to freeze the posture mid-motion. Additionally, when all references are set to zero, the robot still possess a reactive controller that balances the system upright and selects foot placements to remain at nominal stance. Figure 7-6 shows the performance of this controller for unstructured terrain.

7.4.1 Stance Tracking during Double Support

The simplest motion that can be performed by the robot is a simple side-to-side oscillation when both contact points are preserved (double support). Figure 7-7 depicts this scenario.

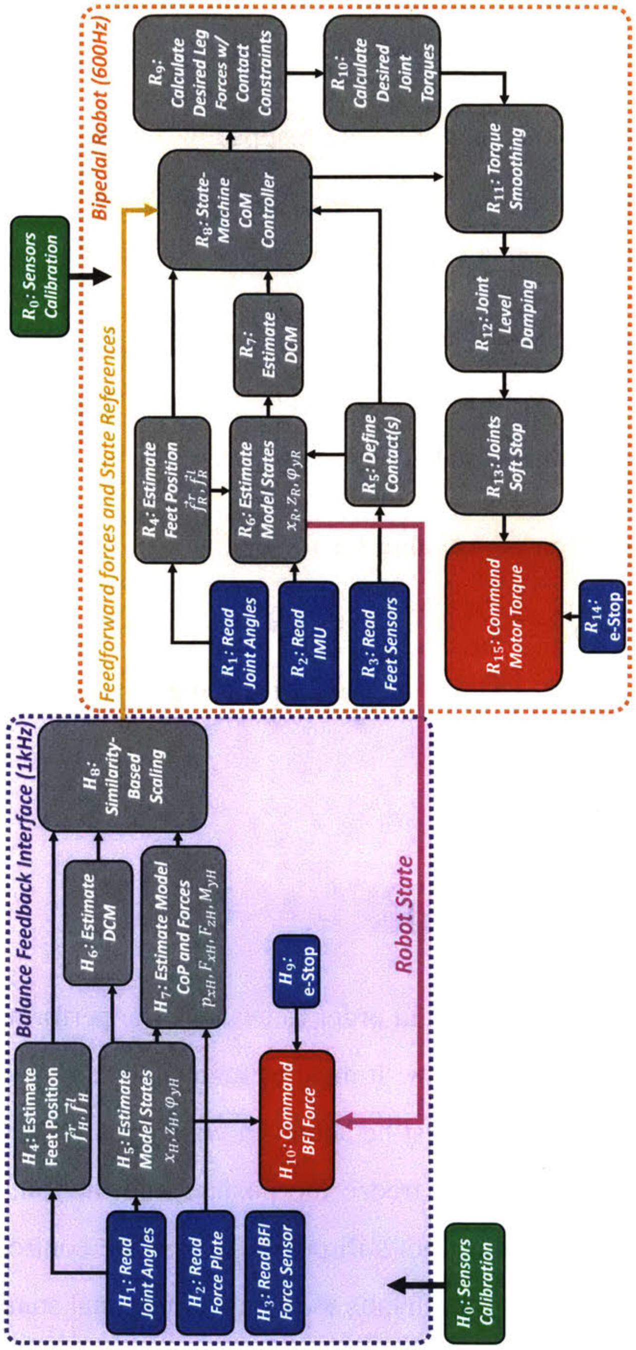

Figure 7-5: Overall control sequence for the teleoperation experiments. This block diagram includes initialization procedures (green), system inputs from sensors (dark blue), commands to actuators (red) and communication between BFI and robot (yellow and magenta arrows).

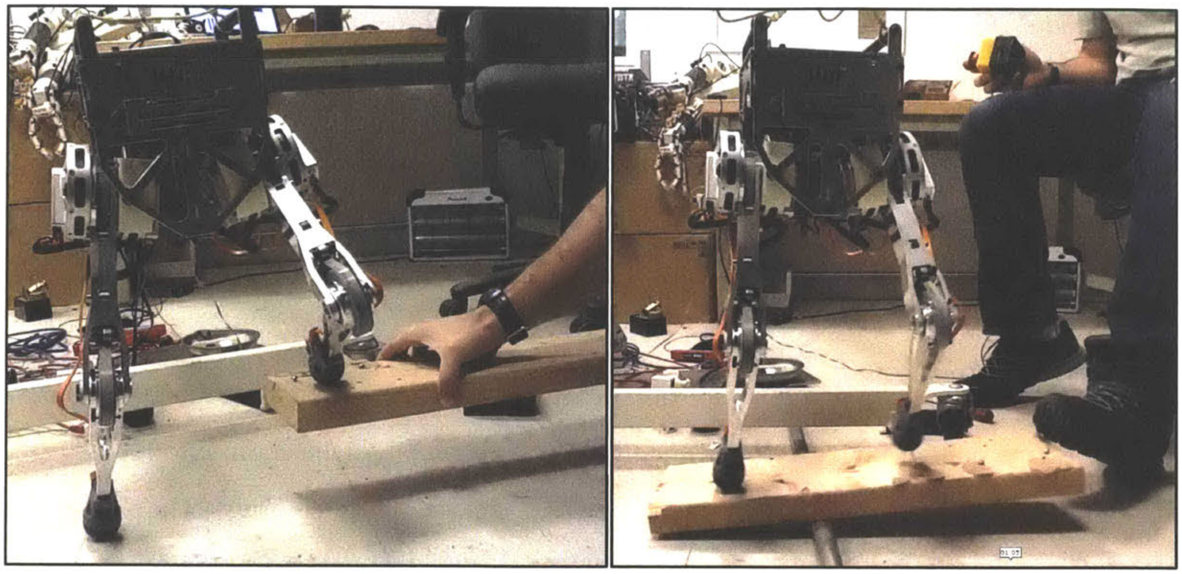

Figure 7-6: Example behaviors of the robot autonomous controller, when all references are set to zero. Left: given the contact position, the robot calculates the necessary forces to maintain its posture in space. Right: when in single support, the swing leg attempts to readjust the stance to nominal distance d_{0R}.

The term *Robot Stance* in the third plot is defined by the relative position of the CoP in respect to each foot. Thus,

$$Robot \quad Stance = \frac{p_{xR} - f^l_{xR}}{f^r_{xR} - f^l_{xR}},$$

which equals 1 when the CoP is under the right foot and 0 when the CoP is under the left foot.

Two factors can be noticed here. The first is that for small amplitudes, when the CoP does not reach any of the feet, the tracking performance of the robot's DCM ξ_{xR} is very accurate, it closely follows the human scaled DCM. We assume the high frequency oscillation originates from the compliance of the foot sensor, given that the CoM state is estimated using leg kinematics. Additionally, as expected, the robot relative CoP position is geometrically similar to humans'.

The second noticeable detail occurs when the CoP reaches one of the feet (single support), and the tracking performance of the DCM slightly deteriorates. This occurs because, during single support, the robot loses control authority over two of the four possible force components. Given that the system attempts to control three states (x_R, z_R and φ_{yR}) and only has two control inputs, the performance is compromised (see figure 7-8). Regardless, the force produced by the BFI slightly slows down the human motion such that the tracking is preserved.

7.4.2 Stepping in Place

Taking steps in place is a natural extension of the side-to-side motion described previously. The difference is that now the robot must briefly dynamically balance on one foot during leg swing, thus this motion cannot be achieve by semi-static trajectories. The swing leg also follows the human foot trajectory in order to control the step placement. Figure 7-9 shows the behavior of the robot when following the human as represented by the snapshots in Figure 7-11. Figures 7-10 shows vertical and horizontal components of the same planar trajectory across time, notice the visualization of the LIP for selected instants.

7.4.3 Effects of Feedback Force

Its important to point out that the feedback forces are responsible for informing the operator about the instantaneous performance of the robot. If the slave system has been disturbed by and external force or if it looses synchronization, the feedback force F_{BFI} can provide this information to the operator. Figure 7-12 shows the behavior off the system when the robot attempts to follow human motion without feedback, which is just activated $\approx 3.5s$. The area in red represents $F_{BFI} = 0$, while the areas in green represents the utilization of the feedback force to the human. Under the effect of the BFI force, the reference provided to the robot from human motion data is now consistent with the model dynamics and both systems can synchronize.

7.4.4 Jumping

Dynamic jumping is a motion that can be trivially transmitted to the robot. During this action, the operator suddenly increases the vertical component of the ground reaction force. From equation (4.28), the robot generates a similar effort against the ground, allowing it to

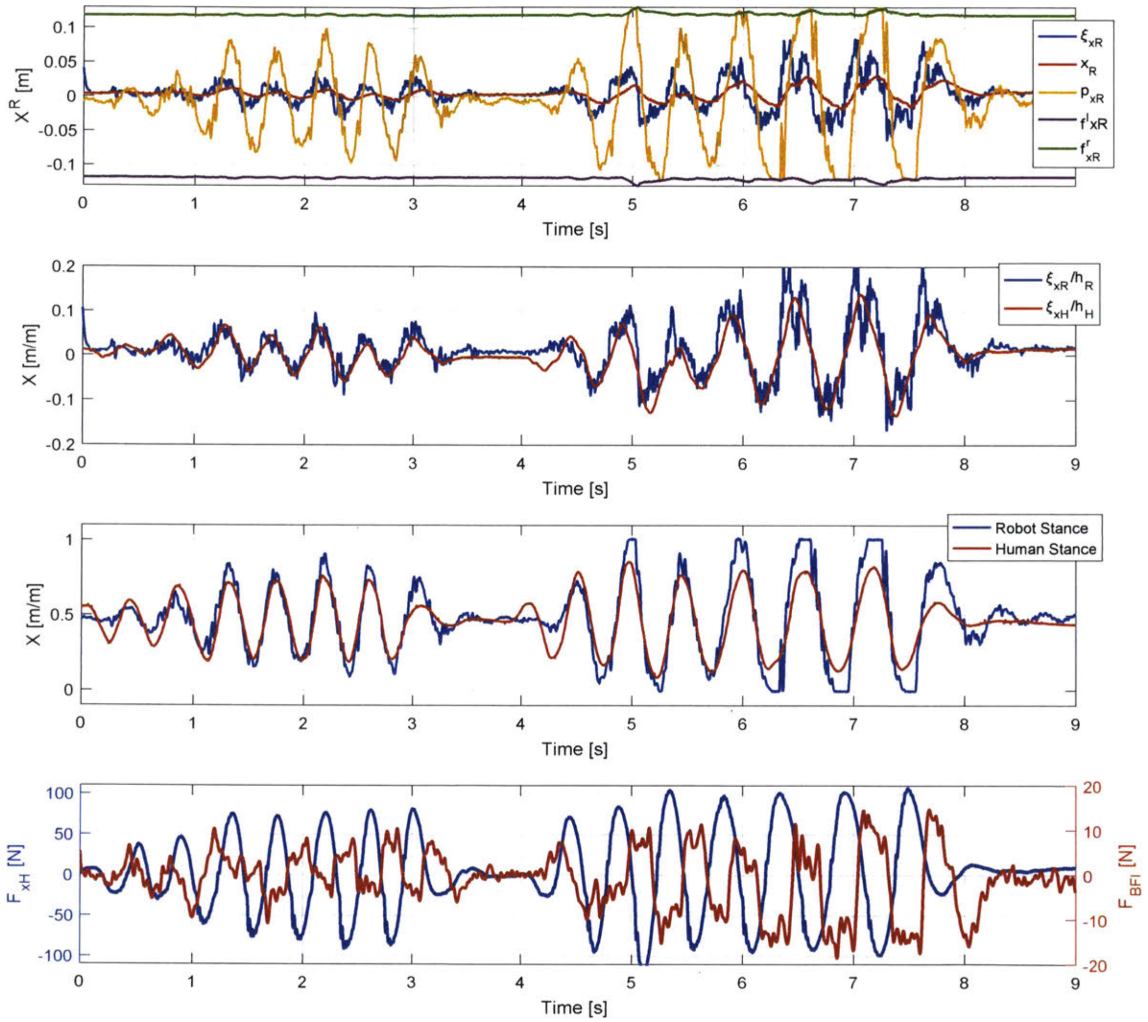

Figure 7-7: Tracking performance for simple side-to-side motion during normal stance. When the robot CoP lies between the feet, both systems DCM follow similar dynamics. The feedback force F_{BFI} makes sure that the human generate feasible references for the robot.

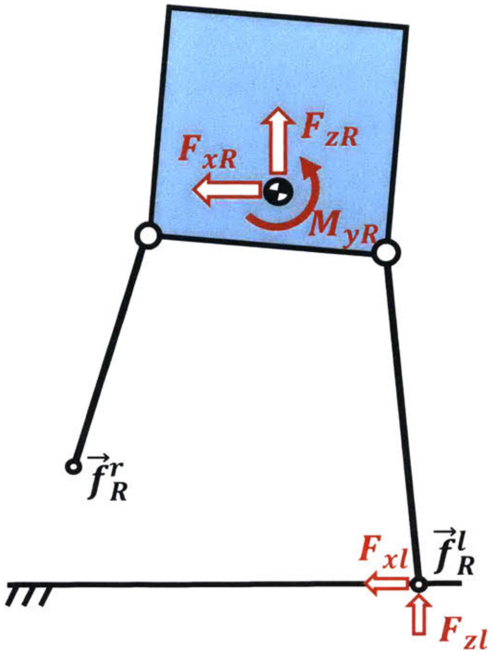

Figure 7-8: Single support condition. The robot only has two control inputs (F_{xl} and F_{zl}) available to control three desired efforts (F_{xR}, F_{zR} and M_{yR}).

jump. Figure 7-13 shows in blue the feedfoward component of the robot controller while in red we see the vertical force that both feed exert to the body together. The bottom plot depicts the vertical displacement of the CoM from leg kinematics and from the boom. Notice that when the robot is off the ground, the vertical CoM estimation from leg kinematics saturates at maximum leg extension. Figure 7-14 shows snapshots of selected instances during the jump motion.

7.4.5 Uneven Terrain

As shown for the simulated robot in figure 4-19, the force controller proposed here is robust to small variations in the terrain such as when the robot steps on an obstacle that is not present for the operator. Figure 7-15 depicts this situation. In figure 7-16 we see the stance dynamics of the robot when it steps on an obstacle. Notice that the world reference frame for the robot lies in the middle point between both feet, thus, the object height is given by the difference between feet height ($\approx 2.5cm$ here).

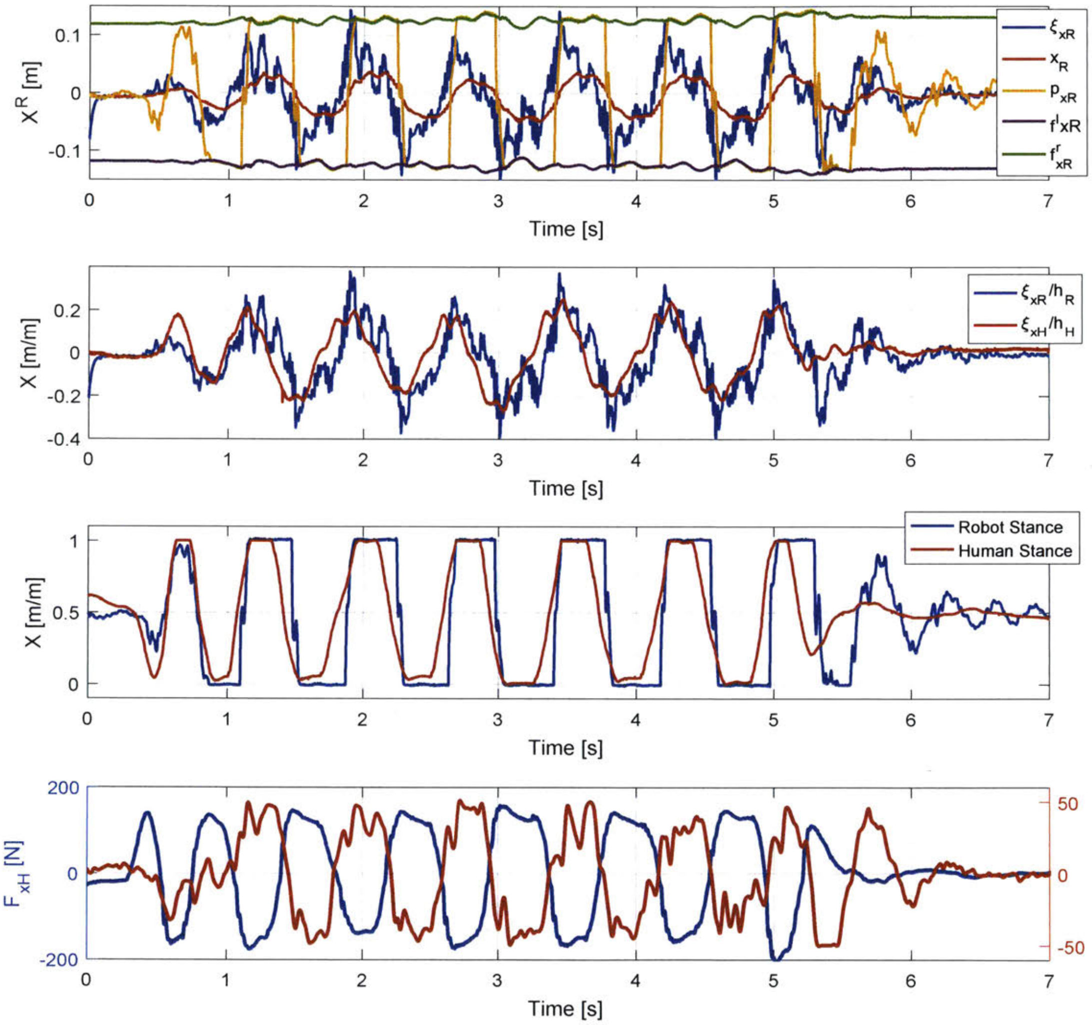

Figure 7-9: Tracking performance for stepping in place. We can evidence the synchronized change of support between left and right feet. The high frequency component of the robot DCM originates from the $\dot{x}_R$ estimation using a filtered derivative.

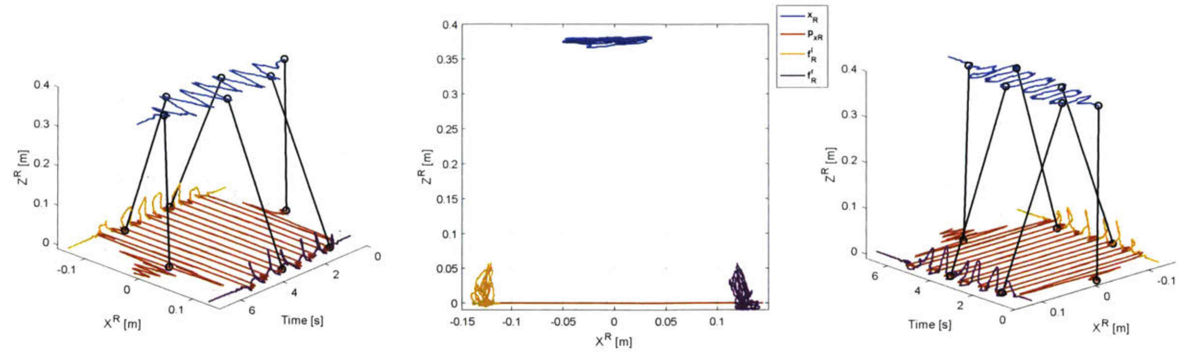

Figure 7-10: Spacial trajectory of the robot Center of Mass, Center or Pressure and feet when stepping in place. The LIP model, the line that connects the x_R and the p_{xR}, is superimpose for selected instants to represent the dynamic motion. Left and Right plots shows the same information from different angles. The middle plot is the projection in the X^R, Z^R plane.

7.5 Summary and Discussion

To the author's knowledge, the results presented in this Chapter are unprecedented. It is the first time that dynamically induced change of support and stepping is demonstrated via bilateral feedback teleoperation. Previous work in the literature already presented strategies to control a bipedal robot to take steps and walk via unilateral feedback [31]. However, the robot achieves this behavior by a pre-programmed routine that is controlled by the human on a higher level. In contrast, in our approach, the operator is directly coupled to the machine in a much lower level. Hence, in order to control the robot, the human must generate motions that affect both systems, the human body and the robot. The operator must learn how to accomplish the task while dealing with the robot's added dynamics. We assume that, if the operator is able to master this skill, s/he will be able to naturally control the robot, much like learning how to play a new sport.

The motions achieved here, however, are just a small fraction of what we assume can be done with this control strategy. For instance, a robot with ankle joints, and able to balance itself on the Sagittal Plane, can easily be controlled to walk and run. Alternatively, with the addition of upper limbs to the robot and roll moment feedback to the operator, momentum-based balancing strategies can now be explored. Furthermore, by mounting a stereo camera to the robot, the operator can now select precise foot stepping locations. The

Figure 7-11: Sequence of snapshots for teleoperated stepping in place. The robot cannot statically balance during single stance, it must continually move in order to be dynamically stable.

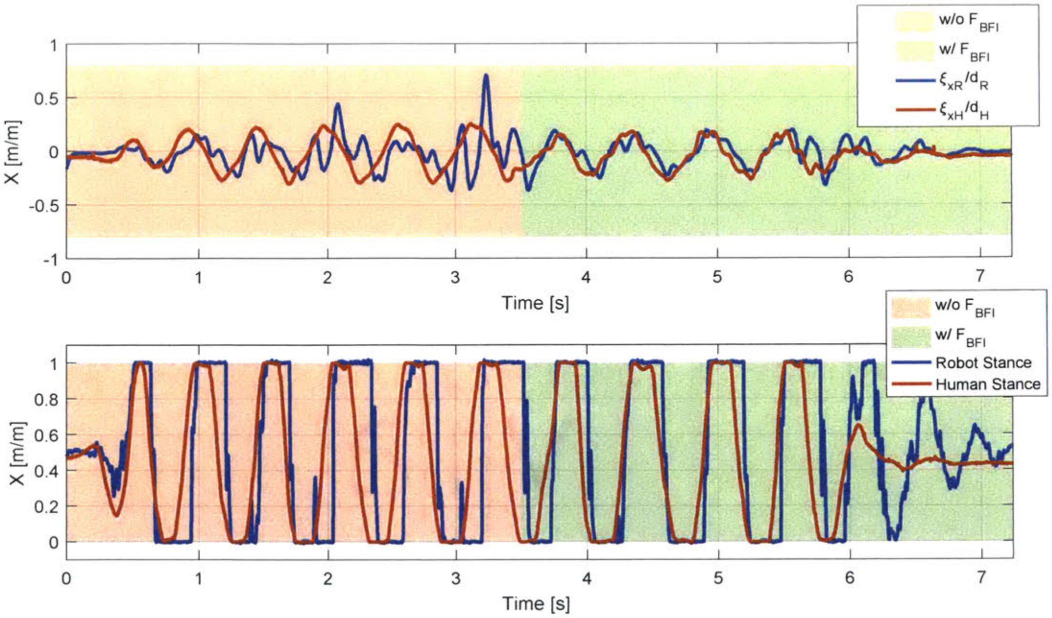

Figure 7-12: Stepping in place experiment when the BFI force is turned-off and suddenly activated during motion. Notice the stabilization of the robot DCM and the synchronization of the stance between right and left feet.

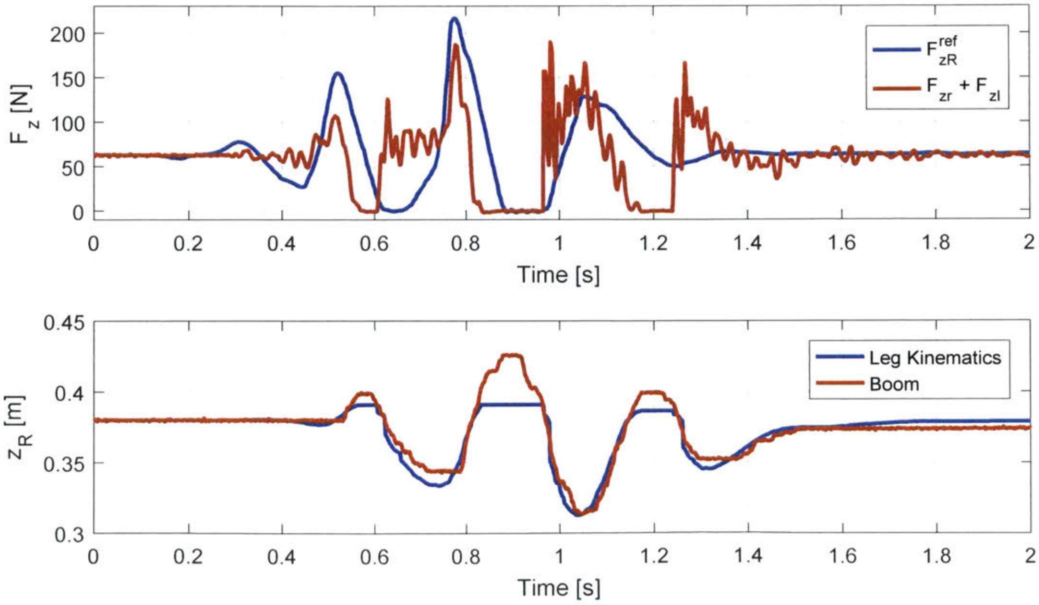

Figure 7-13: Top: Feedfoward force profile for jumping motion. The hight frequency component is likely originated from foot compliance. Bottom: CoM height estimation form leg dynamics and from the boom. When the robot is in flight the height estimation saturates because the legs reach full extension.

Figure 7-14: Sequence of snapshots for teleoperated dynamic jump. Notice on the top right sub-figure when the operator and the robot are both in flight.

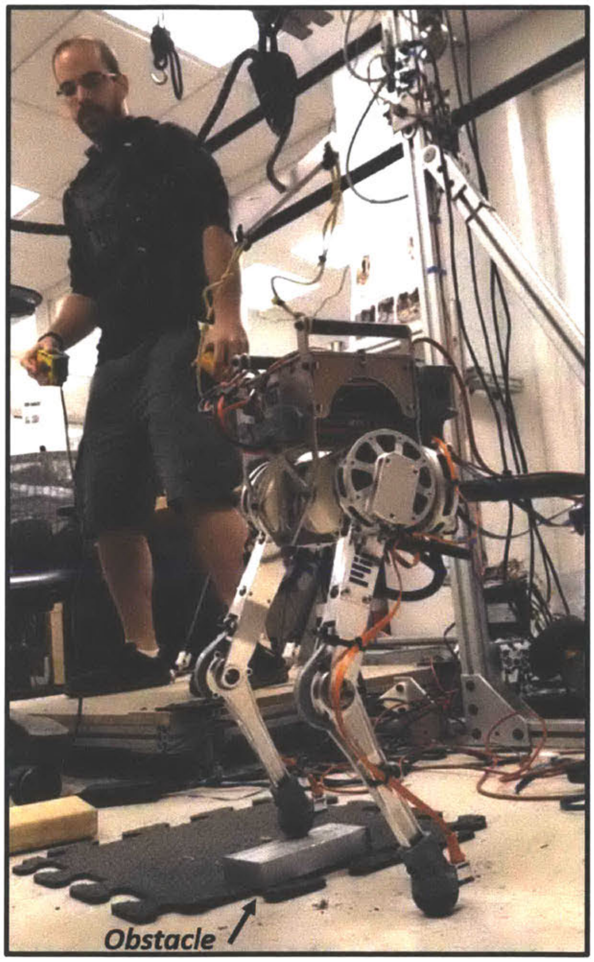

Figure 7-15: The robot steps on an 2.5*cm* obstacle that is not present for the human operator. The force controller is capable of dealing with such disparity.

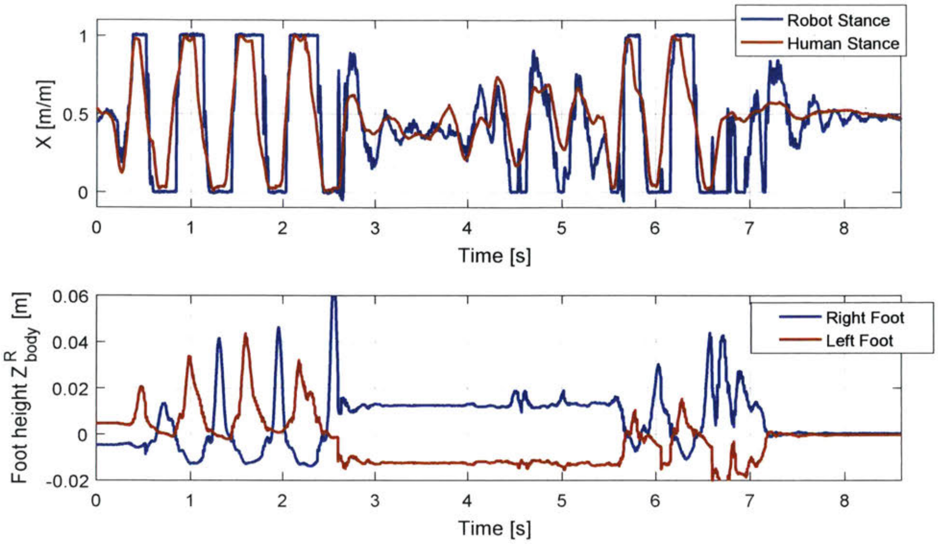

Figure 7-16: Robot stance dynamics when stepping on obstacle. The upper plot shows the change of stance compared to human input. The bottom plot shows the foot height in respect to the body including when the robot steps on the $2.5cm$ high object between $\approx 2.8s$ to $\approx 5.6s$. Notice that zero corresponds to the average height between both feet.

strategy presented here can be extended to a completely immersive experience.

Chapter 8

Discussion and Conclusions

8.1 Discussion

The interfacing between a human operator and a legged machine is a very complex task, specially if it requires bilateral information flow during highly dynamic tasks. However, if successful, it brings some evident advantages. Imagine for a second that a human operator can control a humanoid machine with the same capability s/he moves one's own body. The applications for such capable robot for field operations are endless. In contrast, most of the approaches for the control of autonomous robots, such as in [15], must use simple and intuitive heuristics to generate the motion references that allow autonomous robots to walk and interact with the world. Alternatively, motion planning algorithms based on optimization can be utilized to control the robot, but this calculation must be done off-line and requires accurate knowledge about the environment. On the other hand, the key idea behind our methodology is that the motion strategy and intention utilized by the human can be summarized by the interaction between the Center of Mass and the net ground contact forces. Hence, the human automatically provides near-optimal (and, more importantly, feasible) kinematic and dynamic references for the slave machine in real-time without the need for complex perception and/or motion planning algorithm. During extreme situations, the operator can even prototype new motions on the fly, as humans often do. Moreover, this action can be as simple or convoluted as needed, depending of the degree of authority the operator has over the robot. The challenge that needs to be solved here is to define the best way to bilaterally transfer dynamic information between both systems such that the human can experience the robot as a extension of his/her body.

To bridge the gap between human and robot, a novel device, the Balance Feedback Interface, that captures motion data and applies large feedback forces to the operator is presented in Chapter 2. This HMI is utilized in the experiments throughout this Thesis. In Chapter 3 we present a high-level description of the HERMES Project, our first approach to teleoperate a humanoid robot using human whole-body input. A simple model-free control strategy allowed the humanoid robot to perform a variety of unprecedented dynamic tasks with extreme interactions with the environment, such as breaking through a dry wall and using an ax to strike a wooden door. Despite the limited capabilities of the robot, this approach illustrates the advantages and the potential of direct teleoperation over classic autonomous controllers based on perception and motion planning algorithms. Motivated by the results from HERMES, Chapter 4 introduces the core contribution of this Thesis, a model-based mapping strategy that imposes dynamic similarity between human and robot motion. In that Chapter, the operator controls simulated robots with natural frequencies that are substantially different than humans'. The following Chapter, Chapter 5, describes the experimental evaluation of the proposed control law on a simple physical system, the Cart-Pole, that illustrates the model commonly utilized for human walking: the Linear Inverted Pendulum. Finally, Chapters 6 and 7 together present the procedure to apply the bilateral feedback teleoperation to a small-scale bipedal robot, Little HERMES. Chapter 6 presents a collection of design principles that are required for achieving high bandwidth force control and impact mitigation, capabilities required for dynamic legged robots. Moreover, Chapter 7 utilizes the theory developed in Chapter 4 to control Little HERMES' stance and stepping actions. To the authors knowledge, this is the first time that such dynamic and non-trivial motions are achieved using whole-body teleoperation with force feedback.

It is important to notice that the relevance of the force feedback F_{BFI} is not evident solely in the DCM tracking performance, if that was the case, simply optimizing the robot autonomous controller would likely suffice. Instead, the force feedback provides the human with valuable information about the robot motion in real-time. For instance, the direction and magnitude of the feedback force provides the information about the robot scale and dynamic capabilities, allowing the operator to adapt his/her own motion accordingly. Notice in Figure 4-13 how the stepping frequency varies according to robot scale. In fact, larger robots lead to negative feedback to the human, rendering the impression of added drag. Smaller scale robots, on the other hand, causes forces that accelerate the operator's natural motion, increasing stepping frequency. Additionally, this force feedback also allows the human to experience unexpected perturbations to the robot during motion. If the robot controller is not able to cope with such disturbances, the human operator can readjust his/her motion online. Finally, although not the scope of this thesis, it is very likely that human motor learning plays a significant role on the success of the bilateral teleoperation. We anticipate that seamless teleoperation can be achieved if the human is able to sufficiently practice with the coupled human-robot dynamics via appropriate physical feedback. This idea is very similar to practicing and learning a new sport.

An evident drawback of this method is related to an old issue for telerobotics: communication delay. It is still unclear how much delay the strategy proposed in this thesis can tolerate. Given the slow natural frequency of the dynamic systems in this work, we expect that, for moderate amounts of lag, the bilateral teleoperation can still be successful. However, we argue that the challenge of achieving high-speed communication is still considerably simpler than the challenges of achieving human-level perception, motion planning and adaptability. Thus, despite the fact that this is one of the very first studies in the field, we believe that bilateral teleoperation is still a more promising short-term solution for deploying robots to unstructured scenarios.

We speculate that the reason why there are very few examples of humanoid whole-body teleoperation with bilateral feedback in the literature is because it requires a very complex experimental setup and a deep understating about robotics and biomechanics. Hence, it requires the involvement of many disparate areas of research such as control theory, biomechanics, mechatronic design, communication theory, motor learning, among other. These are, by themselves, very extensive and complex fields, and some of them are not even mature yet.

8.2 Future Work

Because the work done in this Thesis involves so many different areas of research, there are a multitude of directions that can be explored for future work. Some of these directions are natural extensions of the theory developed here. For instance, we envision the relaxation of the adopted model, allowing variable natural frequencies by modifying equation (4.13) (to allow $\dot{\omega}_R \neq 0$). This leads to a nonlinear system that couples horizontal and vertical dynamics, producing a slightly modified force feedback law F_{BFI} than (4.26). Although it is unclear how extreme are the behaviors our method can produce, by including a variable ω_i we expect to achieve more complex actions that include significant variations in stance height. Another possible natural development of the current approach is to extend the feedback to the other axis. For example, we believe that including feedback for the roll torque (Y^H direction) could greatly improve the usefulness of momentum strategies for balancing, as described in [1]. Additionally, in this Thesis, we study the Frontal Plane dynamics with the intention to expand the current work to walking motions. We envision that the operator will perform a walking-in-place motion while the robots follows a moving reference. The strategy developed here can be utilized so the operator can control the robot around this moving reference. Hence, for this scenario, controlling the frontal plane dynamics is a fundamental ability.

Other pertinent questions that originate from this work are:

1. Optimization of the robot autonomous controller. More specifically, how does the feedback gain K_x from (4.25) affect the teleoperation performance? We interpret this gain as a level of "autonomy" of the robot. It roughly regulates how much control authority is given to the robot itself or to the operator over the robot balancing.

2. Here we avoided the addition of conservative constraints in order to explore the motion possibilities that could be achieved. For a robot that will be deployed in a real world scenario, what safety metrics should be included? Such as boundaries on the CoP or DCM travel?

3. Similar to other Human-Robot Interaction (HRI) studies, we assume learning is a

significant factor for the task success, as clearly presented in [8]. Thus, a statistical analysis of many experiments with different subjects is required to allow definitive interpretation of the results.

4. A basic but pertinent question relates to the mechanical design of the Human-Machine Interface and how to reliably apply forces to the operator. Ideally we would like to apply forces directly to the CoM, but how can we achieve this goal given skin compliance, discomfort and etc?

5. Here we study superficially the effects of scale on the teleoperation strategy. However, it is not yet clear what are the boundaries of how small or big the robot can be relatively to the human such that the dynamic similarity teleoperation still makes sense. There are likely a minimum and maximum robot sizes that the human is physically able to synchronize with.

6. Robotics research have considerably advanced the control of autonomous robots with more sophisticated algorithms. The combination of bilateral feedback with such controllers could offers promising solutions. For instance, for more complex contact conditions, the force distribution solution from equations (4.54) to (4.57) can be replaced by an Optimization-Based controller. The challenge being the definition of the control authority that is given to the human and to the robot.

7. As shown on equation (4.45), the external forces applied to the robot could be estimated by the machine and transmitted back to the operator. This information can be included in the feedback law, allowing the operator to perform more appropriate corrections including during static conditions.

8.3 Conclusions

This Thesis introduces our approach to achieve dynamic bilateral feedback teleoperation of a bipedal robot using human whole-body motion. The novel teleoperation strategy developed here addresses the issue of self-balancing while performing dynamic tasks that involve whole-body coordination. This approach is fundamentally different from the solution to the classic bilateral telerobotics of robotic manipulators with fixed base. To the author's knowledge, this strategy is still effectively unexplored in the literature, specially for highly dynamic actions. In this Thesis, we take advantage of human innate motion skills and map human kinematic and force information such that the motion of the robot is dynamically similar to the model for the operator. To achieve this, the Balance Feedback Interface provides force feedback to the human which incorporates the information about the robot's physical scale, as well as the instantaneous motion tracking performance. We utilize a reduced order model as the communication channel between the operator and robot, and pay special attention to how the natural frequency of each system affects the teleoperation result. The simplicity of the template utilized provides valuable insights about the fundamental behavior of the complex coupled system, with this gained awareness, we attempt to provide a framework for the whole-body teleoperation of legged machines.

Eventually, given sufficient training, we assume the bilateral teleoperation will feel to the operator as an extension of his/her own body, allowing the robot to harness human innate motor control capabilities. We envision this acquired skill as a fundamental stepping stone to allow robots to achieve extreme motor behaviors and eventually be reliably deployed to highly unstructured scenarios. We deeply hope that the work conducted in this Thesis can aid the development of robots that will, one day, be the first responders in real disasters and, possibly, save peoples lives.

Bibliography

[1] M. Abdallah and A. Goswami. A Biomechanically Motivated Two-Phase Strategy for Biped Upright Balance Control. In *Robotics and Automation (ICRA), 2005 IEEE International Conference on*. IEEE, 2005.

[2] R. McNeil Alexander. *Principles of Animal Locomotion*. Princeton University Press, 2003.

[3] Y. Asano, T. Shirai, T. Kozuki, Y. Motegi, Y. Nakanishi, K. Okada, and M. Inaba. Motion generation of redundant musculoskeletal humanoid based on robot-model error compensation by muscle load sharing and interactive control device. In *2013 13th IEEE-RAS International Conference on Humanoid Robots (Humanoids)*, 2013.

[4] World Nuclear Association, 2017. Available at: http://www.world-nuclear.org/.

[5] AxonVR. Available at: http://axonvr.com/.

[6] A. Brygo, I. Sarakoglou, N. Garcia-Hernandez, and N. Tsagarakis. Humanoid Robot Teleoperation with Vibrotactile Based Balancing Feedback. In *Haptics: Neuroscience, Devices, Modeling, and Applications. EuroHaptics 2014. Lecture Notes in Computer Science, vol 8619*. Springer, 2014.

[7] A. Brygo, I. Sarakoglou, N. Tsagarakis, and D. G. Caldwell. Tele-manipulation with a humanoid robot under autonomous joint impedance regulation and vibrotactile balancing feedback. In *Humanoid Robots, 2014 14th IEEE-RAS International Conference on*. IEEE, 2014.

[8] E. Burdet, R. Osu, D. Franklin, T. Milner, and M. Kawato. The central nervous system stabilizes unstable dynamics by learning optimal impedance. *Nature*, 414:446–449, 2001.

[9] A. Cela, J. J. Yebes, R. Arroyo, L. Bergasa, R. Barea, and E. LÃşpez. Complete low-cost implementation of a teleoperated control system for a humanoid robot. *Sensors*, 13(2):1385–1401, 2013.

[10] X. Chen, S. Nishikawa, K. Tanaka, R. Niiyama, and Y. Kuniyoshi. Bilateral teleoperation system for a musculoskeletal robot arm using a musculoskeletal exoskeleton. In *2017 IEEE International Conference on Robotics and Biomimetics (ROBIO)*, 2017.

[11] Meng Yee (Michael) Chuah and Sangbae Kim. Enabling force sensing during ground locomotion: A bio-inspired, multi-axis, composite force sensor using discrete pressure mapping. *IEEE Sensors Journal*, 14(5):1693–1703, 2014.

[12] B. Dariush, M. Gienger, A. Arumbakkan, Y. Zhu, B. Jian, K. Fujimura, and C. Goerick. Online transfer of human motion to humanoids. *International Journal of Humanoid Robotics*, 6(2):265–289, 2009.

[13] Reda Elbasiony and Walid Gomaa. Humanoids skill learning based on real-time human motion imitation using kinect. *Intelligent Service Robotics*, 11(2):149–169, Apr 2018.

[14] Englsberger, Ott, and Albu-Schaffer. Three-dimensional bipedal walking control using divergent component of motion. In *Intelligent Robots and Systems (IROS), 2013 IEEE/RSJ International Conference on*. IEEE, 2013.

[15] J. Englsberger, C. Ott, and A. Albu-Schaffer. Three-dimensional bipedal waling control based on divergent component of motion. *IEEE Transactions on Robotics*, 31(2), 2015.

[16] A. Di Fava, K. Bouyarmane, K. Chappellet, E. Ruffaldi, and A. Kheddar. Multi-contact motion retargeting from human to humanoid robot. In *2016 IEEE-RAS 16th International Conference on Humanoid Robots (Humanoids)*, 2016.

[17] M. Goldfarb. Similarity and invariance in scaled bilateral telemanipulation. *Journal of Dynamic Systems, Measurement, and Control*, 121:79–87, 1999.

[18] S. Guo, R. Southern, J. Chang, D. Greer, and J. Jun Zhang. Adaptive motion synthesis for virtual characters: a survey. *The Visual Computer: International Journal of Computer Graphics*, 31(5):497–512, 2014.

[19] D. Haldane, M. Plecnik, and R. Fearing. Robotic vertical jumping agility via series-elastic power modulation. *Science Robotics*, 1(1), 2016.

[20] Z. Hasan. The human motor control system's response to mechanical perturbation: should it, can it, and does it ensure stability? *Journal of Motor Control*, 37(6):484–493, 2005.

[21] L. Hof. The equations of motion for a standing human reveal three mechanisms for balance. *Journal of Biomechanics*, 40:451–457, 2007.

[22] L. Hof. The 'extrapolated center of mass' concept suggests a simple control of balancing in walking. *Human Motion Science*, 27(1):112–125, 2008.

[23] L. Hof, M. Gazendam, and W. Sinke. The condition for dynamic stability. *Journal of Biomechanics*, 38:1–8, 2005.

[24] Neville Hogan. CMU RI Seminar: The paradox of human performance. Available at: https://www.youtube.com/channel/UCW2eNKQeNIvl6MgFNKwLgBQ.

[25] K. Hongo, M. Yoshida, Y. Nakanishi, I. Mizuuchi, and M. Inaba. Development of bilateral wearable device kento for control robots using muscle actuator modules. In *RO-MAN 2009, The 18th IEEE International Symposium on Robot and Human Interactive Communication*. IEEE, 2009.

[26] Hopkins, Hong, and Leonessa. Compliant Locomotion Using Whole-Body Control and Divergent Component of Motion Tracking. In *Robotics and Automation (ICRA), 2015 IEEE International Conference on*. IEEE, 2015.

[27] Christian Hubicki, Jesse Grimes, Mikhail Jones, Daniel Renjewski, Alexander Sprowitz, Andy Abate, and Jonathan Hurst. Atrias: Design and validation of a tether-free 3d-capable spring-mass bipedal robot. *International Journal of Robotics Research*, 35(12):1497–1521, 2016.

[28] Vicon Intelligence in Motion. Available at: http://vicon.com/.

[29] Y. Ishiguro, T. Ishikawa, K. Kojima, F. Sugai, S. Nozawa, Y. Kakiuchi, K. Okada, and M. Inaba. Online master-slave footstep control for dynamical human-robot synchronization with wearable sole sensor. In *Humanoid Robots, 2017 17th IEEE-RAS International Conference on*. IEEE, 2017.

[30] Y. Ishiguro, K. Kojima, F. Sugai, S. Nozawa, Y. Kakiuchi, K. Okada, and M. Inaba. Bipedal oriented whole body master-slave system for dynamic secured locomotion with lip safety constraintsr. In *Intelligent Robots and Systems (IROS), 2017 IEEE/RSJ International Conference on*. IEEE, 2017.

[31] Y. Ishiguro, K. Kojima, F. Sugai, S. Nozawa, Y. Kakiuchi, K. Okada, and M. Inaba. High speed whole body dynamic motion experiment with real time master-slave humanoid robot system. In *Robotics and Automation (ICRA), 2018 IEEE International Conference on*. IEEE, 2018.

[32] S. Kajita, F. Kanehiro, K. Kaneko, K. Yokoi, and H. Hirukawa. The 3d linear inverted pendulum mode: a simple modeling for a biped walking pattern generation. In *Proceedings 2001 IEEE/RSJ International Conference on Intelligent Robots and Systems (IROS)*, 2001.

[33] E. Kandel, J. Schwartz, T. Jessell, S. Siegelbaum, and A. Hudspeth. *Principles of Neural Science*. McGraw-Hill, 2013.

[34] G. Kenneally, A. De, and D. E. Koditschek. Design principles for a family of direct-drive legged robots. *IEEE Robotics and Automation Letters*, 1(2):900–907, 2016.

[35] S. Kim, C. Kim, B. You, and S. Oh. Stable whole-body motion generation for humanoid robots to imitate human motions. In *Intelligent Robots and Systems (IROS), 2009 IEEE/RSJ International Conference on*. IEEE, 2009.

[36] J. Koenemann. Real-time Imitation of Human Whole-Body Motions by Humanoids. In *Robotics and Automation (ICRA), 2014 IEEE International Conference on*. IEEE, 2014.

[37] Koolen, Boer, Rebula, and Goswami. Capturability-based analysis and control of legged locomotion, part 1: Theory and application to three simple gait models. *Robotics Research, International Journal on*, 2012.

[38] T. Koolen, M. Posa, and R. Tedrake. Balance control using center of mass height variation: Limitations imposed by unilateral contact. In *2016 IEEE-RAS 16th International Conference on Humanoid Robots (Humanoids)*, 2016.

[39] S. Kuindersma, R. Deits, Maurice Fallon, A. Valenzuela, H. Dai, F. Permenter, T. Koolen, P. Marion, and R. Tedrake. Optimization-based locomotion planning, estimation, and control design for the atlas humanoid robot. *Autonomous Robots*, 40:429–455, 2016.

[40] T. Kurotobi, T. Shirai, Y. Motegi, Y. Nakanishi, K. Okada, and M. Inaba. Controlling tendon driven humanoids with a wearable device with direct-mapping method. In *2012 IEEE RO-MAN: The 21st IEEE International Symposium on Robot and Human Interactive Communication*, 2012.

[41] S. Lee and A. Goswami. Reaction Mass Pendulum (RMP): An explicit model for centroidal angular momentum of humanoid robots. In *Robotics and Automation (ICRA), 2007 IEEE International Conference on*. IEEE, 2007.

[42] J. Lei, M. Song, Z. Li, and C. Chen. Whole-body humanoid robot imitation with pose similarity evaluation. *Signal Processing*, 108:136 – 146, 2015.

[43] T. McMahon and J. Bonner. *On Size and Life*. Scientific American Library, 1983.

[44] B. Na, H. Choi, and K. Kong. Design of a direct-driven linear actuator for a high-speed quadruped robot, cheetaroid-i. *IEEE/ASME Transactions on Mechatronics*, 20(2):924–933, 2015.

[45] S. Wang nad X. Zuo, R. Wang, F. Cheng, and R. Yang. A generative human-robot motion retargeting approach using a single depth sensor. In *Robotics and Automation (ICRA), 2017 IEEE International Conference on*. IEEE, 2017.

[46] S. Nakaoka, A. Nakazawa, F. Kanehiro, K. Kaneko, M. Morisawa, and K. Ikeuchi. Task model of lower body motion for a biped humanoid robot to imitate human dances. In *2005 IEEE/RSJ International Conference on Intelligent Robots and Systems*, 2005.

[47] N. Naksuk, C. S. G. Lee, and S. Rietdyk. Whole-body human-to-humanoid motion transfer. In *5th IEEE-RAS International Conference on Humanoid Robots, 2005.*, 2005.

[48] K. Otani and K. Bouyarmane. Adaptive whole-body manipulation in human-to-humanoid multi-contact motion retargeting. In *2017 IEEE-RAS 17th International Conference on Humanoid Robotics (Humanoids)*, 2017.

[49] A. Ott, A. Roa, and G. Hirzinger. Posture and balance control for biped robots based on contact force optimization. In *Humanoid Robots, 2012 11th IEEE-RAS International Conference on*. IEEE, 2012.

[50] C. Pacchierotti, L. Meli, F. Chinello, M. Malvezzi, and D. Prattichizzo. Cutaneous haptic feedback to ensure the stability of robotic teleoperation systems. *International Journal of Robotics Research*, 34(14):1773–1787, 2015.

[51] H. Park, S. Park, and S. Kim. Variable-speed Quadrupedal Bounding Using Impulse Planning: Untethered High-speed 3D Running of MIT Cheetah 2. In *Robotics and Automation (ICRA), 2015 IEEE International Conference on*. IEEE, 2015.

[52] J. Park, J. Haan, and F. C. Park. Convex optimization algorithms for active balancing of humanoid robots. *IEEE Transactions on Robotics*, 23(4):817–822, 2007.

[53] Peternel and Babic. Learning of compliant human-robot interaction using full-body haptic interface. *Advanced Robotics*, 27, 2013.

[54] L. Peternel and J. Babic. Humanoid robot posture-control learning in real-time based on human sensorimotor learning ability. In *Robotics and Automation (ICRA), 2013 IEEE International Conference on*. IEEE, 2013.

[55] M. Popovic, A. Goswami, and H. Herr. Ground reference points in legged locomotion: Definitions, biological trajectories and control implications. *The International Journal of Robotics Research*, 24(12):1013–1032, 2005.

[56] Michael Posa. *Optimization for Control and Planning of Multi-contact Dynamic Motion*. PhD thesis, Massachusetts Institute of Technology, 6 2017.

[57] L. P. Poubel, S. Sakka, D. ÄĘehajiÄĞ, and D. Creusot. Support changes during online human motion imitation by a humanoid robot using task specification. In *Robotics and Automation (ICRA), 2014 IEEE International Conference on*. IEEE, 2014.

[58] Pratt, Carff, Drakunov, and Goswami. Capture point: A step toward humanoid push recovery. In *Humanoid Robots, 2006 6th IEEE-RAS International Conference on*. IEEE, 2006.

[59] G. A. Pratt and M. M. Williamson. Series elastic actuators. In *Proceedings 1995 IEEE/RSJ International Conference on Intelligent Robots and Systems. Human Robot Interaction and Cooperative Robots*, volume 1, pages 399–406 vol.1, 1995.

[60] J. Pratt, B. Krupp, and C. Morse. Series elastic actuators for high fidelity force control. *Industrial Robot: An International Journal*, 29:234–241, 2002.

[61] Joao Ramos, Benjamin Katz, Meng Yee Chuah, and Sangbae Kim. Facilitating model-based control through software-hardware co-design. In *Robotics and Automation (ICRA), 2018 IEEE International Conference on*. IEEE, 2018.

[62] Joao Ramos and Sangbae Kim. Humanoid dynamic synchronization through whole-body bilateral feedback teleoperation. *IEEE Transactions on Robotics, (to appear)*, 2018.

[63] S. Seok, A. Wang, D. Otten, and S. Kim. Actuator design for high force proprioceptive control in fast legged locomotion. In *Intelligent Robots and Systems (IROS), 2012 IEEE/RSJ International Conference on*. IEEE, 2012.

[64] B. Siciliano and O. Kathib. *Handbook of Robotics*. Springer, 2008.

[65] IEEE Spectrum. Humanoid robot Mahru mimics a person's movements in real time, 2010.

[66] IEEE Spectrum, 2011. Available at: https://spectrum.ieee.org/.

[67] M. Stilman, Koichi Nishiwaki, and Satoshi Kagami. Humanoid teleoperation for whole body manipulation. In *2008 IEEE International Conference on Robotics and Automation*, 2008.

[68] W. Suleiman, E. Yoshida, F. Kanehiro, J. P. Laumond, and A. Monin. On human motion imitation by humanoid robot. In *2008 IEEE International Conference on Robotics and Automation*, 2008.

[69] Gypsy 7 Motion Capture System. Available at: http://metamotion.com/.

[70] Takenaka, Matsumoto, and Yoshiike. Real time motion generation and control for biped robot -1st report: Walking gait pattern generation. In *Intelligent Robots and Systems (IROS), 2009 IEEE/RSJ International Conference on*. IEEE, 2009.

[71] Teslasuit. Available at: https://teslasuit.io/.

[72] OptiTrack Motion Tracking. Available at: http://optitrack.com/.

[73] Xsens 3D Motion Tracking. Available at: http://xsens.com/.

[74] uppercaseCSIC uppercaseUPC. Teleoperation of a robot arm through a haptic device. Available at: https://www.youtube.com/channel/UCW2eNKQeNIvl6MgFNKwLgBQ.

[75] M. Vukobratovic and B. Borovac. Zero-moment point âĂŞ thirty five years of life. *International Journal of Humanoid Robotics*, 01:157–173, 2004.

[76] X. Wang, Q. Chen, and W. Wang. 3d human motion editing and synthesis: A survey. *Computational and Mathematical Methods in Medicine*, 2014.

[77] Y. Wang and M. Srinivasan. Stepping in the direction of the fall: the next foot placement can be predicted from current upper body state in steady-state walking. *Biology Letters*, 2014.

[78] G. Welch and E. Foxlin. Motion tracking: no silver bullet, but a respectable arsenal. *IEEE Computer Graphics and Applications*, 22(6):24–38, 2002.

[79] P. Wensing and D. Orin. Generation of dynamic humanoid behaviors through task-space control with conic optimization. In *Robotics and Automation (ICRA), 2013 IEEE International Conference on*. IEEE, 2013.

[80] P. Wensing, A. Wang, S. Seok, D. Otten, J. Lang, and S. Kim. Proprioceptive actuator design in the mit cheetah: Impact mitigation and high-bandwidth physical interaction for dynamic legged robots. *IEEE Transactions on Robotics*, 33(3), 2017.

[81] P. M. Wensing, A. Wang, S. Seok, D. Otten, and S. Kim J. Lang. Proprioceptive actuator design in the mit cheetah: Impact mitigation and high-bandwidth physical interaction for dynamic legged robots. *IEEE Transactions on Robotics*, 33:509–522, 2017.

[82] K. Yamane, S. O. Anderson, and J. K. Hodgins. Controlling humanoid robots with human motion data: Experimental validation. In *Humanoid Robots, 2010 10th IEEE-RAS International Conference on*. IEEE, 2010.

[83] K. Yamane and J. Hodgins. Control-aware mapping of human motion data with stepping for humanoid robots. In *Intelligent Robots and Systems (IROS), 2010 IEEE/RSJ International Conference on*. IEEE, 2010.

[84] Y. Zheng and K. Yamane. Human Motion Tracking Control with Strict Contact Force Constraints for Floating-Base Humanoid Robots. In *Humanoid Robots, 2013 12th IEEE-RAS International Conference on*. IEEE, 2013.

[85] Y. Zheng and K. Yamane. Adapting Human Motions to Humanoid Robots Through Time Warping Based on a General Motion Feasibility Index. In *Robotics and Automation (ICRA), 2015 IEEE International Conference on*. IEEE, 2015.